Experimental Results on " $K^0_S - K^0_L$ " Asymmetry in D^0 Decays

Manmohan Dash

12th January 2009

Dissertation[a] Submitted to the Faculty of

VIRGINIA POLYTECHNIC INSTITUTE AND STATE UNIVERSITY

in partial fulfilment of the requirements of the degree of

"DOCTOR OF PHILOSOPHY IN PHYSICS"

Blacksburg, Virginia

[a]***key words:*** *Charm Physics, Cabibbo Favored and Doubly Cabibbo Suppressed Asymmetry in K^0 Meson, Charm Factory at Belle, e^+e^- Collider at KEK, Belle Collaboration, Spontaneous Symmetry Breaking*

Committee		Signature
Professor	Leo Piilonen, Chair	
Professor	Marvin Blecher	
Professor	Tetsuro Mizutani	
Professor	Mark Pitt	
Professor	John Simonetti	

$\{K_S^0 - K_L^0\}$ Asymmetry in $\{D^0\}$ Decays

Abstract

This analysis aims at carrying out measurements to determine an asymmetry that has been proposed to exist in the decay of D^0 meson into various CF and DCS modes.[a] A detailed measurement of the D^0 decay into $K_L^0\pi^0$ and $K_S^0\pi^0$ final states has been performed along with other necessary related decay modes. The result from this can be used to disentangle the CF $D^0 \to \overline{K}^0\pi^0$ and DCS $D^0 \to K^0\pi^0$ amplitudes, and contributes to the important goal of constraining the strong phase $\delta_{K\pi}$ between $D^0 \to K^-\pi^+$ and $D^0 \to K^+\pi^-$. This measurement is based on a small fraction of data set accumulated by the Belle detector at the KEKB e^+e^- collider, with K_L^0 candidates reconstructed using hadronic clusters in the KLM[b] together with a D^0 mass constraint and D^* tag. This asymmetry is akin to a generic process of symmetry breaking. While the main goal of the Belle asymmetric detector is to study the spontaneous symmetry breaking in the B-meson system[c], the colossal size of the data accumulated "off" the $\Upsilon(4S)$ resonance also provides a suitable machine for the study of the charm meson sector.

[a] CF and DCS stand for Cabibbo Fabored and Doubly Cabibbo Suppressed

[b] The K_L^0 and μ identification system at Belle is known as KLM

[c] CP or charge-parity violation

key words

Charm Physics

Cabibbo Favored and Doubly Cabibbo Suppressed Asymmetry in K^0 Meson

Charm Factory at Belle

e^+e^- Collider at KEK

Belle Collaboration

Spontaneous Symmetry Breaking

Acknowledgement

As the author of this thesis I have recieved help, support and friendship from a long list of people, usual in experimental high energy physics. I would like to acknowledge the support and friendship of the following people.

FIRST of all, I would like to express my deep sense of gratitude to my thesis adviser Professor Leo Piilonen. Leo gave a definite shape to my naive questioning attitude with his patient, critical and detailed guidance. It was an enriching experience to have worked with world's most talented experts in the field at Belle Experiment in Japan. I would like to mention expert input and keen interest of Dr Bostjan Golob of Slovenia, Professor Yoshihide Sakai of Japan and initial guidance of Bruce Yabsley of Australia. Bostjan gave a sofisticated shape to the analysis. I wish to express my deep and sincere gratitude towards Sakai san and Bostjan for their input for my analysis and for posing trust in me as an Invited Speaker in charm quark physics in the conferences of the Physical Societies of USA and Japan. I would also like to thank Jian Gui Wang, a native of China who later migrated to Australia, for his help and guidance in my initial days at the experiment. I am indebted towards Vladishiv Balagura from Russia for enlightening technical discussions and help, Professor Thomas Browder from Hawaii for discussions on the steps of the analysis. I am grateful to Gobinda Majumdar from Mumbai, India for extremely useful technical help and to Sunil Kumar of Panjab, India for initial technical guidance. Professor Kazuo Abe of Japan who recently retired from the collaboration made sure international researchers had a nice experience in Japan. He has a great sense of humor and invited us to many dinners and took

us to beautiful places around Tsukuba where the Belle Detector Experiment is situated. I appreciate his friendly, helpful and humorous ways.

I enjoyed my stay In Japan. I would like to mention the following people for their continued friendship. I shared an excellent friendship with Urban Bitenc from Slovenia and Karina Arinstein from Russia. Urban and her lady friend Doroteja who is also from Slovenia and visited Japan, got married later. Deb Mohapatra who is now at Cornell University gave me useful advise and helped me when I needed them the most. Tapas and I shared a fun filled friendship that helped us work during isolating and stressful situations of PhD researchers. Seema, expecting to graduate soon with a PhD from Cincinnati University is also an excellent friend. Himansu from Hawaii University helped me to deal with the instabilities in my stay at Japan and USA resulting from my frequent travel schemes between the two countries. I would like to remember Karim Trabelsi of France, Nishida Shohei, husband and wife Ishino and Kibayashi, Sang Lee from Korea, Sachko Kataoka, Minori Watanabe, Morikun, Nakazawa-san and many other Japanese friends who made my stay in Japan enjoyable. Before I forget all the names which is quite likely given the huge size of high energy physics experiments, I would also like to mention Nitesh Sony, Sanjay Swain, Prafulla Behera, Ashis Satpathy and Professor Jasbir Singh for sharing fun time in Japan and for many discussions. I would like to thank young friendly secretaries Miyuki Hatogai and Imai Chihiro who were always enthusiastic and supportive of Belle Collaboration. I would like to thank Naka san who later joined the collaboration replacing Miyuki san, for her help during instability in my health. I had fallen ill towards the end of my stay in Japan and she went out of her way to help me for the hospital visits, where lack of Japanese skills could be fatal.

I was greatly inspired by the lectures and problem solving training of Professor Marvin Blecher, Professor Luke Mo, Professor Tetsuro Mizutani and Professor Beate Schmittman. All except Beate and Luke are in my graduate committee for thesis defense. On the personal side I would like to thank Christa Thomas for her continued support and friendship. I would also like to thank Kim Beisecker and Karen Wills of the Crewell International Center, the graduate ombudsperson Ennis McCrery and Professor Donald McKeon at Tech for their support in living an enjoyable and safe graduate students life. Suresh Lanka from the Maths Department and Bret Spencer from the Physics Department who I shared quite some time with helped me a great deal during my frequent travels to Japan. I would like to thank Professor Mamata Satapathy and Pro-

fessor Pushpa Khare of Utkal University, an erstwhile member institution of the Belle Experiment and my Alma mater, for offering me an opportunity to join the Belle Experiment, as a PhD student at Virginia Tech. I wouldn't have bagged the numerous opportunities that came after this without their offering me this opportunity. I am also delighted to mention Dr Karmadeva Maharani for his continued motivation and support during my masters program at Utkal. I was inspired by Professor Niranjan Barik for his eloquent lectures on Quantum Mechanics at Utkal University. His inspiration and support helped me succeed at the tough PhD program at Virginia Tech. I also want to express my deep gratitude towards Professor Lambodar Prasad Singh and Professor Shaktidhar Jena for writing letters for me to join Tech. I would like to mention Professor Laxmidhar Maharana for his inspiration, lectures and sense of humor that kept us motivated during his lectures at Utkal.

LAST but not the least I am deeply indebted to my parents and siblings for their continued support and motivation.

IT is not possible to mention everyone's name I would like to, for their support one way or the other. But I would like to drive home my point that a great number of people may enrichingly influence our lives personally and professionally in ways that may motivate us to learn finer aspects of our lives in pursuit of finer aspects of nature in the face of astounding adversities.

Manmohan Dash [*,†]
August 07, 2007

[*]Physics Department, Robeson Hall, Virginia Tech, Blacksburg, Virginia, USA, 24060-0435
[†]Belle Experiment, High Energy Accelerator Research Organisation (KEK), 1-1 Oho, Tsukuba, Ibaraki, Japan, 305-0801

Contents

List of Figures

List of Tables

Chapter 1

Experimental Situation and Motivation

"I was born not knowing, and I have only had a little time to change that here and there"

Richard Feynman

in this Chapter....The theoretical motivations and the experimental backgrounds of the measurement are described.

Literature in High Energy Physics and Phenomenology has a few papers that have touched the phenomena of $\{D \to (K_S, K_L)\pi\}$ asymmetry with a summary that directed for a grit rather than worked as a solid basis for carrying out this experiment.

AFTER this measurement was performed still more aspects have come up although they all lie in the precinct of experimental investigation. Nevertheless this measurement has given a semi-quantitative evidence of the proposed asymmetry in the process of neutral charmed meson's decay. An early phenomenological treatment that is available in the literature is one by Bigi and Yamamoto where they have summarized the situation before this measurement.[1] Extracting from their paper here is the summary of the physics of the situation.

"Both Cabibbo allowed and Doubly forbidden transitions contribute coherently to $D \to K_S, L + \pi$ decays. This leads to several intriguing and even quantitatively significant consequences, among them:

(i) A difference between $\Gamma(D^+ \to K_S\pi^+)$ and $\Gamma(D^+ \to K_L\pi^+)$ and between $\Gamma(D^0 \to K_S\pi^0)$ and $\Gamma(D^0 \to K_L\pi^0)$ of roughly 10 %; similarly $\Gamma(D^+ \to [K_S\pi^0]_{K^*}\pi^+) \neq 1/4\Gamma(D^+ \to [K^-\pi^+]_{K^*}\pi^+)$, and more generally $\Gamma(D \to K^0 + \pi's) \neq 2\Gamma(D \to K_S + \pi's)$.

(ii) A change in the relative phase between the isospin 3/2 and 1/2 amplitudes as extracted from the observed branching ratios for $D^+ \to K_S\pi^+, D^0 \to K_S\pi^0, K^-\pi^+$.

(iii) If new Physics intervenes to provide the required weak phase, then CP asymmetries of up to a few percent can arise in $D^+ \to K_S\pi^+$ vs $D^- \to K_S\pi^-$, $D^0 \to K_S\pi^0$ vs. $\overline{D}^0 \to K_S\pi^0$, $D^+ \to [K_S\pi^0]_{K^*}\pi^+$ vs. $D^- \to [K_S\pi^0]_{K^*}\pi^-$ etc.; an asymmetry of the same size, but opposite in sign occurs when the K_S is replaced by a K_L in the final state.

The weak decays of charm hadrons posses three layers, namely Cabibbo allowed, once and twice forbidden transitions. The first two layers have clearly been observed in D decays, while the third one is now emerging in the data. In this note we want to point out that the existence of doubly Cabibbo suppressed D(DCSD) channels has a subtle, yet significant impact on Cabibbo allowed D(CAD) decays producing neutral kaons. The main results are:

[1] Interference between Cabibbo allowed and doubly forbidden transitions in $D \to K_{S,L} + \pi's$ Decays, [7]

a) $\Gamma(D \to K_S + \pi's) \neq \Gamma(D \to K_L + \pi's)$ (irrespective of CP violation in $K \to \pi\pi$ decays) and thus $\Gamma(D \to \overline{K}^0 + \pi's) \neq 2\Gamma(D \to K_S + \pi's)$; the difference allows to extract the amplitude for the DCSD mode $D \to K^0 + \pi's$.
b) Ignoring DCSD leads to a systematic error of $\mathcal{O}(10\%)$ in the extraction of the final state phaseshifts in the $D \to K\pi$ etc. channels.
c) If New Physics intervenes in DCSD and provides a weak phase, then $D \to K_S + \pi's$ decays would exhibit a direct CP asymmetry that
(i) cancels against the corresponding asymmetry in $D \to K_L + \pi's$ vs. $\overline{D} \to K_L + \pi's$ modes,
(ii) establishes the existence of physics beyond the KM ansatz for CP violation and
(iii) can be interpreted in terms of the microscopic parameters of the New Physics.

The search for $D^0 - \overline{D}^0$ mixing has long been one of the most interesting projects in charm physics. Publications by the FOCUS [1] and CLEO [2] collaborations have stimulated a series of new measurements, including an updated y_{CP} measurement by the Belle collaboration [3], reported at the summer conferences.

An important quantity in the interpretation of $D^0 - \overline{D}^0$ mixing results is the phase difference $\delta_{K\pi}$ between the Cabibbo favored (CF) and doubly Cabibbo suppressed (DCS) neutral D meson decays. As has been shown in [4], new information on $\delta_{K\pi}$ may be obtained by measuring the asymmetry between the decay rates of D^0 into$K^0_L\ \pi^0$ and $K^0_S\ \pi^0$ where the effect may be as large as $\mathcal{O}(\tan^2\theta_c)$, i.e. at the 5% level.

In this thesis the author describes a detailed measurement of the $D^0 \to K^0_L\pi^0/D^0 \to K^0_S\pi^0$ decay rate asymmetry, using the Belle detector at the KEKB e^+e^- collider with a new approach compared to the first such measurement carried out at Belle before the author had joined the collaboration. In order to cancel out most of the systematic effects of the detector, we extract the K^0_L/K^0_S relative detection efficiency from the ratio of $K^0_L\pi^+\pi^-$ and $K^0_S\pi^+\pi^-$ modes via the decay $D^0 \to K^{*-}\pi^+$. The presence of $K^{*-} \to K^0\pi^-$ in the decay chain ensures equal rates of K^0_L and K^0_S in this case.

Throughout the thesis, the inclusion of CP-conjugate processes is implied. In particular, the $D^0 \to K^0_L\pi^0$ is combined with $\overline{D}^0 \to K^0_L\pi^0$, and so on. Thus the K_L and K_S are treated as CP-eigenstates[2] and it is assumed that direct CP violation in $D \to \overline{K}\pi$ and $K\pi$ decays, if present, may be ignored at our present sensitivity. At instances, however, study of only a particular decay mode or a set of modes without inclusion of their corresponding charge conjugate modes will suffice the purposes of such studies. The exclusion of charge conjugate modes will be mentioned. The final analysis includes all relevant modes in a consistent way. to be added more.....

[2] the error is negligible

Chapter 2

The Belle Detector and the Experiment

in this Chapter.....The Belle CP violation Experiment and the Belle Detector are described. The detector is located in the energy asymmetric e^-e^+ collider at Tsukuba, Japan where this measurement was performed.

2.1 THE GOAL OF THE BELLE EXPERIMENT

Introduction

The current theory of fundamental particles and their interactions is formally known as "Standard Model (SM)" of Particle Physics. These fundamental particles are categorized into three generations of spin -1/2 fermions, and the interactions between them are mediated by spin -1 bosons.

The SM has been successful in explaining physical phenomena "transmitted" by the fundamental forces viz. strong, electromagnetic and weak interactions, but not gravity.

ALMOST all experimental results to date are consistent with the SM. But, as we all have become aware, the SM is not the complete and final theory: it contains many ad hoc numbers (such as fermion masses) and puzzling phenomena (such as the presence of only left-handed weak interactions). We expect to see and look forward to—evidence of new physics beyond the Standard Model.

2.2 FLAVOR PHYSICS

IN THE Standard Model the complex phases of the 3×3 Kobayashi-Maskawa (KM) quark mixing matrix are the source of *CP* violation at the electroweak scale and have their origin in the quark mass matrix of the Yukawa sector of the theory. The study of *CP* violation and measurements of the KM matrix elements, including the complex phases, are very important for the development of a more fundamental understanding of nature.

In the KM model, *CP* violation is attributed to complex phases in the quark mixing matrix

$$\begin{pmatrix} V_{ud} & V_{us} & V_{ub} \\ V_{cd} & V_{cs} & V_{cb} \\ V_{td} & V_{ts} & V_{tb} \end{pmatrix}. \tag{2.1}$$

The nontrivial complex phases are typically assigned to the furthest off-diagonal elements V_{ub} and V_{td}. Unitarity of the KM matrix implies that $\sum_i V_{ij}^* V_{ik} = \delta_{jk}$ and $\sum_j V_{ij}^* V_{kj} = \delta_{ik}$, which gives the following relation involving V_{ub} and V_{td} :

$$V_{td}V_{tb}^* + V_{cd}V_{cb}^* + V_{ud}V_{ub}^* = 0. \tag{2.2}$$

This expression implies that the three terms form a closed triangle in the complex plane, as shown in Fig. 2.1. The three internal angles of this so-called "unitarity triangle" are definedas

$$\phi_1 \equiv \arg\left(\frac{V_{cd}V_{cb}^*}{V_{td}V_{tb}^*}\right), \phi \equiv \arg\left(\frac{V_{ud}V_{ub}^*}{V_{td}V_{tb}^*}\right), \phi \equiv \arg\left(\frac{V_{cd}V_{cb}^*}{V_{ud}V_{ub}^*}\right). \tag{2.3}$$

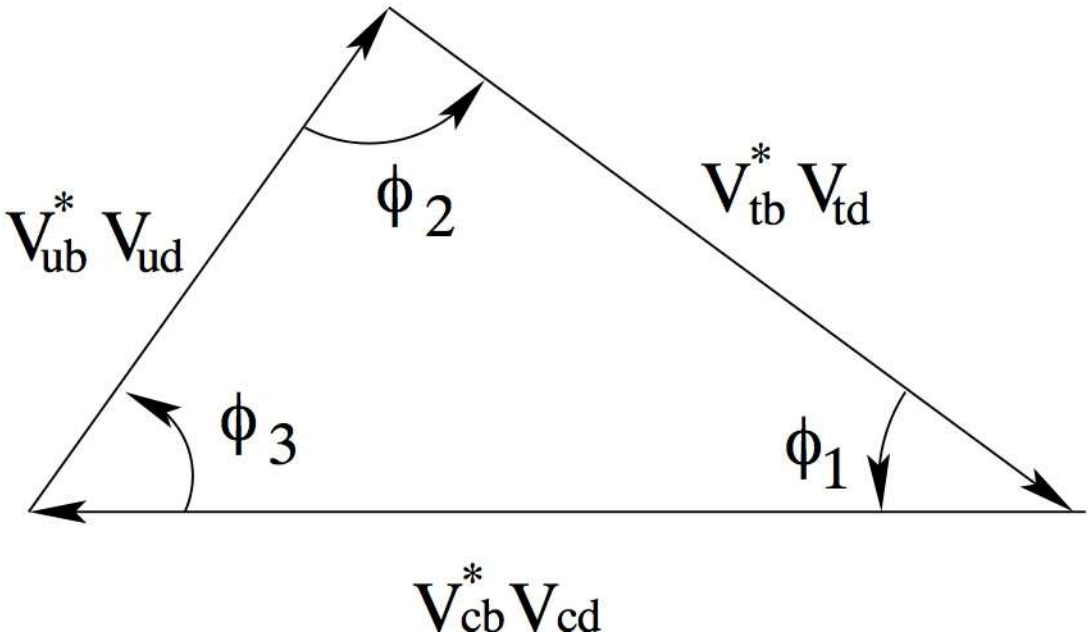

Figure 2.1: CKM Unitarity traingle.

Wolfenstein suggested a rather convenient approximate parameterization of the KM matrix [13],

$$\begin{pmatrix} 1-\lambda^2/2 & \lambda & \lambda^3 A(\rho - i\eta) \\ -\lambda & 1-\lambda^2/2 & \lambda^2 A \\ \lambda^3 A(1-\rho-i\eta) & -\lambda^2 A & 1 \end{pmatrix}, \tag{2.4}$$

where there are four parameters, λ, A, ρ, and η, that have to be obtained from experiment. Of the four, λ and A are relatively well determined; less is known about ρ and η.

2.3 THE $\Upsilon(4S)$

THE $\Upsilon(1S)$ MESONS are bound states of $b\overline{b}$ quarks with spin, parity and charge conjugation quantum numbers $J^{PC} = 1^{--}$. After the first observation of the $\Upsilon(1S)$ in proton-nucleon collisions by the CFS collaboration, the existence of the Υ meson was confirmed by experiments at CESR [9] and DORIS [8]. Fig. 2.2 shows the total e^+e^- annihilation cross section as a function of the CM energy in the region of the Υ resonances measured by CLEO [10].

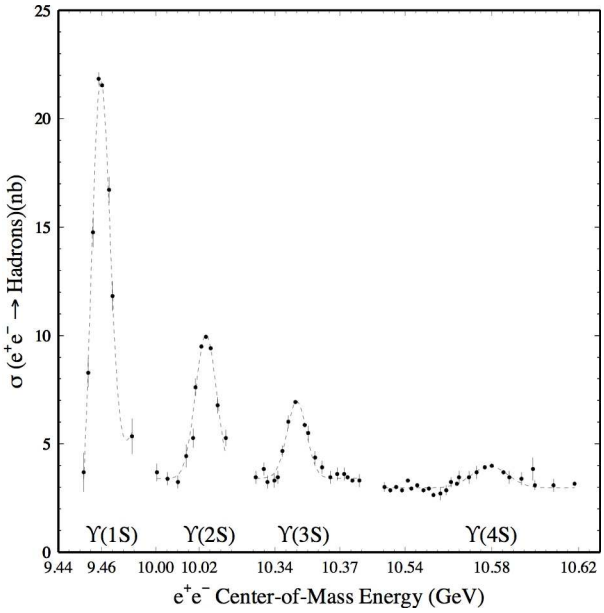

Figure 2.2: e^+e^- total cross section

The mass of the $\Upsilon(4S)$ meson is just above the threshold for decay into $B\overline{B}$ meson pairs, where B refers generically to a bound state of either $\overline{b}u$ or $\overline{b}d$ quarks. It decays about 96% of the time into such $B\overline{B}$ pairs [10]. The cross section of $\Upsilon(4S)$ production at its peak position is about 1/3 of that of total hadronic production $e^+e^- \to q\overline{q}$ $(q = u, d, s, c)$, which is often referred to as "continuum". Therefore, although KEKB is operating at the $\Upsilon(4S)$ resonance to produce $B\overline{B}$ pairs, it produces three times more $q\overline{q}$ events that constitute a major source of background to B physics. Due to the low invariant mass of the $q\overline{q}$ pair, the jets from these light quarks are produced with a significant boost factor. In contrast, the B and $\overline{B}$ mesons from $\Upsilon(4S)$ decay are generated nearly at rest, and so have a more spherical event structure. We will use this difference later to suppress continuum events with so-called shape variables. In order to study the $q\overline{q}$ contribution cleanly, KEKB is sometimes operated at 60 MeV below the $\Upsilon(4S)$ resonance. The data taken at the $\Upsilon(4S)$ resonance and 60

MeV below are referred to as "on-resonance" and "off-resonance" respectively. Around 10% of data taken by Belle are off-resonance. The ratio of the branching fraction of $\Upsilon(4S)$ to $B^0\overline{B^0}$ and B^+B^- has also been measured by CLEO [10] and is:

$$\frac{\mathscr{B}(\Upsilon(4S) \to B^+B^-)}{\mathscr{B}(\Upsilon(4S) \to B^0\overline{B^0})} = 1.04 \pm 0.07 \pm 0.04, \tag{2.5}$$

which is consistent with equal production rates for charged and neutral $B\bar{B}$ pairs. Here we follow the Particle Data Group (PDG) convention, which assumes an equal production rate [11].

2.4 HISTORY OF THE BELLE EXPERIMENT

THE BELLE EXPERIMENT started at KEK in Tsukuba, Japan, in 1994. The construction of KEKB was completed in 1998. After half a year of KEKB commissioning, the Belle detector was installed in the beam line in May 1999. Physics runs started in June 1999. Physics runs are divided into "experiments." The period and accumulated luminosity for each experiment upto April 2005 are listed in Table 2.1. The accumulated luminosity and peak luminosity of KEKB are shown in Fig. 2.3; as you can see, the daily measures (top three graphs) continue to rise, indicating continuous improvement in the operation of the accelerator. In May 2005, KEKB achieved the world record of the peak luminosity of 15.81×10^{33} cm^{-2}s^{-1} and up to June 12, 2006, KEKB accumulated a record integrated luminosity of $612\,fb^{-1}$. Today, about $1\,fb^{-1}$ of data is taken every day.

The main physics goal of Belle is to study *CP* violation in the *B* meson system. Additionally, Belle has made significant achievements in charm, τ, and two photon physics, as well as non-*CP* aspects of *B* physics.

2.5 THE KEKB ACCELERATOR

THE KEKB colliding-beam accelerator provides the electron-positron collisions at the heart of the Belle detector. It consists of two storage rings of 3.012 km length each, one for the 8 GeV electrons (High Energy Ring, HER) and one for the 3.5 GeV positrons (Low Energy Ring, LER), that were constructed inside the tunnel of the decommissioned TRISTAN accelerator. The rings are positioned 11 m underground. Since the two beams have different energies, separate beam pipes are used. To ensure that the circumference of each

Table 2.1: Experiment numbers and integrated luminosity.

ExpNo	Integrated luminosity (fb^{-1})			
	On resonance	Continuum	Energy scan	Total
3	0.02	0.002	0.009	0.03
5	0.24	0.019	—	0.26
7	5.86	0.589	0.084	6.53
9	4.38	—	—	4.38
11	8.32	1.216	0.124	9.66
13	10.8	1.209	0.065	12.1
15	12.8	1.412	—	14.2
17	12.1	0.848	—	12.9
19	29.1	3.645	—	32.7
21	4.41	—	—	4.41
23	6.30	1.449	—	7.75
25	25.9	1.675	—	27.8
27	25.6	3.755	—	29.4
29	—	—	—	—
31	18.1	2.425	—	20.5
33	17.7	2.734	—	20.4
35	16.8	1.959	—	18.7
37	62.6	6.091	—	68.7
39	50.3	—	—	50.3
41	64.9	—	—	64.9
Total	376.2	29.03	0.283	405.6

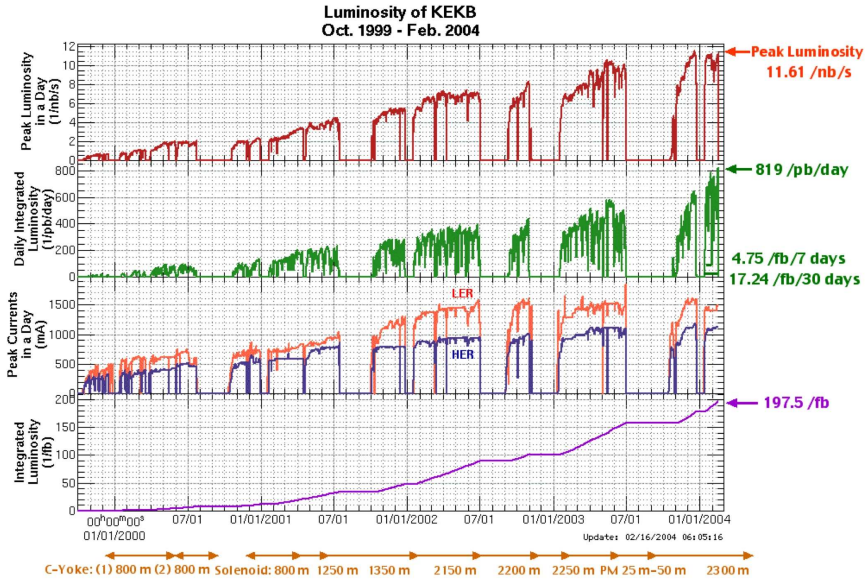

Figure 2.3: KEKB luminosity history.

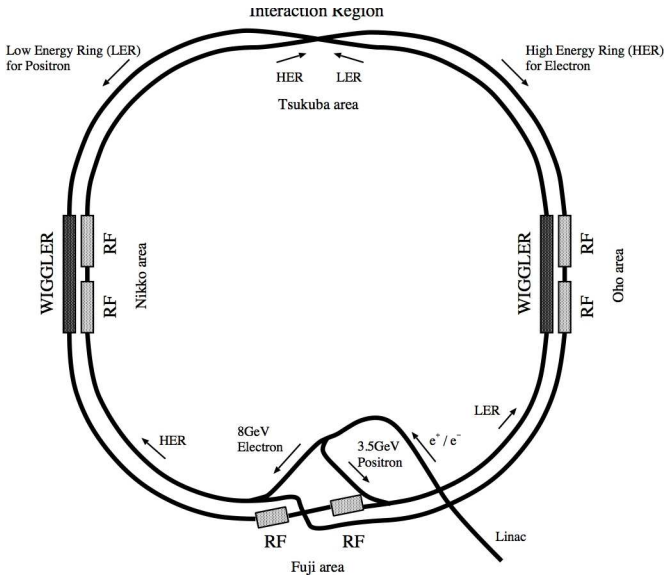

Figure 2.4: KEKB e^+e^- collider configuration.

ring is precisely the same, a second cross-over of the two beam pipes occurs in the "Fuji" area. The configuration of the KEKB storage ring is illustrated in Fig. 2.4. The electron and positron beams are created and accelerated to their final energy in the linear accelerator (Linac) and then injected into KEKB in the Fuji area. The two beams cross at the interaction point (IP) in the Tsukuba experimental hall at the center of the Belle detector [12]. At the IP, electrons and positrons collide with a finite crossing angle of ± 11 mrad. In order to compensate for the energy loss of the beams due to radiation as they circulate in KEKB, two kinds of RF cavities—normal conductive cavities called Accelerator Resonantly coupled with Energy Storage (ARES) and superconducting cavities (SCC)— are installed. The positron beam passes through wigglers that are installed in order to reduce the longitudinal damping time of the LER.
KEKB was designed to achieve a luminosity, $\mathscr{L}$, of 10^{34} cm^{-2}s^{-1} based on the formula:

$$\mathscr{L} = \frac{1}{2er_e}\xi_y\left(\frac{\gamma I}{\beta_y^*}\right)_{\pm} = (2.2\times 10^{-34})\xi_y\left(\frac{IE}{\beta_y^*}\right)_{\pm}, \tag{2.6}$$

where e is the elementary electric charge, r_e is the classical electron radius, ξ_y is the vertical beam tune shift parameter, β_y^* is the vertical β function at the IP, γ is the Lorentz boost factor, I is the beam current and E is the beam energy. The units of L, I, E and β_y^* are given in cm^{-2}s^{-1}, A, GeV and cm respectively. We assume that β_y^* and ξ_y are the same for both beams, because unequal parameters cause incomplete overlap of both the beams during the

Table 2.2: Main parameters of KEKB.

Ring		LER	HER	Unit
Energy	E	3.5	8.0	GeV
Circumference	C	3016.26		m
Luminosity	$\mathscr{L}$	1×10^{34}		$cm^{-2}s^{-1}$
Crossing angle	θ_x	±11		mrad
Tune shifts	ξ_x/ξ_y	0.039/0.052		m
Beta function at IP	β_x^*/β_y^*	0.33/0.01		
Beam current	I	2.6	1.1	A
Natural bunch length	σ_z	0.4		cm
Energy spread	σ_E	7.1×10^{-4}	6.7×10^{-4}	
Bunch spacing	s_B	0.59		m
Particle/bunch	N	3.3×10^{10}	1.4×10^{10}	
Emittance	$\varepsilon_x/\varepsilon_y$	$1.8\times10^{-8}/3.6\times10^{-10}$		m
Synchrotron tune	ν_s	0.01∼0.02		
Betatron tune	ν_x/ν_y	45.52/45.08	47.52/46.08	
Momentum compaction factor	α_p	$1\times10^{-4}\sim2\times10^{-4}$		
Energy loss/turn	U_0	0.81†/1.5‡	3.5	MeV
RF voltage	V_c	5∼10	10∼20	MV
RF frequency	f_{RF}	508.887		MHz
Harmonic number	h	5120		
Longitudinal damping time	τ_ε	43†/23‡	23	ms
Total beam power	P_b	2.7†/4.5‡	4.0	MW
Radiation power	P_{SR}	2.1†/4.0‡	3.8	MW
HOM power	P_{HOM}	0.57	0.15	MW
Bending radius	ρ	16.3	104.5	m
Length of bending	l_b	0.915	5.86	m

†: without wigglers, ‡ with wigglers.

collision. This assumption requires $I_+E_+ = I_-E_-$, so the LER current is higher than the HER current. The design parameters of KEKB are listed in Table 2.2.

2.6 THE BELLE DETECTOR

THE BELLE DETECTOR is a general purpose detector surrounding the interaction point (IP) to detect the particles from e^+e^- collisions. In order to study the B meson and other related physics at KEKB, the Belle detector consists of a beam pipe, Extreme Forward Calorimeter (EFC), Silicon Vertex Detector (SVD), Central Drift Chamber (CDC), Aerogel Čerenkov Counter (ACC), Time of Flight Counter (TOF), Electromagnetic Calorimeter (ECL), solenoid magnet, K-Long (K_L) and Muon (μ) detector (KLM), trigger and Data Acquisition system (DAQ), and off-line software and computing facilities. We define

the right-handed coordinate system for Belle by aligning the z-axis with the positron beam and its positive direction opposite the motion of the positrons. The y-axis points upwards and the x-axis is perpendicular to both (pointing away from the center of the KEKB rings). The polar angle θ is measured relative to the positive z-axis. Due to the boost of the $\Upsilon(4S)$ resonances, the components of Belle are asymmetrical in z. This is apparent in Fig. 2.5 and 2.6, where the components are shifted towards the forward direction relative to interaction point (IP). The detector is divided into three regions: the barrel section, which is parallel to the beam axis, and the two endcaps, which extend radially from the beam axis at the forward and backward ends of the detector. The polar angle coverage of each of the three sections is shown in Table 2.3.

Table 2.3: Polar angle coverage of the Belle detector.

Region	Polar angle coverage
Barrel	$34^\circ < \theta < 127^\circ$
Forward endcap	$17^\circ < \theta < 34^\circ$
Backward endcap	$127^\circ < \theta < 150^\circ$

Following is a brief description of the components of the Belle detector.

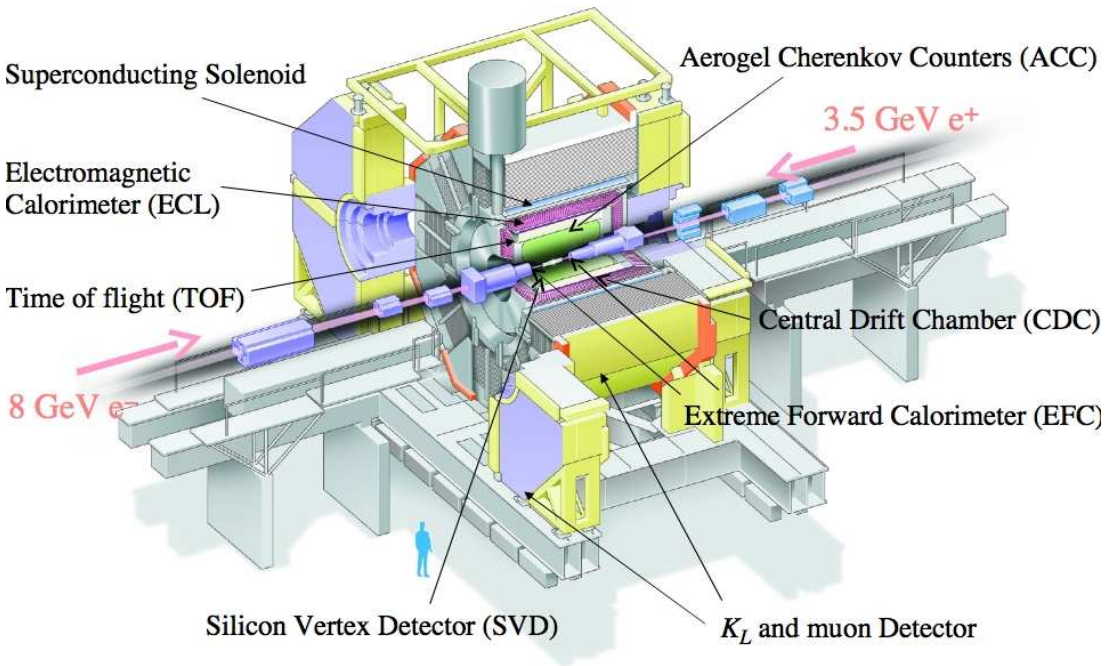

Figure 2.5: Cut away view of the Belle detector

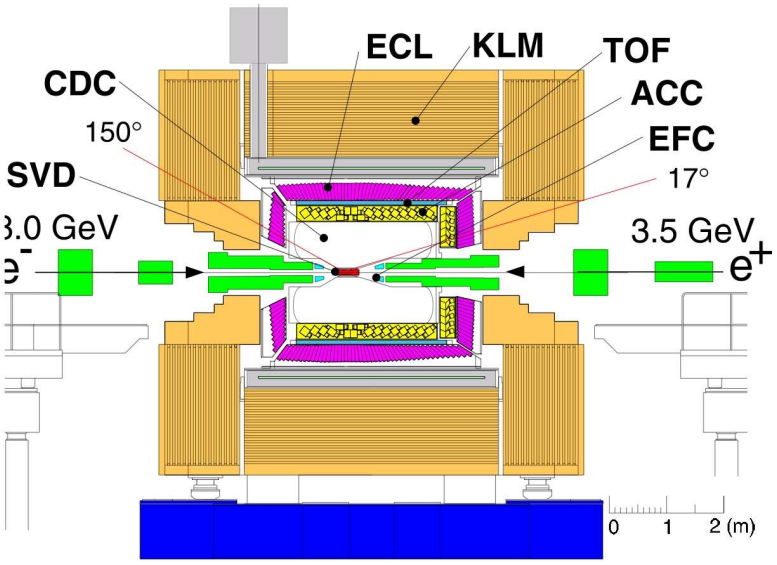

Figure 2.6: Side view of the Belle detector

Beam Pipe

The beam pipe is designed to minimize multiple scattering and energy loss of charged particles between their production and their measurement in the SVD and CDC, since these effects degrade the vertex resolution. The beam pipe configuration is shown in Fig. 2.7. It consists of two beryllium cylinders, with radii 20.0 mm and 23.0 mm, and with 0.5 mm thickness for each. The 2.5 mm gap between cylinders is filled with helium gas for cooling. (The beam-pipe is heated by ohmic currents and high order mode losses in the material as the beam bunches circulate.) The outer beryllium cylinder is covered with a 20 μm thick gold film to absorb low energy X-rays from the HER. The total material thickness of the beam pipe corresponds to 0.9% of a radiation length.

Extreme Forward Calorimeter (EFC)

The extreme forward calorimeter is designed to extend the polar angle coverage for the Belle detector. Photons and electrons are measured by the EFC in the extreme forward and backward area that is not covered by the ECL (see section 2.6). The EFC is placed around the beam pipe close to the IP, where a very high radiation level exists. The radiation-hard crystal bismuth germanate (BGO), $Bi_4Ge_3O_{12}$, is used as the scintillating material, and a photodiode is used to read out the signal. The EFC covers the polar angle range

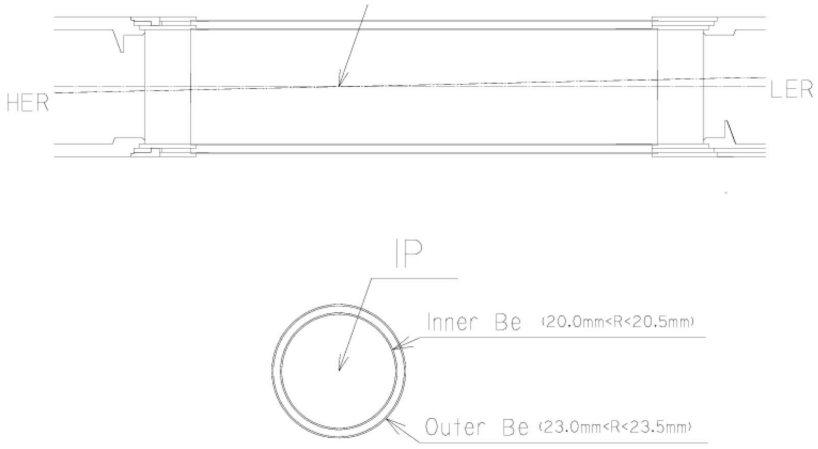

Figure 2.7: Configuration of beam pipe

$6.4° < \theta < 11.5°$ for the forward detector and $163.3° < \theta < 171.2°$ for the backward detector. Both forward and backward detectors are segmented into 32 sections in ϕ and 5 in θ. Figure 2.8 shows the EFC configuration. The forward and backward crystals correspond to 12 and 11 radiation lengths respectively. The EFC is also used for online luminosity monitoring based on the rate of Bhabha scattering mechanism. Figure 2.9 shows the history of a typical beam fill in the early days of operation. The real Bhabha rate is calculated by subtracting the EFC fake rate ($< 10\%$) from the EFC raw Bhabha rate.

Silicon Vertex Detector (SVD)

The primary purpose of the SVD is to determine the z-axis position of the B meson decay vertex, which is essential for time-dependent CP analysis. Figure 2.10 shows the configuration of the original SVD in a side and end view perspective.

It has three layers of double-sided silicon strip detectors (DSSD) and covers the region of $23° < \theta < 139°$, corresponding to 86% of the total solid angle. As shown in the end view, the three layers consist of 8, 10 and 14 full ladders respectively for the inner, middle and outer layers around the beam axis. Each full ladder is made of two half-ladders and each half-ladder contains one or two DSSDs which are supported by boron-nitride (BN) ribs sandwiched with carbon-fiber reinforced plastic (CFRP). In total, there are 32 ladders and 102 DSSDs. The DSSDs are essentially reverse-biased diode-strip detectors. They are produced by Hamamatsu Photonics and were originally designed for the DELPHI micro-vertex detector [14]. They are $300\mu m$ thick and have an area

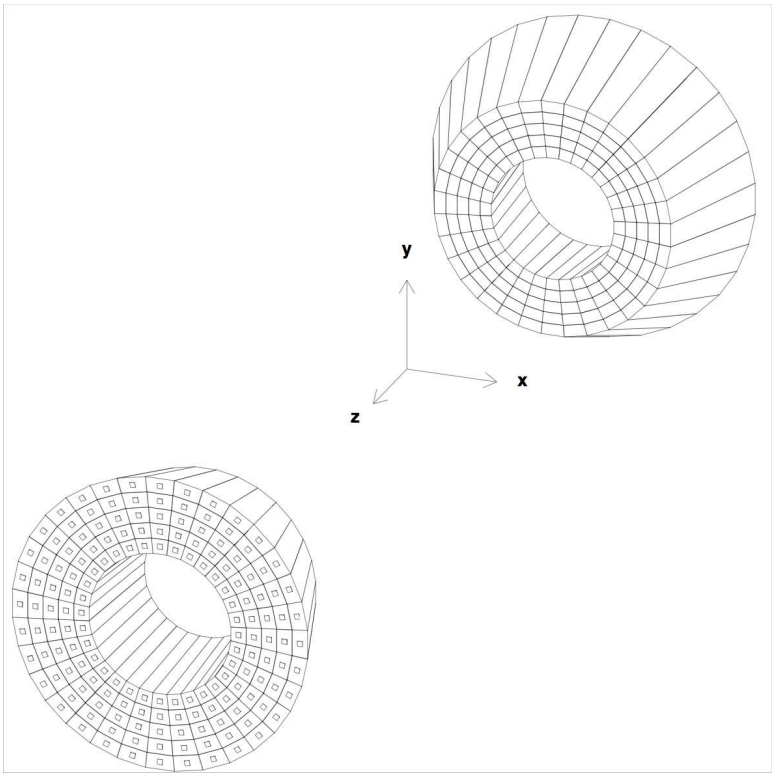

Figure 2.8: EFC configuration

of 57.5 $\times$ 33.5 mm^2. Each DSSD contains 1280 sense strips and 640 readout pads. One side is p doped silicon with p^+ readout strips parallel to the beam to measure ϕ. The other side has n^+ strips oriented perpendicular to the beam to measure the z coordinate. The p^+ and n^+ strips have pitches of 24μm and 42μm, respectively. As shown in Fig. 2.11, a charged particle traversing a DSSD will create electron-hole pairs, which will drift to the appropriately biased side of the DSSD, where their charge is deposited and read out.

The signals from the DSSDs are read out by VA1 chips [15] mounted on a ceramic hybrid. As the VA1 has 128 channels, five chips are mounted on each hybrid to read out all 640 pads on a DSSD. The VA1 chips are fabricated with a 1.2μm CMOS process by Austrian Micro Systems and can tolerate radiation levels of up to 200 krad. Signals from the VA1 chips are digitized by flash analogue-to-digital converters (FADCs), which are located in the adjacent Belle electronics hut. Online digital signal processors in the FADC modules perform common mode noise subtraction, data sparsification and data formatting. As mentioned before, the main purpose of the SVD is to determine the B meson decay vertex and to improve the charged tracking. For studies of time dependent CP asymmetries, the z-axis distance of the two B vertices for an $\Upsilon(4S)$ decay must be measured with the precision of about 100μm . As shown in

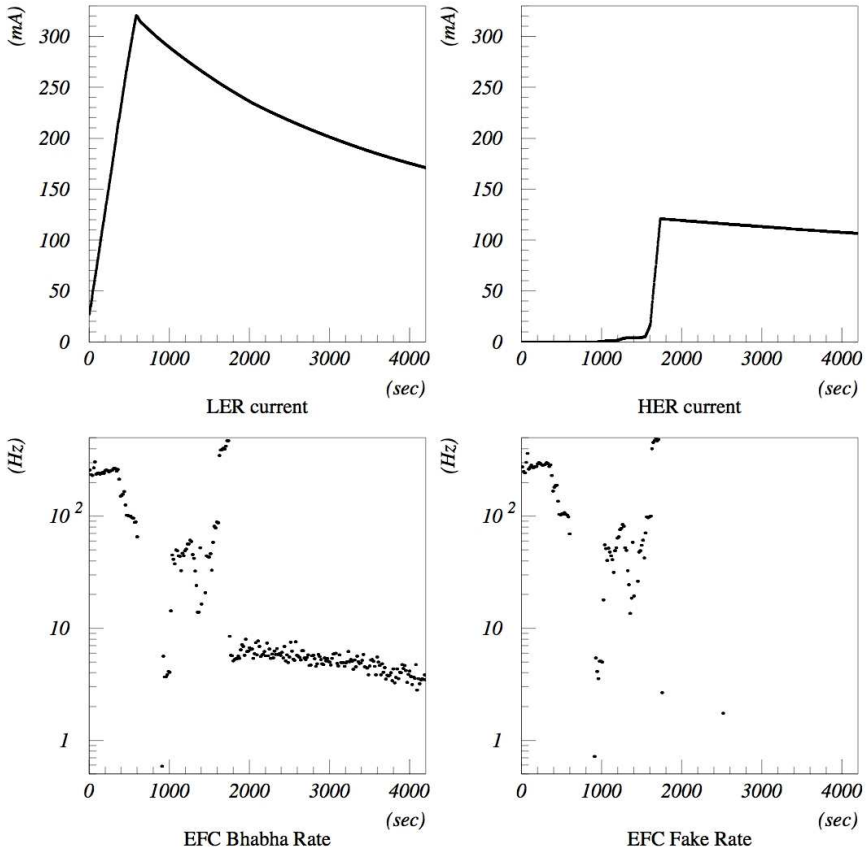

Figure 2.9: EFC rates and the beam current during beam injection

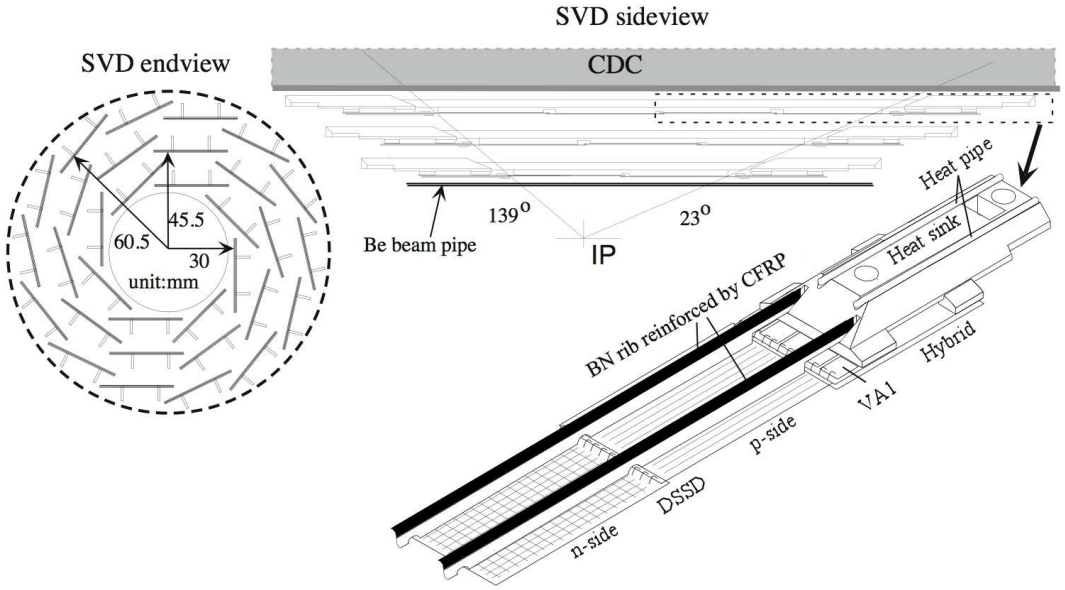

Figure 2.10: Configuration of SVD1

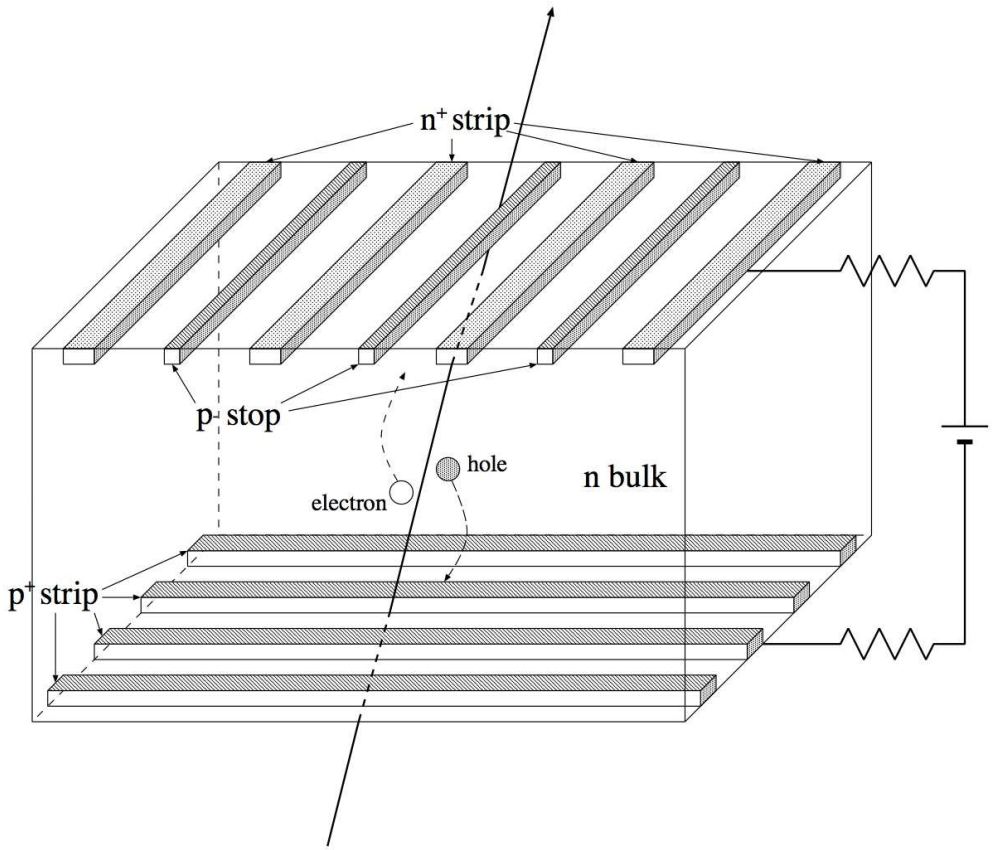

Figure 2.11: Double-sided silicon-strip detector from the SVD

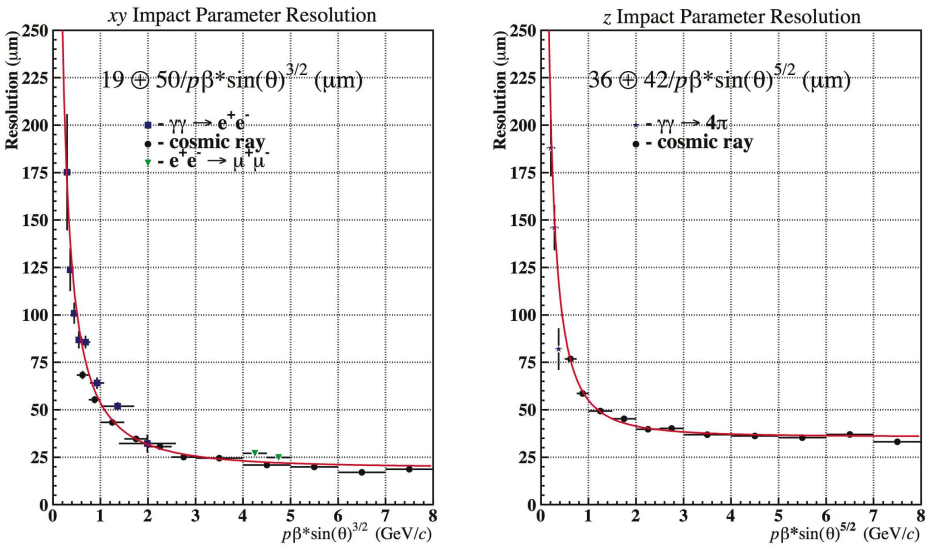

Figure 2.12: Impact parameter resolution of charged tracks with associated SVD hits.

Fig. 2.12, the momentum and angular dependences of the impact parameter (the closest approach of tracks to the IP) resolution behave like the following:

$$\sigma_{xy} = 19 \oplus 50(p\beta \sin^{3/2}\theta)^{-1}\mu m \tag{2.7}$$

$$\sigma_{z} = 36 \oplus 42(p\beta \sin^{5/2}\theta)^{-1}\mu m, \tag{2.8}$$

where $\oplus$ indicates a quadratic sum. The momentum p is given in units of GeV/c. The impact parameter resolution for a 1 GeV track is around 55μm.
In summer 2004, the three-layer SVD1 was replaced with a four-layer SVD2. Several improvements were made. SVD2 has a larger angular acceptance of $17° < \theta < 150°$. The innermost layer is closer to the primary interaction point at a distance of 2 cm instead of 3 cm in SVD1. This is possible with a significantly smaller beam pipe. The fourth layer is accommodated by a redesign of inner region of the CDC (see section 2.6). The four layers of SVD2 contains 6, 12, 18 and 18 full ladders from inside to outside as shown in Fig. 2.13. Each half ladder consist of 1, 2 or 3 DSSDs. The DSSDs for SVD2 have 512 readout channels in both $r-z$ and $r-\phi$, or in total 110,592 readout channels. The number of DSSDs for each half ladder is displayed in Table 2.4. A hadronic event recorded by SVD2 is displayed in Fig. 2.14.
For the SVD1, the limited radiation tolerance of the VA1 front-end readout chip was an important issue. It was replaced by a VA1TA chip [16], manufactured by IDEAS. It is implemented in a 0.25μm CMOS process and is expected to

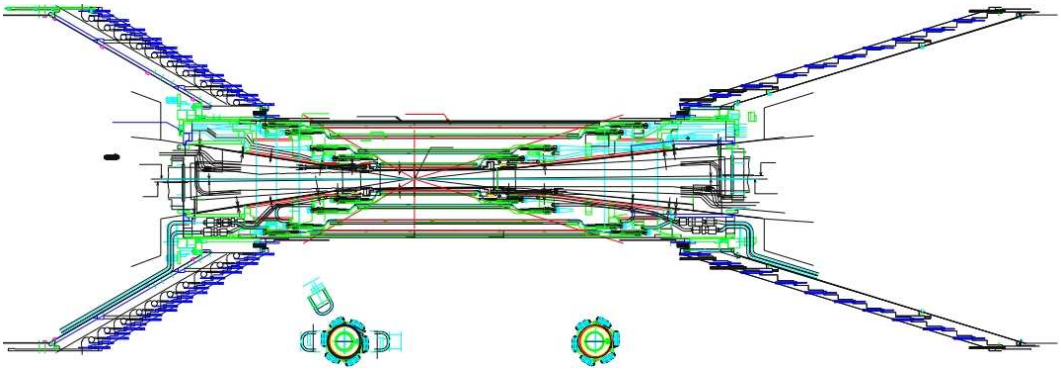

Figure 2.13: Sideview of the SVD2 geometry.

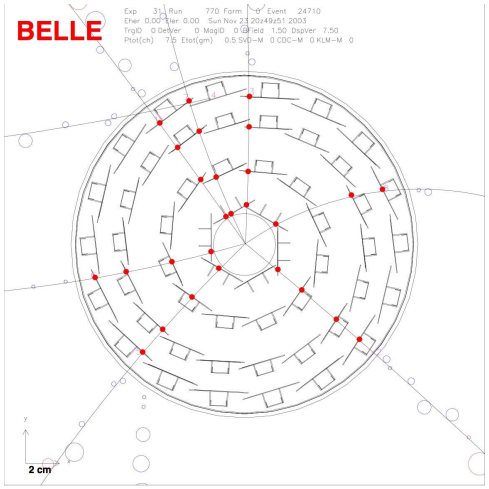

Figure 2.14: Frontview of the SVD2: A typical hadronic hit.

Table 2.4: Number of detectors in each half ladder of the SVD.

number of DSSDs in	forward / backward	half ladder
Layer 1:	1	1
Layer 2:	1	2
Layer 3:	2	3
Layer 4:	3	3

have a stable performance up to a radiation dose of at least 20 MRad [17]. More information on SVD1 and SVD2 can be found in Refs. [18, 19, 12].

Central Drift Chamber (CDC)

The main purpose of the CDC is to measure the momentum and the energy deposition of charged particles (dE/dx). The dE/dx information is used to provide information for particle identification (PID), i.e. identifying kaons, pions, protons and electrons. All components in Belle out to the ECL (described in section 2.6) are contained in a 1.5 T magnetic field supplied by a solenoid magnet (see section 2.6). The field is nearly uniform and directed in the positive z direction. When a charged particle moves through a magnetic field, it follows a helical path along the field direction. The helix can be decoupled into a circular motion in a plane, being defined by three parameters, and a motion in a straight line, being defined by two parameters. From these five independent parameters it is possible to determine the closest approach of the helix to the IP and the components of the particle's momentum parallel and perpendicular to the magnetic field. These momentum and impact parameter measurements are the primary purpose of the CDC. Figure 2.15 shows the CDC structure. The length of CDC is 2,400 mm, and the inner and outer radii are 83 and 874 mm, respectively. It covers the polar angle range from 17° to 150°. The CDC is a small cell drift chamber consisting of 50 anode sense wire layers and three cathode strip layers. The 50 anode layers consist of 32 axial wire layers and 18 small-angle stereo wire layers. The axial wires are parallel to the z direction and the crossing angles between the stereo wires and z-axis vary from 42.5 mrad to 72.1 mrad. There are 8,400 readout channels for the anode wires and 1792 channels for the cathode strips. The cell configuration is shown in Fig. 2.16. We obtain three-dimensional track information from the anode wires. As well as tracking, the CDC provides a vital component to the particle identification (PID) system. From the pulse height at the anode wires, a measure of the mean energy deposition due to ionization of the gas (dE/dx) can be obtained for a particle traversing the CDC. As the energy loss depends on the boost of the particle, for a given momentum, dE/dx will depends on particle species. A 50% helium-50% ethane mixed gas fills the chamber to minimize the multiple Coulomb scattering contribution. The pulse height and drift time of the ionization are measured to provide the information of energy deposit and the distance from the sensor-wire. The transverse momentum (p_t) resolution is shown in Fig. 2.17; the resolution is a function of p_t itself behaving like

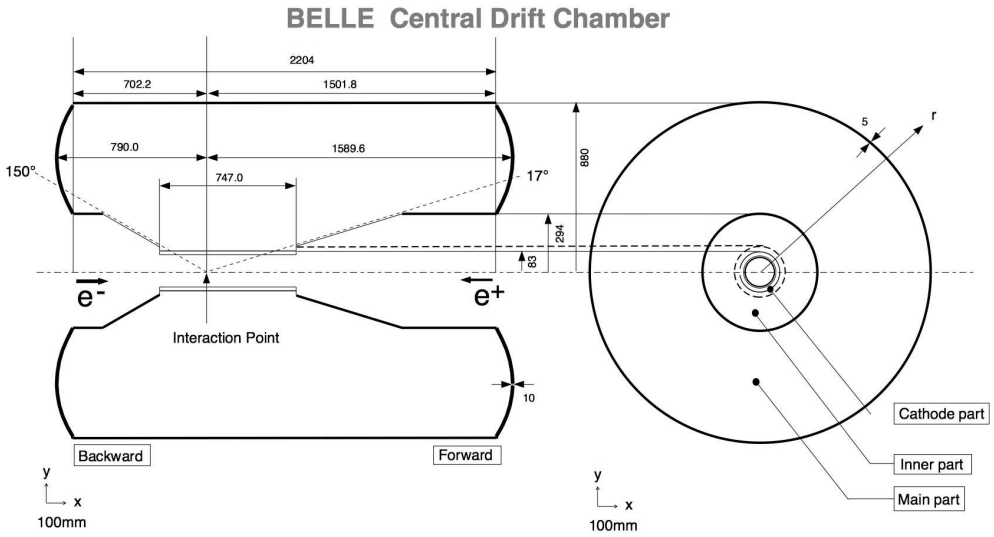

Figure 2.15: Configuration of CDC.

$(0.19p_t \oplus 0.30)\%$. The dE/dx resolution is 7.8% for pions from K_s decay and 6% for energetic electrons and muons. The scattering distribution for dE/dx is shown at Fig. 2.18. The separation between the different particles can clearly be seen. The CDC is described in [12, 20] in more detail.

Aerogel Čerenkov Counter (ACC)

The aerogel Čerenkov counter is designed for $K^{\pm}$ and $\pi^{\pm}$ separation with momentum between 1.2 GeV/c and 3.5 GeV/c. The ACC detects the Čerenkov light emitted when a particle travels through a medium faster than the speed of light in that medium. Specifically, for a medium of refractive index n, Čerenkov light is emitted if the velocity of the particle, β, satisfies:

$$n > 1/\beta = \sqrt{1 + (mc/p)^2}, \tag{2.9}$$

where m and p are the mass and momentum of the particle, respectively. Thus, depending on the refractive index of the medium, there will be a range of velocity for which pions emit Čerenkov radiation but kaons do not. The barrel ACC consists of 960 aerogel counter modules segmented into 60 cells in ϕ direction. The forward end-cap ACC consists of 228 modules that are arranged in 5 concentric layers. There are five different types of aerogel with refractive indices of n = 1.010, 1.013, 1.015, 1.020 and 1.028, arranged according to polar angle. The alignment is shown in Fig. 2.19. The typical counter module consists of silica aerogel filled in 0.2 mm-thick aluminum boxes and viewed with one or two fine mesh-type photomultiplier tubes (FM-PMTs). The FM-PMTs

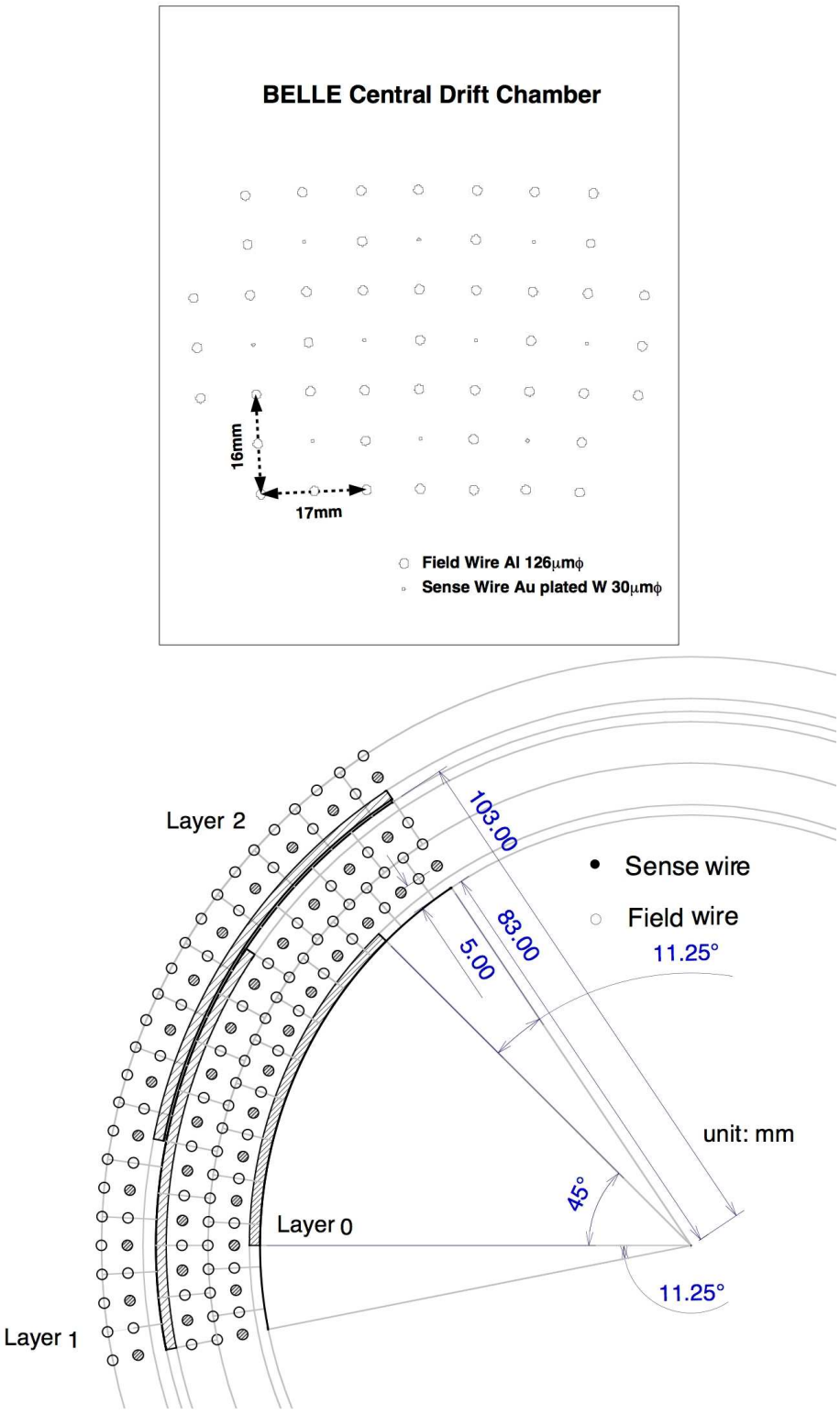

Figure 2.16: CDC cell structure.

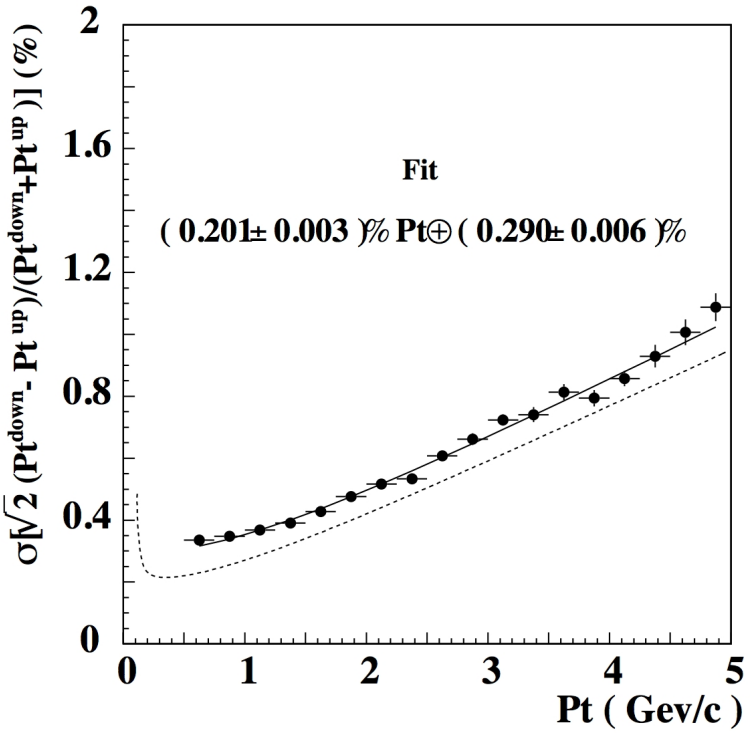

Figure 2.17: The CDC p_t resolution. The solid curve is the fitted result and the dotted curve is the ideal expectation for $\beta = 1$ charged track.

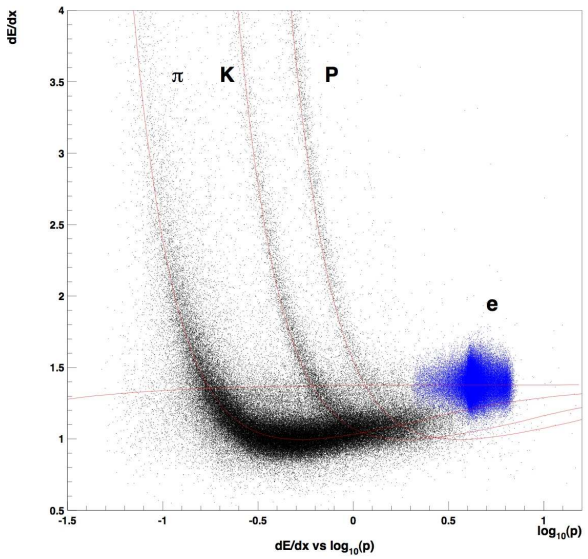

Figure 2.18: dE/dx distribution versus momentum.

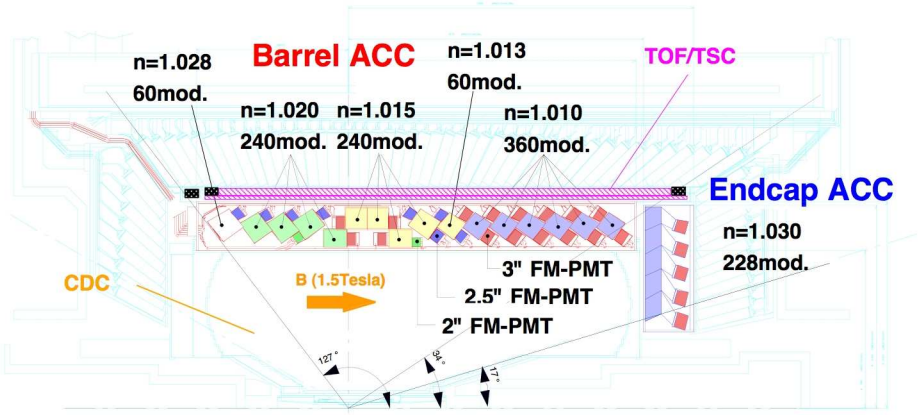

Figure 2.19: Alignment of ACC.

can be operated well in a 1.5T magnetic field. Figure 2.20 shows a schematic drawing of the ACC module. There are 1560 readout channels in the barrel part and 228 in end-cap. A more detailed description of the ACC can be found in Reference [21].

Time of Flight Scintillator (TOF)

The time of flight detector provides complementary information for the particle identification in the ACC in order to distinguish $K^{\pm}$ and $\pi^{\pm}$ mesons up to 1.2 GeV/c, where the K/π separation power for ACC and CDC is less effective. The TOF also provides fast timing signals for the trigger system, which requires a timing resolution of 100 ps. The flight time, T, for a particle of mass m to travel a length L is given by:

$$T = \frac{L}{c}\sqrt{1+(\frac{mc}{p})^2}. \tag{2.10}$$

The TOF measures the time elapsed between the collision at the IP and its passage through the TOF barrel. Thus a particle's mass can be calculated once its momentum is known. This enables particle species to be differentiated by their measured times-of-flight. The mass distribution calculated from TOF measurements is shown in Fig. 2.21. Clear separation between kaons, pions and protons can be seen. The module TOF structure is shown in Fig. 2.22. TOF counters and TSCs are made of fast scintillators and FM-PMTs that are mounted

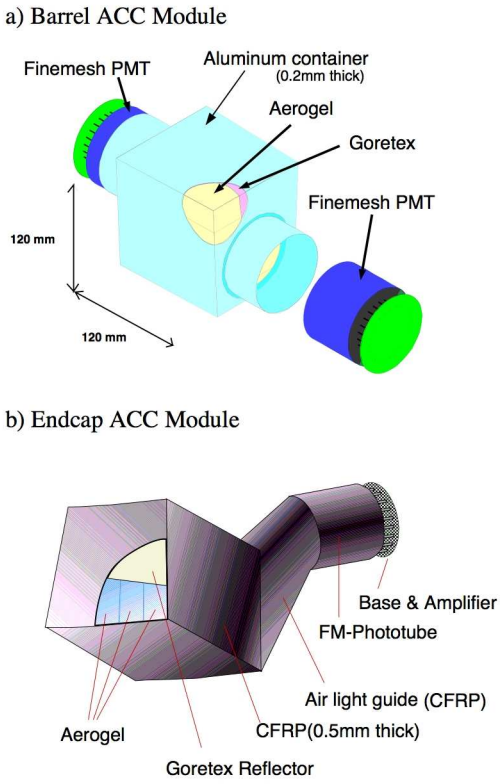

Figure 2.20: Schematic drawing for typical ACC module: (a) is the barrel ACC module and (b) is the forward end-cap module.

directly to the scintillator. Two TOF counters (4 cm thick) and one TSC (0.5 cm thick) form one module. The TSC is used to produce trigger signals, taking a coincidence with the TOF counters to reduce the trigger hit rate. The TOF system consists of 64 TOF modules located in the barrel region just outside the ACC and covers the polar angle region $33^\circ < \theta < 121^\circ$. Each module is made up of two TOF counters, read out by two FM-PMTs attached at both ends, and one trigger scintillation counter (TSC), read out by one FM-PMT attached at the backward end. The time resolution of the TOF scintillators is $\sigma_t = 100$ ps. The TOF hit efficiency is 95% for single-end hits and 88% for both-end hits in $e^+e^- \to \mu^+\mu^-$ pair events. For more information on the TOF system, see Refs. [12, 22]. Information from the TOF combined with the ACC and the dE/dx measurement from the CDC give the Belle detector more than a 3σ separation between charged kaons and pions over the whole momentum range up to 3.5 GeV/c.

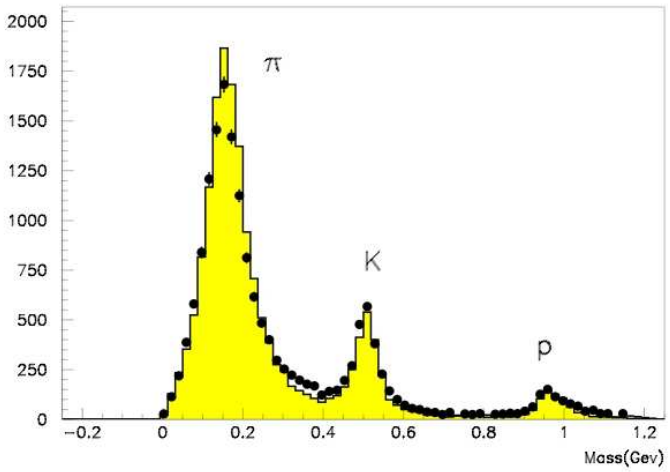

Figure 2.21: Hadron mass distributions calculated from TOF measurements for particles with momentum below 1.2 GeV/c. The points are from data, the shaded histogram is from Monte Carlo.

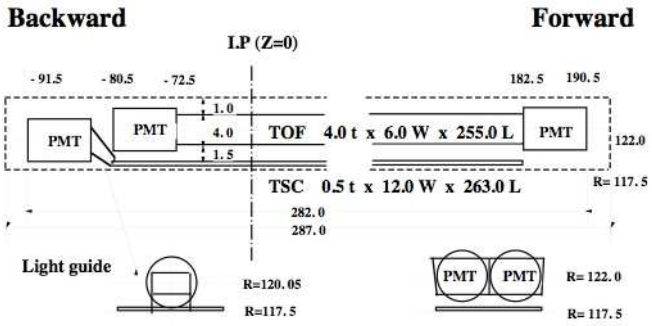

Figure 2.22: TOF Configuration.

Electromagnetic Calorimeter (ECL)

The electromagnetic calorimeter (ECL) measures the energy and position of photons from π^0 decays and radiative B decays with high efficiency and good resolution for energy and position. The ECL is also used for electron identification. In addition to this the ECL information is significantly used for the reconstruction of the K_L mesons which are poorly measured in the Belle detector as they don't decay inside the detector. The analysis K_L forms an important part of this dissertation. is The ECL is composed of an array of tower-shaped CsI(Tℓ) crystals. Each crystal is arranged so that it points to the interaction point. (There is a small tilt angle so that photons do not pass through a gap between crystals without interacting.) Figure 2.23 and Table 2.5 shows the ECL

Table 2.5: Geometrical configuration of the ECL.

	θ coverage	θ seg.	ϕ seg.	#	Position
Forward endcap	$12.4^\circ < \theta < 31.4^\circ$	13	48 to 144	1152	$z = 196$ cm
Barrel	$32.2^\circ < \theta < 128.7^\circ$	46	144	6624	$r = 125$ cm
Backward endcap	$130.7^\circ < \theta < 155.1^\circ$	10	64 to 144	960	$z = 196$ cm
Total				8736	

configuration.
The length of each crystal is 30 cm, which corresponds to 16.2 radiation lengths. Each crystal is read out by a pair of silicon PIN photodiodes. The energy resolution of the ECL is measured to be [23]:

$$\frac{\sigma_E}{E} = \frac{0.0066}{E} \oplus \frac{1.53}{E^{1/4}} \oplus 1.18(\%), \tag{2.11}$$

where the energy E is given in GeV. Here, the first term is from the contribution of the electronic noise, while the second term and part of the third term come from incomplete containment of the electromagnetic shower. The third term also includes systematic effects such as the uncertainty of the calibration of the light output from each crystals. The spatial resolution is found to be $0.27 \oplus 3.4/\sqrt{E} \oplus 1.8/E^{1/4}$ mm. The energy and position resolutions are shown in Fig. 2.25. In addition to the measurement of the energy of photons and electrons, the ECL plays an important role for electron identification: a charged track that points at an ECL cluster is identified as an electron (or positron) if the energy and momentum are consistent, among other criteria. The ECL also provides trigger information and online luminosity information [24]. The trigger system is described in section 2.7.

Solenoid Magnet

The superconducting solenoid provides a 1.5 T magnetic field parallel to the beam pipe for charged particle momentum measurement. The superconducting coil consists of a single layer of niobium-titanium-copper alloy embedded in a high purity aluminum stabilizer. The coil is wound around the inner surface of an aluminum support cylinder of 3.4 m diameter and 4.4 m length. Indirect cooling is provided by a liquid helium circulation through a tube on the inner surface of the aluminum cylinder. The layout of the superconducting solenoid is shown in Fig. 2.26.

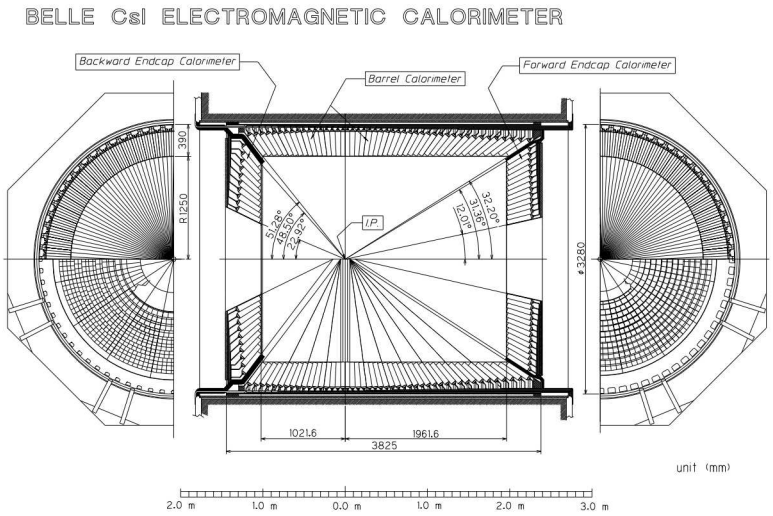

Figure 2.23: ECL configuration

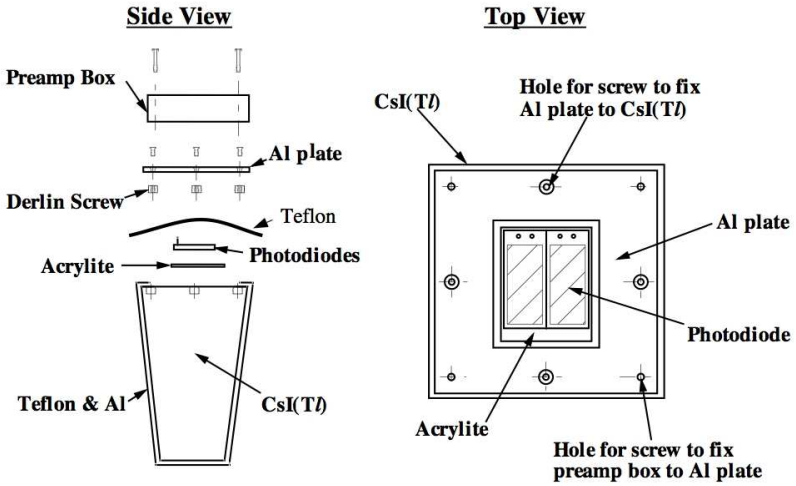

Figure 2.24: Mechanical structure of the ECL counter.

K_L and Muon Detector (KLM)

The K_L and muon detector (KLM) is designed for detection of K_L mesons and muons with momentum larger than 600 MeV/c. The detector is placed outside the solenoid and consists of 15 layers of Resistive Plate Counters (RPC) with 14 layers of 4.7 cm thick iron plates in the barrel region and 14 RPC layers in the endcap region. One RPC super-layer contains two RPC planes to provide θ and ϕ information. The iron plate is also used as return yoke for the magnetic field produced by the super conducting solenoid. The configuration of an RPC is shown in Fig. 2.27. The KLM covers the polar angle region of $20^\circ < \theta < 155^\circ$. Signals are read out from cathode strips in both θ and ϕ direc-

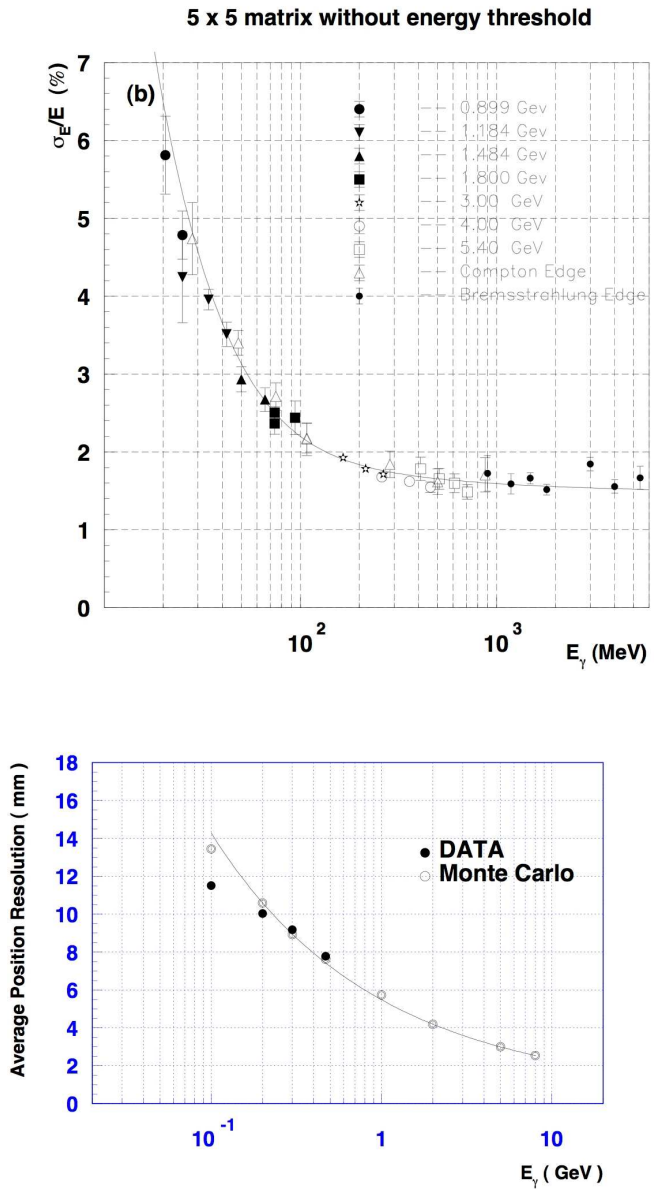

Figure 2.25: Energy (left) and position (right) resolutions of the ECL.

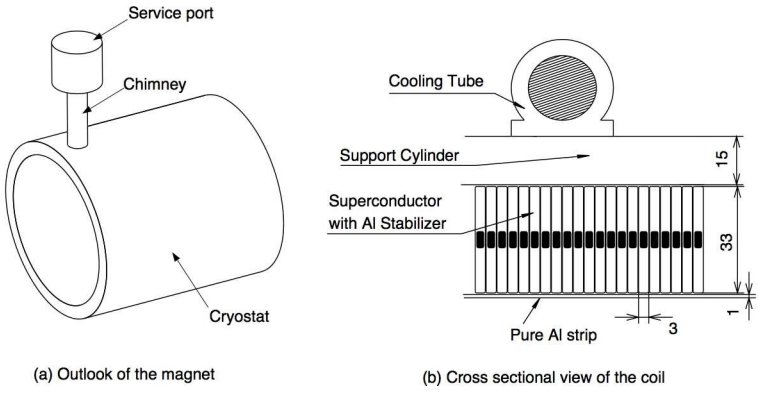

Figure 2.26: Superconducting coil.

tions. There are 21,856 readout channels for the barrel detector and 16,126 for the two endcap detectors. The position resolution for K_L mesons is 30 mrad for both θ and ϕ and the time resolution is a few nanoseconds. All the material in the Belle detector up to the KLM corresponds to about one hadronic interaction length for K_L mesons. The iron plates in the KLM provide a further 3.9 interaction lengths of material, which is necessary for detecting K_L mesons with high efficiency. When the K_L meson interacts with matter, it initiates a shower of hadrons, leaving a cluster of hits in the KLM that is not associated with a charged track. Muons can be discriminated from K_L mesons as they will have an associated charged track and a line of KLM hits rather than a shower pattern. For muons with a momentum of above 1 GeV/c or more, the KLM has a detection efficiency greater than 90% with a fake rate of about 2% (from non interacting pions and kaons).

2.7 TRIGGER AND DATA ACQUISITION

THE ROLE OF THE TRIGGER is to decide when the various subsystems of the Belle detector should record an event. Once a particular particle collision satisfies the trigger criteria, data from all the subsystems are read out and stored for possible use. The word *event* is used interchangeably to represent the physical particle collision or the stored data representing the collision. The decision to read out is based on criteria carefully chosen to remove background events while retaining events of interest at a high efficiency. Once an event is triggered, the data acquisition (DAQ) system transfers the raw data from the detector to the data storage system. The main sources of background events are undesirable interactions between the electron-positron beams, collisions of a beam particle with a residual gas molecule or with the beam-pipe, and synchrotron radiation from the beams. Events of interest are primarily hadronic ($e^+e^- \to q\bar{q}$ or $e^+e^- \to \Upsilon(4S) \to B\bar{B}$) and QED events ($e^+e^- \to e^+e^-$ or $e^+e^- \to \mu^+\mu^-$ or $e^+e^- \to \tau^+\tau^-$), used for physics analyses as well as detector calibration and luminosity measurements. For this analysis the hadronic events are of interest and the following discussion focuses on the hadronic trigger. Event rates for both physics and background events at the design luminosity of 10^{34} cm^{-2}s^{-1} are about 100 Hz each; but to accommodate higher backgrounds, the trigger is designed to operate up to 500 Hz. Figure 2.28 shows an overview of the Belle trigger system. It consists of the level 1 hardware trigger, the level 3 software trigger implemented by an online computer

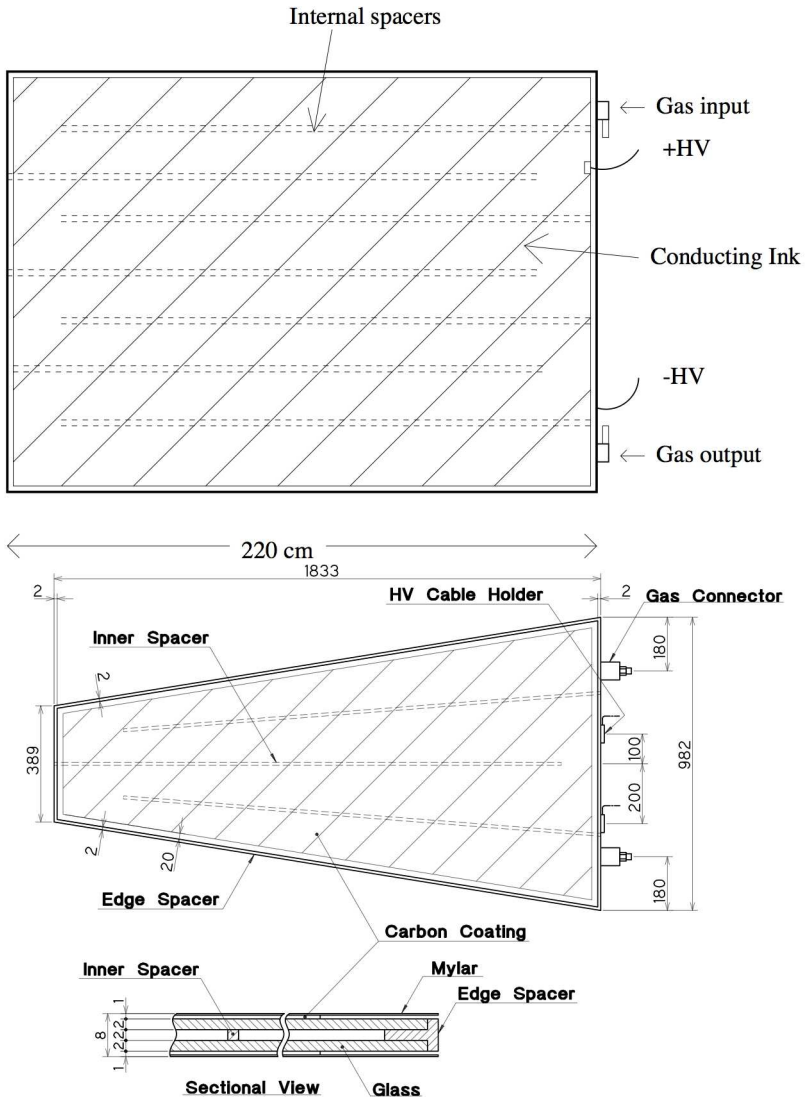

Figure 2.27: The barrel and end-cap RPC.

farm and a level 4 trigger, which runs in the off-line Belle computing system and performs more elaborate background reduction based on full event reconstruction.

The Level-1 (L1) trigger

An overview of the level-1 trigger system is shown in Fig. 2.29. It consists of the sub-trigger system and the central trigger system called global decision logic (GDL) [25]. By design, all the subtrigger signals arrive at the GDL within 1.85μs after the event occurs. The L1 final trigger signal is issued 2.2μsafter the event crossing. The timing of the trigger signals must be accurate since the trigger signal determines the readout timing. We determine the timing of the

final trigger by the TOF trigger or, in its absence, the ECL trigger.

Sub-triggers

The GDL receives up to 48 subtrigger signals. As shown in Fig. 2.29, there are trigger signals from the CDC, TOF, ECL, KLM and EFC systems. Their trigger systems will only be mentioned very superficially here; for more information, see Ref. [29]. The CDC provides two types of triggers: the $r-\phi$ trigger and the z trigger [27]. The $r-\phi$ trigger is based on the signals from six axial superlayers, while the z trigger is formed by signals from the cathode strips and z information inferred from the axial and stereo layers. The TOF produces trigger signals based on the hit multiplicity and back-to-back topology. The ECL trigger is based on trigger cells (TC) formed of 4×4 crystals combinations. It also provides triggers based on the $\theta - \phi$ segmentation, where the number of isolated cluster is calculated from the TC hit patterns. The KLM detects muons using four (two) layers in the barrel (endcap) parts and sends trigger signals to the GDL. The EFC provides two types of triggers: the EFC Bhabha trigger is based on the forward and backward coincidence, while the two photon trigger is based on a single hit. Another important subtrigger is the random trigger, which is useful to understand the background noise hits in the detector elements.

Global Decision Logic (GDL)

The GDL receives up to 48 subtrigger signals and aligns their timing by adding an appropriate delay to each channel. It then performs trigger logic operations to the subtrigger signals and generates 48 types of triggers. (Since exp. 21, the number of trigger types is increased to 64.) The GDL issues the final trigger 2.2 μs after the event's e^+e^- collision. For the hadronic trigger, the GDL has four main triggers:

- ♢ Two-track trigger: This requires the following information from the CDC: two tracks with $r-\phi$ and at least one track with z triggers and an open angle of at least 135°. This trigger also requires TOF hits and ECL clusters.

- ♢ Three-track triggers: This is similar to the two-track trigger, but with CDC $r-\phi$ information required for three or more tracks. Several different types of triggers are formed depending on the number of tracks, opening angle, TOF hits and ECL cluster hits.

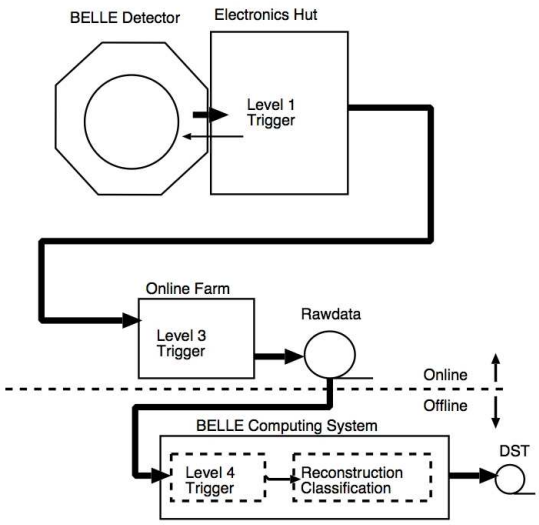

Figure 2.28: An overview of the Belle trigger system.

♢ Isolated cluster counting trigger: This requires four or more isolated ECL clusters, which avoids Bhabha events.

♢ Total energy trigger: This requires that the analogue sum of energy deposited in the ECL be greater than 1 GeV. It is vetoed by the ECL Bhabha and cosmic triggers.

♢ Combined trigger: This is a combination of track trigger, energy and cluster trigger.

Each trigger provides 90% to 97% efficiency for $B\bar{B}$ events [28]. Because the track, energy and cluster triggers are almost independent, we expect more than 99% efficiency for $B\bar{B}$ events when using the overlap of these triggers. The trigger rate is correlated to the beam currents and the luminosity, but also depends on the beam background condition. In spite of the reduction of beam background and the modification of the trigger logic, the trigger rate gradually increases as the beam currents and the luminosity increases.

Level-3 (L3) and Level-4 (L4) Triggers

The aim of the level-3 trigger is to reduce the number of events to be stored. The L3 trigger first checks the L1 trigger information but passes some categories of events, such as Bhabha events and random trigger events. If an event does not belong to these categories, the L3 trigger performs a fast reconstruction and discards the event if it has no track with $|z| < 5$ cm at the IP. A large

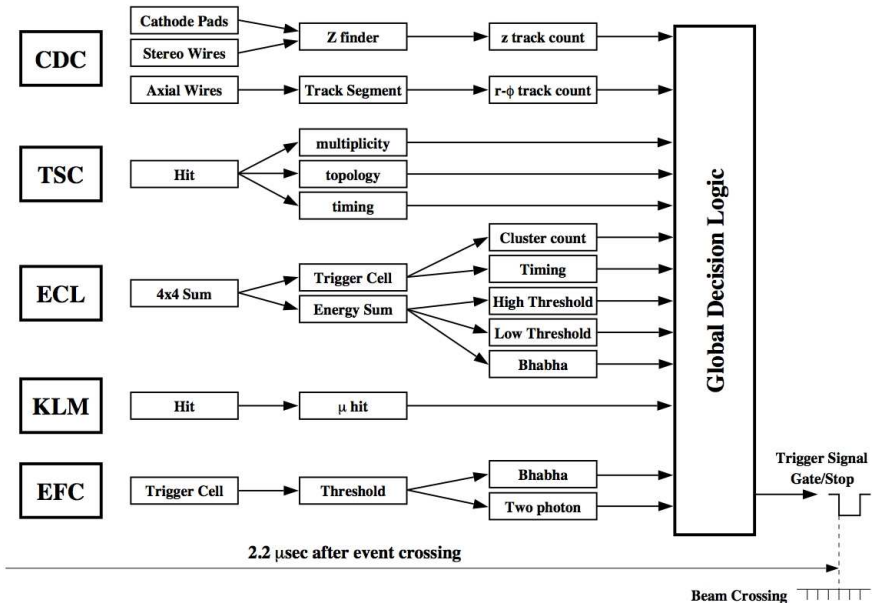

Figure 2.29: Belle level one (L1) trigger.

part of the beam background events are discarded by this procedure. The L3 software has been activated since Experiment 11 and results in a factor of two reduction of stored events while retaining an efficiency of more than 99% for hadronic and τ-pair events. The level-4 trigger filters events just before the full event reconstruction takes place [30]. The basic strategy of this trigger is to use a fast tracker to reconstruct tracks in order to reject tracks originating away from the IP. Events rejected by the L4 trigger still remain in the raw data. Thus the L3 trigger (and the L1 trigger) reduce the data size to be recorded, while the L4 trigger reduces only the CPU time for DST production. The L4 trigger rejects about 78% of triggered events while keeping nearly 100% of B meson events.

Data Acquisition (DAQ)

The role of the DAQ system is to record events specified by the trigger up to its limit of 500 Hz, while keeping a dead-time fraction of the detector of less than 10%. To achieve this, a distributed-parallel system is used. The overview of the Belle data acquisition system [26] is shown in Fig. 2.30. The DAQ system is segmented into 7 subsystems to handle the data from each subdetector. The signals from most subdetectors go through a charge-to-time (Q-to-T) converter and are processed by a time-to-digital converter (TDC). The Q-to-T converter produces a pulse whose width is proportional to the input charge; the multihit TDC "digitize" the timings of the leading and trailing edges of

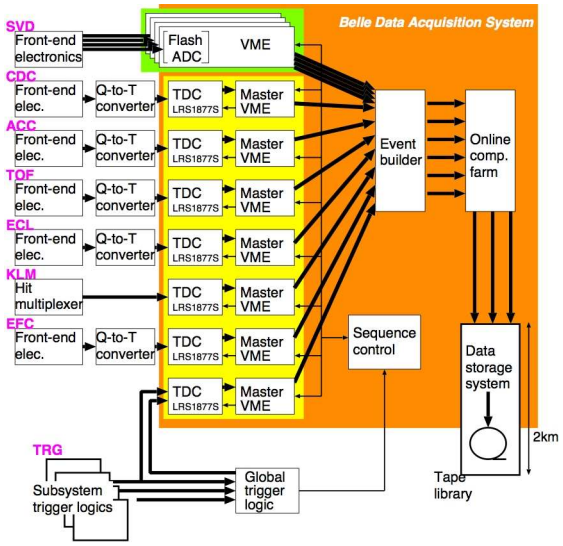

Figure 2.30: Belle data acquisition system.

this pulse. Only the SVD uses flash analogue-to-digital converters (FADCs) instead of TDCs. The KLM does not have a Q-to-T converter, since the pulse height does not provide useful information. The readout sequence starts when the sequence controller (SEQ), upon receiving a final trigger by the GDL, distributes a common stop signal to the TDCs. The data from each subdetector is combined into a single event by the event-builder, which converts "detector-by-detector" parallel data streams into "event-by-event" data. The output data of the event-builder is transfered through the level-3 trigger to the online computer farm. The quality of the data is monitored by the online data quality monitor (DQM) in the online farm. Finally, the data is sent via optical fiber to the mass storage system at the KEK computing center, where it is stored on tape. The typical size of a hadronic event is about 30 kB, which corresponds to a maximum data transfer rate of 15 MB/s for a trigger rate of 500 Hz.

Data Processing

The events accepted by the L4 trigger are reconstructed and the information is stored on data summary tapes (DST). In this stage, raw data, which are direct logs of the data acquisition devices, are converted into physics objects of momentum 3-vector, closest approach to the IP and associated particle identification information. A basic summary of the reconstruction procedure is as follows. Charge tracks are reconstructed using signals from the CDC. They are extrapolated inwards to the SVD and outwards to the ACC, TOF, ECL and KLM, where we look for associated signals. Hits in the ECL and KLM that

Table 2.6: Examples of event classification.

Category	Description
HadronB	general hadronic events
HadronC	tight general hadronic events (< 5 tracks)
Bhabha	Bhabha ($e^+e^- \to e^+e^-$) events
RadBhabha	radiative Bhabha ($e^+e^- \to e^+e^-\gamma$) events
GammaPair	$e^+e^- \to \gamma\gamma$ events
MuPair	$e^+e^- \to \mu^+\mu^-$ events
TauPair	$e^+e^- \to \tau^+\tau^-$ events
LowMulti	two photon events and others
Random	random triggered events

have no associated track in the CDC will be deemed neutral particles (photons or K_L mesons). Four-vectors can then be assigned to the charged tracks and neutral particles and PID likelihoods are determined. Various other flags and variables are calculated and all the information is written to the DSTs. Events are then classified into several categories based on certain selection criteria and stored as skimmed data accordingly. Table 2.6 lists examples of the event classification. Most analyses, including this one, start from the HadronB sample.

2.8 SOFTWARE

A COLOSSAL AMOUNT of software has been written and developed by the members of the Belle collaboration. In addition to software for DAQ operation and data processing described above, software has also been written for analysis of data and simulation of the detector and physical processes. This is formally known as the Belle AnalysiS Framework (BASF). It consists of a main kernel, user interface and modules that can be dynamically loaded at run time. A typical user analysis can be written as a dynamically loaded module without having to worry about the interface with external software. BASF is also used for Monte Carlo (MC) generation, as described below.

Monte Carlo Generation

AN IMPORTANT part of high energy physics data analysis is comparing the distributions of real data to expectations. Because of complexity of the detector response and various physics processes that may mimic the signal being studied, this comparison cannot be made using analytically derived distri-

butions. Instead, the physics process and detector response are modelled using a Monte Carlo (MC) simulation. The real data distributions are then compared to the corresponding MC distributions that contains considerably more events (to reduce the statistical fluctuation of the simulated vs real data). This simulation is aware of the detailed geometry, response, and deficiencies of the entire Belle detector. It is used to study detector response of very rare types of events, enabling us to deduce ways to increase the sensitivity for such events. Producing MC data takes place in two stages. First, the underlying particle physics processes, from e^+e^- collision to the subsequent decays of very short-lived daughters, are generated. Then, the detector response to these particles is simulated. The first step uses the so called QQ generator [33] developed by the CLEO collaboration to study B meson decays created by the $\Upsilon(4S)$ resonance. It incorporates particle properties and event production rates compiled from many experiments in the form of world averages and also relevant information about the KEKB accelerator, such as electron and positron energies. For newer analyses, the modern EvtGen [34] package is used to generate the particle physics processes. It is thought to describe the angular distributions of particles more accurately. Background continuum events are generated using the JETSET program [31] in which the subsequent hadronisation processes are based on the Lund string fragmentation model [32]. About three times the luminosity recorded in data is generated for the continuum events. The generated events, whether from QQ or EvtGen or JETSET, are then passed to a BASF module called GSIM. This module simulates the detector response; it is based on the CERN package GEANT3 [35] and simulates the interactions between the final state daughters and the detector response. The simulated data is then reconstructed in the same way as real data, with the final MDSTs containing the additional event generator information. Much effort is made to make the simulation as accurate as possible. Background hits are added by taking random trigger events and inserting their noise hits into the MC event. The varying size and position of the IP is incorporated as are evolutions in the subdetectors, such as appearance (or disappearance) of dead channels.

Chapter 3

The Measurement Techniques and Signal Monte Carlo

"I have tried to avoid long numerical computations, thereby following Riemann's postulate that proofs should be given through ideas and not voluminous computations"

David Hilbert

in this chapter....The unique techniques employed in the measurement are described. In addition the analysis performed in signal monte carlo is described here.

3.1 RECONSTRUCTION TECHNIQUES

A thorough description of the major reconstruction techniques in this measurement analysis are given. We start with the reconstruction techniques for the final state particles that are central to the analysis.

K_L^0 RECONSTRUCTION TECHNIQUE

A key point in the analysis of final states containing K_L^0 is the reconstruction of its momentum. The technique presented below makes use of the KLM[1] subsystem of the Belle detector [5], which consists of several layers of iron absorber interspaced with resistive plate chambers.

This system enables one to reconstruct muon tracks as well as hadronic showers. Showers which do not have a matching charged track are assumed to be produced by the K_L^0, with the position of the shower giving information about the flight direction of the K_L^0, depicted in figure 3.1. The direction resolution is improved if the K_L^0 deposits energy in the electromagnetic calorimeter in front of the KLM[a], in which case the position of the calorimeter cluster is used to determine the K_L^0 flight direction, depicted in figure 3.2.The later are called as ecl type K_L^0 and the rest of the K_L^0 are called klm type K_L^0.

[a] the belle electromagnetic calorimeter is called ecl

To extract the magnitude of the K_L^0 momentum one needs to employ additional constraints. In particular to reconstruct D^0's decay into $K_L^0 X$ where X is a fully reconstructed system,[2] one can apply a D^0 mass constraint[3] and solve the resulting 4-momentum equation with respect to the magnitude of the K_L^0 momentum, $|\vec{p}_{K_L^0}|$ and exploit the D^* tag[4] to reconstruct the signal[5].

[1] KL from $[K_L^0]$ and M from $[\mu]$, the K_L and μ identification subdetector at belle

[2] that is, $D^0 \to K_L^0 X$, where X is fully reconstructed, i.e. its 4-momentum is known from the detector at Belle

[3] assume that the decay products originated from D^0 so their combination has the known value of mass of D^0, colloquially known as D^0 mass hypothesis.

[4] $D^* \to D^0 \pi$ decay, π is a slow or soft pion, i.e. a low energy or low momentum pion, π_{slow}, because of the close proximity the starred and neutral D mesons in the mass spectrum of the mesons. [in otherwords most of the energy of the D^* is taken up by the D^0 for its mass alone.

[5] We define all our signal by the distribution of the D^* mass or its mass difference wrt the D^0 mass

Figure 3.1: This diagram exemplifies the identification of K_L^0 in the Belle Detector.

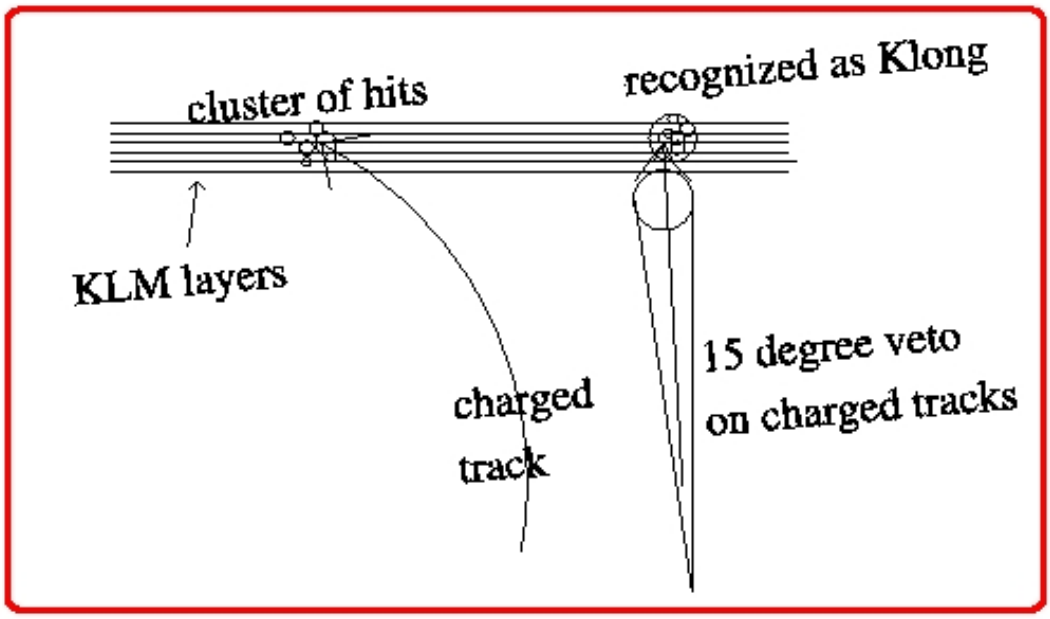

Figure 3.2: The K_L^0 that has interacted in the ECL in addition to its recognition in the KLM detector has better direction resolution. This is known as ecl type K_L^0.

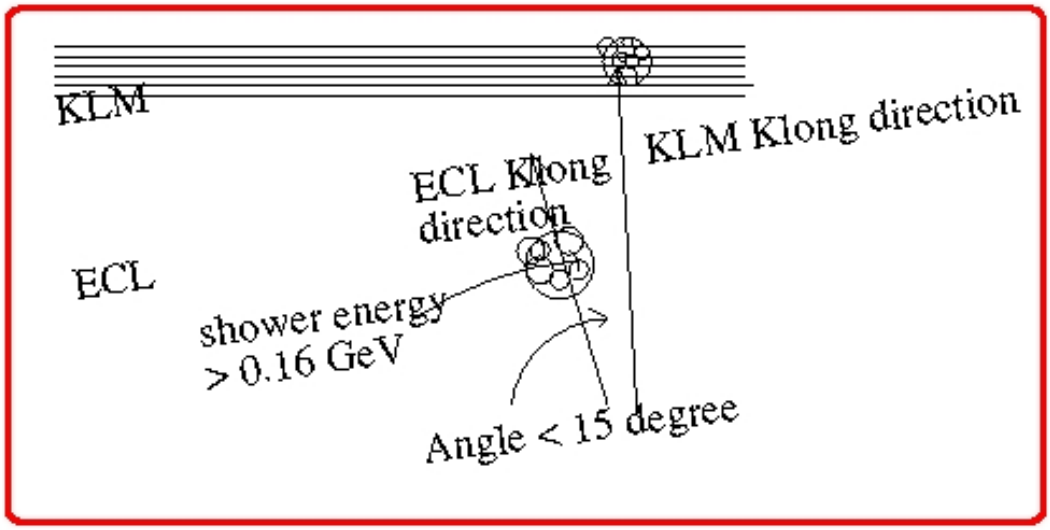

If P is the projection of the 3-momentum of X[6] along the K_L^0 direction, e is the energy of X, p is the 3-momentum magnitude of X, M is the D mass and m is the K_L^0 mass then coefficients of the quadratic equation for the solution of K_L^0 3-momentum magnitude are a, b and c; given by:

$$\begin{aligned} \text{a} &= 4(P - e^2) \\ \text{b} &= 4(M - m^2 - e^2 + p^2)P \\ \text{c} &= (M^2 - m^2 - e^2 + p^2) - 4e^2m^2 \end{aligned}$$

[6] π^0 or $\pi^+\pi^-$

Two body decay and a toy monte carlo scheme

In a two body decay, a particle characterized by 3-momentum $\vec{P}$ and mass M, decays into a particle characterized by $\vec{P}_1$, m_1 and another by $\vec{P}_2$, m_2. We have an experimental situation where one of these daughter particles[a] is fully reconstructed, the other particle's energy or momentum is "missing" in the detector. In addition the detector supplies the direction $\hat{P}_1$ of the particle whose energy is missing from the detector.

[a] say $\vec{P}_2$, m_2

Consider the case of the decay[1] $D^0 \rightarrow K^0_L \pi^0$. In the D^0 rest frame this decay is produced symmetrically in all direction. So the K^0_L flux is spherically symmetrical which means to produce equal amount of flux at two different places on the sphere one needs to distribute the flux in an equal range of polar angle ϕ but not θ.

θ and ϕ are "simulated" i.e. these are considered two independent parameters and a set of two numbers are generated randomly to mimic the direction of the K^0_L over the sphere. The scheme of simulating the K^0_L's direction, employing the principles of two body decay and reconstructing $\vec{P}$ of D^0 by assuming its mass M, described in figur3.3 constitutes the prototype of a monte carlo program known as toy monte carlo.

In this simple yet effective scheme, 2400 events[2] were generated. Now we know the direction of the K^0_L for each of these events, i.e. $\hat{P}_1$. $\vec{P}_2$, m_2 are known[3]. Again since $(\vec{P}_1, m_1)$ and $(\vec{P}_2, m_2)$ form the two body decay hypothesis of $(\vec{P}, M)$,

[1] this is one of the important decay mode in our analysis

[2] Usually monte carlo events are generated in multiples of the size of any experimental data sample, 2400 events are sufficient for this study

[3] π^0- is fully reconstructed

employing the relativistic energy momentum equation and the 4-momentum additions we have to solve for P_1, the magnitude of K_L momentum.

This results in a Quadratic Equation in P_1 which can be solved if M and ${m_1}^4$ are given. Once we have P_1, we can add $(\vec{P}_1, m_1)$ and $(\vec{P}_2, m_2)$ to form $(\vec{P}, M)$. We will thus know $(\vec{P}, M)$ without a distribution for D^0 mass M. Thats why we call this a "D^0 mass constraint method" or "D^0 mass method". This scheme is also applicable to a three body decay like $D^0 \rightarrow (K_L^0\pi)\pi$, where the $\pi\pi$ system has complete information from the detector.

This toy monte carlo doesn't have a real Belle data-event but is studied to see that the method works. In a real data or monte carlo sample the "D^0 mass method" is used throughout in this analysis to retrieve the missing energy of the K_L^0.

Since the equation for the magnitude of the K_L^0 momentum is quadratic there may be up to two solutions. We have chosen the solution $[-b - \sqrt{(D)}]/2a$ and call this the first solution and the other solution turns out to be non-physical. Algorithm 1 shows a piece of code written for this purpose.

To test the validity of this approach first-hand an algorithm was developed which generated 2400 events by simulating "the unknown direction" of a K_L like toy-particle[5] in the two body decay via random numbers and reconstructed the 4-vectors of the toy-particles by employing a mass constraint on the D^0.

A comparison of the generated and the reconstructed momentum distribution is shown in figure3.4. The second solution isn't useful as can be seen in the figure 3.5. This shows that our method of K_L reconstruction is a promising technique for a K_L like particle.

[4]known value of invariant mass of D^0 is 1.8645 GeV and K_L^0 is 0.497 GeV
[5]the direction is known in the detector

Algorithm 1: Algorithm for toy mc

```
float toymc::quadratic (float Y, float Z, float X_enery, float
K_long_mass)
{
float a = 4*((Y*Y) - (X_enery *X_enery));
float b = 4*Z*Y;
float c = Z*Z - 4*(X_enery *X_enery)*(K_long_mass
*K_long_mass));
//solutions of the quadratic equation
float Pk1 = (-(b) - (sqrt(b*b - 4*a*c)))/(2*a);
float Pk2 = (-(b) + (sqrt(b*b - 4*a*c)))/(2*a);
cout << Pk1 << '\t' << '\t' << Pk2 << '\t';
Hist[2]->accumulate(Pk1,1.0);
Hist[3]->accumulate(Pk2,1.0);
toymc->column("momsol1",Pk1);
toymc->column("momsol2",Pk2);
}
```

Figure 3.3: A "Toy" monte carlo scheme for a two body decay. The scheme of simulating the K_L^0's direction by random numberss, employing the principles of two body decay $\vec{P},M \rightarrow \vec{P}_1,m_1 + \vec{P}_2,m_2$ to $D^0 \rightarrow K_L^0 X$ and reconstructing momentum $\vec{P}$ of D^0 by assuming its mass M constitutes the prototype of a monte carlo program known as toy monte carlo. The physics of two body decay is described by 8 variables $[\vec{P}_1,m_1 \cong 4;\ P_2,m_2 \cong 4]$ and 6 equations thereby posing two unknowns. On the generation side of the toy monte carlo these two unknowns can be assigned to the direction of a K_L [two variables θ and ϕ] as on the reconstruction side the direction is known from the detector.

In the rest frame of $D^0(\vec{P},M)$

$$E_1 = (M^2 - m_2^2 + m_1^2)/2M \tag{3.4}$$

$$|\vec{P}_1| = |\vec{P}_2| = (1/2M)[(M^2 - (m_1+m_2)^2)((M^2 - (m_1-m_2)^2)]^{1/2} \tag{3.5}$$

$$d\Gamma = (1/32^2)|M|^2(|P_1|/M^2)\, d\phi_1\, d(cos(\theta_1)) \tag{3.6}$$

The decay is spherically symmetric which means the flux is flat in ϕ_1 but not in θ_1 as seen above. The decay is flat in cosine of θ_1 instead. In the generation of the monte carlo (θ_1,ϕ_1), i.e, the direction of K_L is assumed unknown and simulated by two random numbers. Thus in the generation side there are 8 variables and all of them are known. On the reconstruction side these two variables are obtained from detector so constraining the D^0 mass [and the K_L mass] makes all the variables known. With 8 equations and 8 variables solving for the K_L momentum magnitude $|\vec{P_1}|$ gives 2 solutions from the resulting quadratic equation.

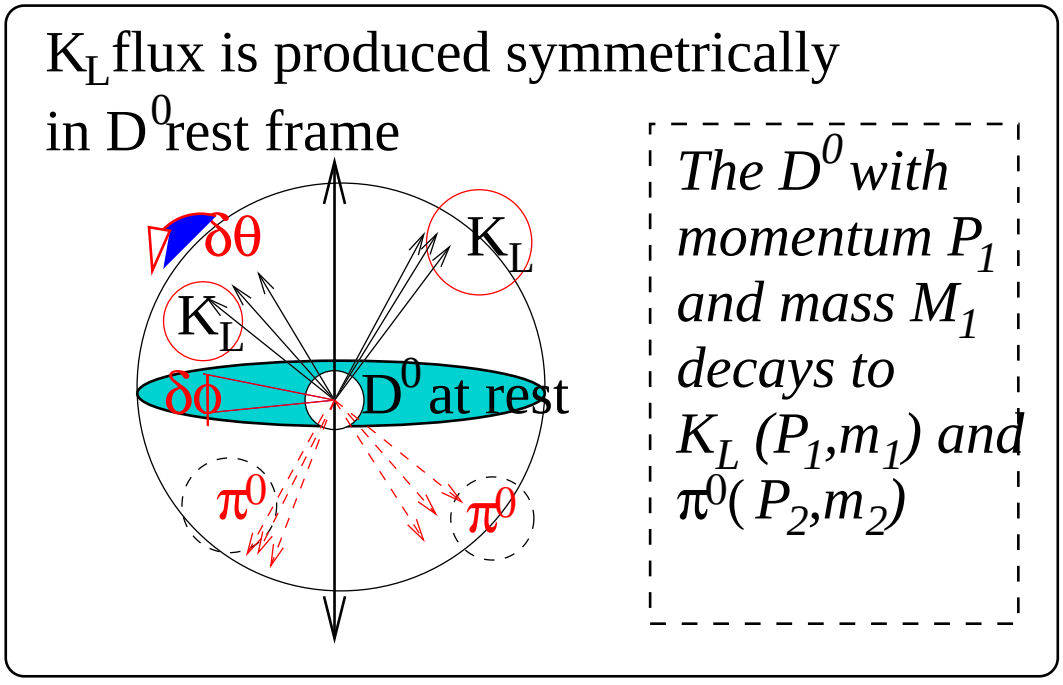

Figure 3.4: The generated and reconstructed momentum distribution for the "K_L^0 like" situation described in figure 3.3 is shown with 2400 randomly generated events.

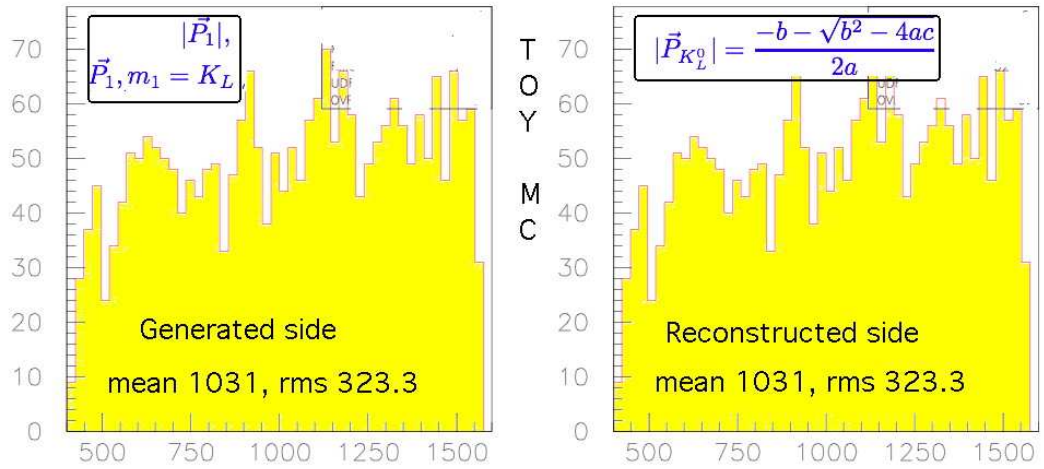

Figure 3.5: Non-Physical solution in Toy Monte Carlo The second solution in the "D^0 mass constraint method" is non-physical as evidenced in the results of the toy MC study.

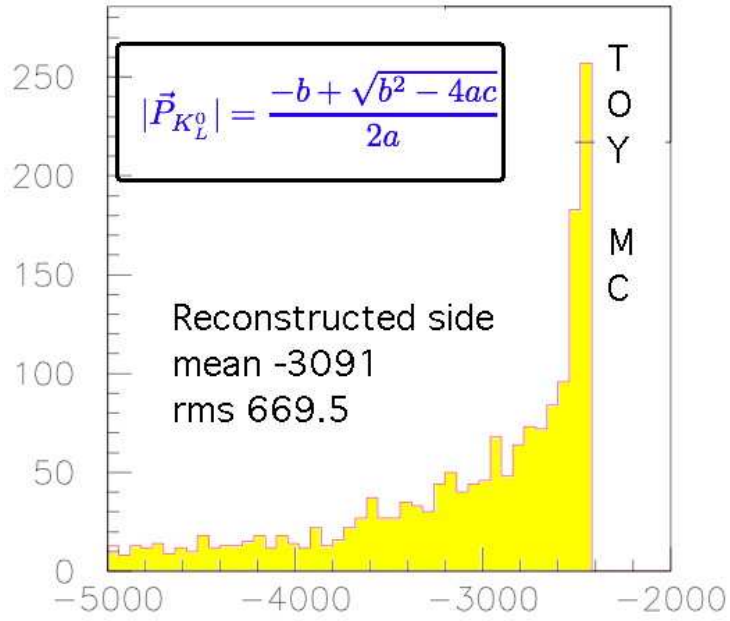

THE K_S^0 RECONSTRUCTION TECHNIQUE

The K_S^0 reconstruction at Belle is characterized by three parameters, "dr"[a], "dphi"[b] and "dz"[c] that can be defined from the K_S^0 vertex and the beam interaction point (IP). These parameters of K_S vertex are shown in endview in figure 3.6 and in sideview in figure 3.7. A clean sample of K_S can be obtained with $dr > 500\ \mu m$, $dz < 1$ cm, $\cos(d\phi) > 0.95$.

[a] dr is the $K_S \to \pi^+\pi^-$ vertex separation from the interaction point in the plane perpendicular to the beam axis

[b] cos(dϕ) is the cosine of the angle between the assumed K_S flight path from the interaction point to the decay vertex and the reconstructed K_S momentum in the transverse projection with respect to the beam.

[c] dz is the distance along the beam axis between the $\pi^\pm$ tracks at the K_S vertex

Figure 3.6: The K_S vertex, "dr" and "dϕ" are shown in the endview of the detector. The vertex measurement greatly enhances the K_S reconstruction quality.

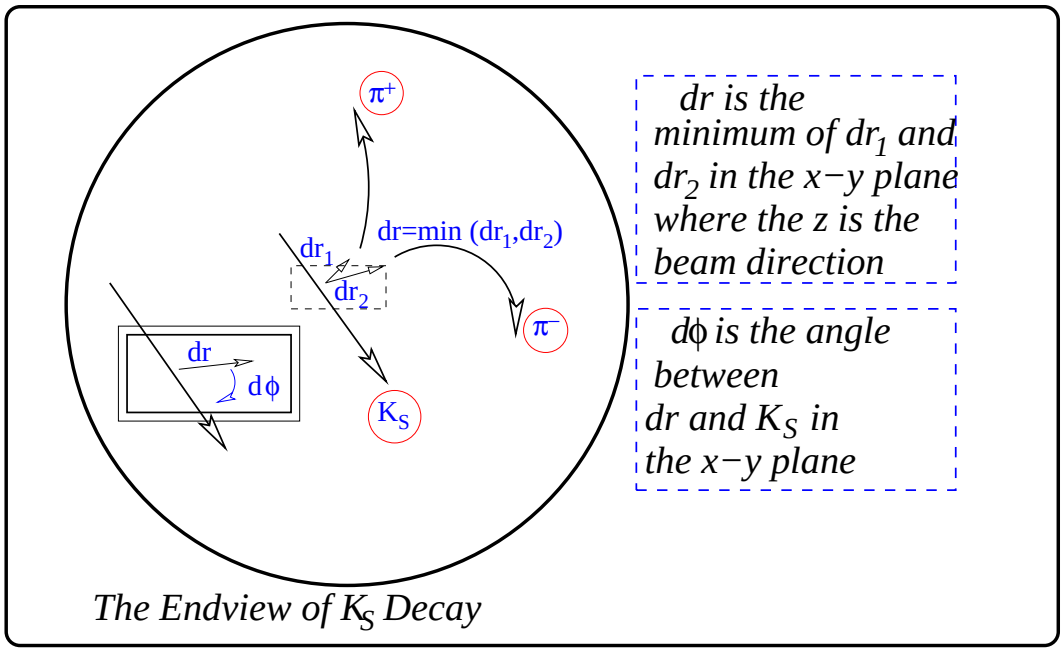

THE PSEUDO-K_L^0 ($\widetilde{K_L^0}$)

To monitor the performance of the "D^0 mass method" in retrieving the K_L^0 missing momenta we utilize the same D^0 decay modes but with K_S^0 instead of K_L^0 in the final state. In other words we use a K_S^0 sample of data and reconstruct them as if we are reconstructing a K_L^0. We use the K_S^0 flight direction reconstructed by its decay into $\pi^+\pi^-$[a] and apply the same procedure of reconstruction as for K_L^0: such K_S^0 are referred to as pseudo-K_L^0 or $\widetilde{K_L^0}$.

[a] smear its resolution to match that of the K_L^0

This works like a control mode and we have two such $\widetilde{K_L^0}$ modes, one for the signal K_S^0 mode and one for the calibration K_S^0 mode.[6] In addition since the pseudo K_L are inherently K_S, their resolution is narrower than that of K_L and this is taken care of by smearing the resolution of $\widetilde{K_L}$ to match that of the K_L. This is achieved by using the codes laid out in the algorithm 2. This smearing follows the relation between the old and new angles governed by the "resolu-

[6] see subsection 3.2 for definition of signal and calibration modes

Figure 3.7: The K_S vertex "dz" in the sideview.

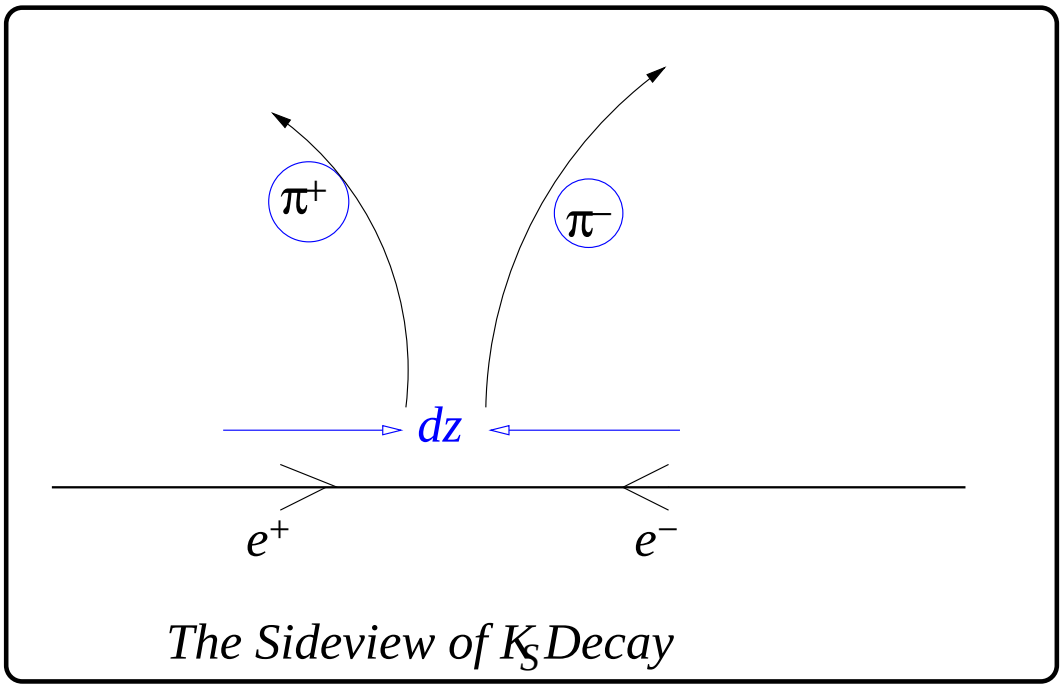

tions" of the angular distributions of K_S and K_L as given in the formula below:

$$\phi^{'} = \phi + R_1\sqrt{(\mathscr{R}^{\phi}_{K_L})^2 - (\mathscr{R}^{\phi}_{K_S})^2} \tag{3.7}$$

$$\theta^{'} = \theta + R_2\sqrt{(\mathscr{R}^{\theta}_{K_L})^2 - (\mathscr{R}^{\theta}_{K_S})^2} \tag{3.8}$$

Algorithm 2: Algorithm for smearing resolution of pseudo-K_L

```
int iDim = 2;
float rndm[2];
rnorml_(rndm,&iDim) ; // FORTRAN function
std:cout<<"random number 1 "<<rndm[0]<<endl ;
std:cout<<"random number 2 "<<rndm[1]<<endl ;
float newphi = PseudoKl.phi() + (sqrt((klphires)*(klphires) -
(ksphires)*(ksphires)))*rndm[0] ;
float newtheta = PseudoKl.theta() + (sqrt((klthetares)*(klthetares) -
(ksthetares)*(ksthetares)))*rndm[1] ;
```

3.2 STUDIES IN SIGNAL MONTE CARLO

SIGNAL SHAPE STUDIES

DEFINITION OF SIGNAL

There are basically 4 decay modes for signal we are interested in, in this measurement, see table 3.1. These decay modes and their charge conjugate (cc) modes are combined together for these studies. Where cc modes are not included notes are provided to mention this.[a] In the course of analysis it can be seen that the cc modes essentially have the same properties[b] as that of the defined modes, as this is not a CP violation study.

[a] This does not alter the analysis in any significant way
[b] such as signal shape, branching ratio etc

The first two modes are the decays of the D^0 where we intend to measure the asymmetry of the K_S and the K_L and the second two modes are the decays of D^0 where there is no such natural asymmtery, as K_S and the K_L are supposed to be produced at equal rates. These later modes are chosen as a calibration to study and cancel any bias coming from reconstruction. At times we may use the synonym "signal modes" for the first two decay modes and "calibration or refernce modes" for the second two decay modes. These decays are explicitly mentioned in table 3.1. As a shorthand we can write out these decays as:

Definition of signal and reference/calibration modes tagged by $D^{*\pm} \to D^0\pi^\pm$, $\pi^\pm = \pi_{slow/soft}$ K_L does not decay inside detector		
sig, mode 1	$D^0 \to \bar{K}^0\pi^0$:	$D^0 \to K^0_S \underbrace{\to \pi^+\pi^-}$ $\pi^0 \underbrace{\to \gamma\gamma}$
sig, mode 2	$D^0 \to \bar{K}^0\pi^0$:	$D^0 \to K^0_L\, \pi^0 \underbrace{\to \gamma\gamma}$
ref, mode 3	$D^0 \to \underbrace{K^{*-}}\pi^+$:	$D^0 \to K^{*-}\{\underbrace{K^0_S \to \pi^+\pi^-}\ \pi^-\}\pi^+$
ref, mode 4	$D^0 \to (K^{*-})\pi^+$:	$D^0 \to (K^0_L\pi^-)\pi^+$

10,000 events were generated and simulated by the Geant Detector Simulation,[7] a module was written in C++ programming language that filtered out events without a "D^*+" in it and the "qq98" decay module was used to gener-

[7] the JETSET 7.3, Model 11 was chosen which takes care of the charm fragmentation.

ate signals for the signal and calibration modes.[8] These conditions have been summarized in table 3.1.

The K_L does not decay inside the Belle detector because of its longer life time. The K_S decays inside the detctor and therefore has a well measured vertex which gives rise to a clean signal for decay modes involving the K_S. On the otherhand the K_L suffers from poor identification and could be contaminated by large amount of background events.

Decay modes involving the K_L demands a lot of ingenuity in their reconstruction. This goal can be achieved although by tedious data analyses despite of the novel method of reconstruction strategy which involves powerful event selction criteria and careful algorithm development. This has resulted in a good signal quality for the analysis.

[8] The charge conjugate modes were not combined with these decay modes.

# OF EVENTS	GENERATOR	MODULES	PROCESS	VETO
10000	QQ98	JETSET7.3, MODEL 11	CHARM FRAGMENTATION	AT-LEAST 1 D^{*+}
mode 1	$D^{*+} \to D^0\pi^+$	$D^0 \to K^0_S\pi^0$	$K^0_S \to \pi^+\pi^-$	$\pi^0 \to \gamma\gamma$
mode 2	$D^{*+} \to D^0\pi^+$	$D^0 \to K^0_L\pi^0$	K^0_L	$\pi^0 \to \gamma\gamma$
mode 3	$D^{*+} \to D^0\pi^+$	$D^0 \to (K^0_S\pi^-)_{K^{*-}}\pi^+$	$K^0_S \to \pi^+\pi^-$	$\pi^0 \to \gamma\gamma$
mode 4	$D^{*+} \to D^0\pi^+$	$D^0 \to (K^0_L\pi^-)_{K^{*-}}\pi^+$	K^0_L	$\pi^0 \to \gamma\gamma$

Table 3.1: One example of how the decays were generated in the qq98 decay module is shown in the appendix (A.1).

PRELIMINARY RECONSTRUCTION OF SIGNAL

With the event selection criteria tabularaized in table 3.2, 10000 signal monte carlo events were generated and the calibration modes[9] were analyzed. Description of the results are given in figures 3.8, 3.9, 3.10 and 3.11. More details of the analysis of the calibration

Figure 3.8: 10000 signal monte carlo events of $D^0 \to (K_S\pi^-)_{K^{*-}}\pi^+$ were analyzed with a event selection criteria summarized in table 3.2, using a reconstruction algorithm developed for this purpose. The signal distribution is shown in D^{*+} mass, on top and deltaM (δM): the mass difference of D^{*+} and D^0, on bottom. Note that the resolution on the reconstructed D^{*+} mass is much wider than that on the δM which really corresponds to the mass of the slow pion, the pions produced from D^{*+} in its decay to D^0 and π^+. The slow pions are clearly distinguished from the random pions which helps in reducing the random pion backgrounds. The events have been vetoed to show only those reconstructed events which matched the events at the generated level. This is referred to as the monte carlo truth. The matching patterns for successful and failed events are shown in figure3.9.

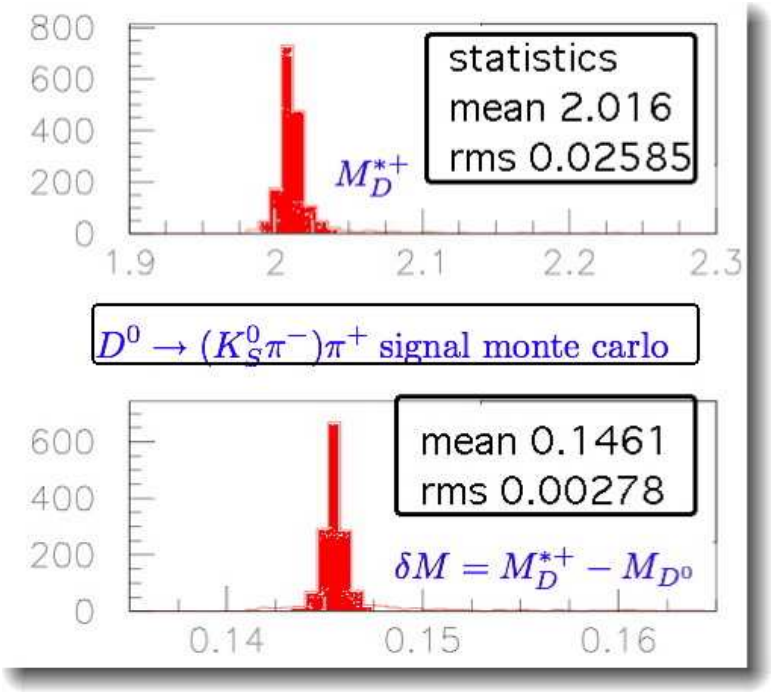

mode $D^0 \to (K_S\pi)\pi$ are shown in figures 3.12, 3.13, 3.14, 3.15 and 3.16. The statistics of the fitting have been shown in tables 3.3, 3.4, 3.5,3.6 and 3.7.

[9] mode 3 and mode 4, the corresponding charge conjugate modes are not included.

Figure 3.9: The events at the generated level and the reconstructed level were matched. The monte carlo truth results are shown for the candidate final state particles for each sequence of the decay $D^0 \to (K_S\pi)\pi$ and its tag $D^* \to D^0\pi$. "1" represents the case of a successful match. "0" represents the failed match in a situation when matching is valid to the daughter level, "-1" represents a successful matching to the daughter's daughter level and so on.

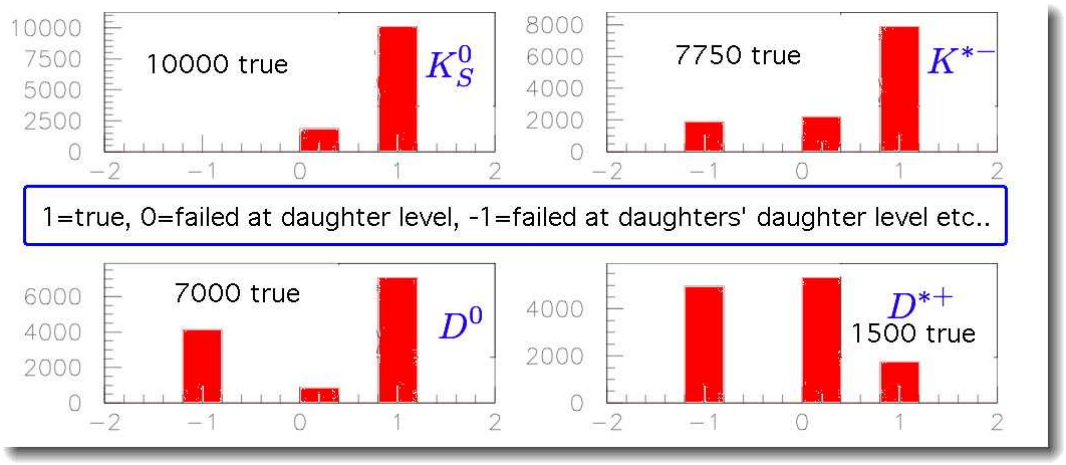

Figure 3.10: In the $D^0 \to (K^0_L\pi)\pi$ mode the K^0_L and D^0 masses are assigned their known values to retrieve the K^0_L missing energy. Note that the D^0 mass shows an erroneous value [true value is 1.865 GeV] because of an inefficient piece of code which was fixed and the correct value was recovered for further analysis. [known values were being passed in the algorithm using global options instead of passing by reference which caused this, this way 500 events were lost which were recovered by using the passing by reference method] This plot shows the K^{*-} mass in $D^0 \to (K^0_L\pi)\pi$ signal monte carlo which is quite broad. Note that there is a selection cut on K^{*-}, a fact that can be seen by the sharp fall on both sides of the histogram. The reconstructed D^{*+} mass is fitted to a gaussian distribution after vetoeing the events without a corresponding match at the generator level [aka mc truth]. The statistics are shown on top of each plot.

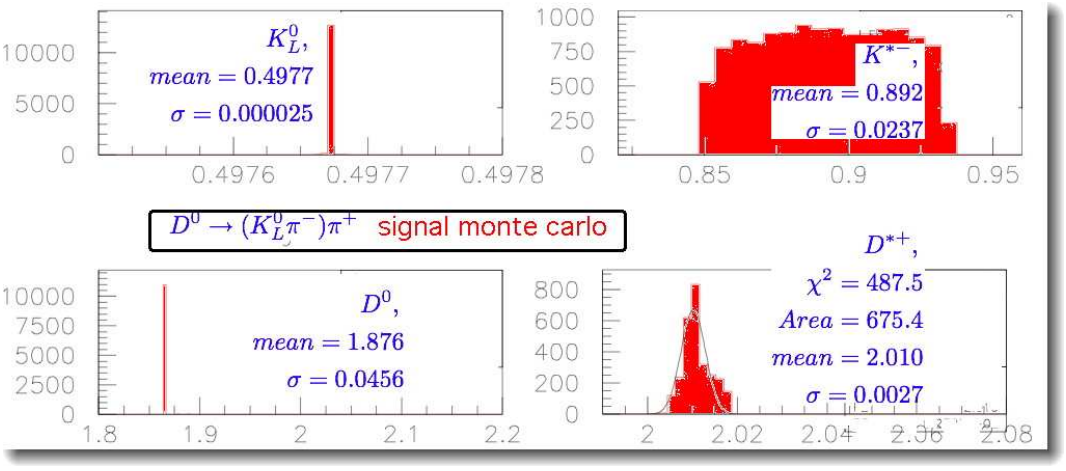

Figure 3.11: The K_L momentum from signal monte carlo. The first and second solutions for the K_L^0 momentum in $D^0 \to (K_L^0\pi)\pi$ are shown here. The second solution for the missing energy/momentum of K_L^0 turns out to be non-physical as expected [study in toy monte carlo in preciding sections]. This result was obtained using 10000 belle detector events [monte carlo] with full detector simulation as opposed to the 2400 events in the toy monte carlo.

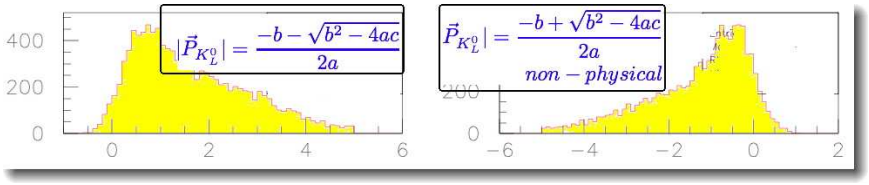

Figure 3.12: The K_S^0 invariant mass is fitted by a combination of two polynomials of order (1) and two gaussian functions. The fit quality is shown on the plot and the parameters of the fit functions are shown in table 3.3.

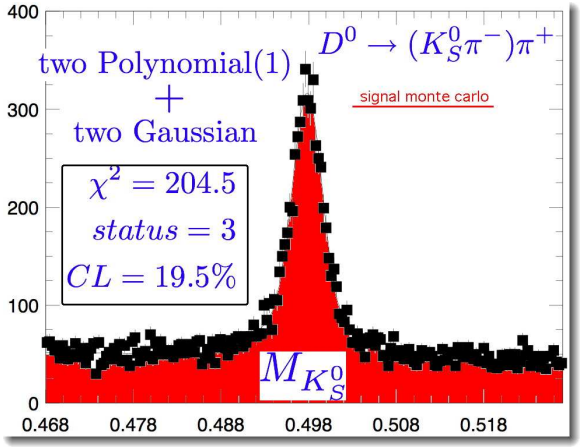

Figure 3.13: The K^{*-} invariant mass in $D^0 \to K_S\pi\pi$ mode is fitted to a signal gaussian fucntion and a background threshold function with its offset fixed to 0.640 GeV. The results of this fitting are shown in table 3.4.

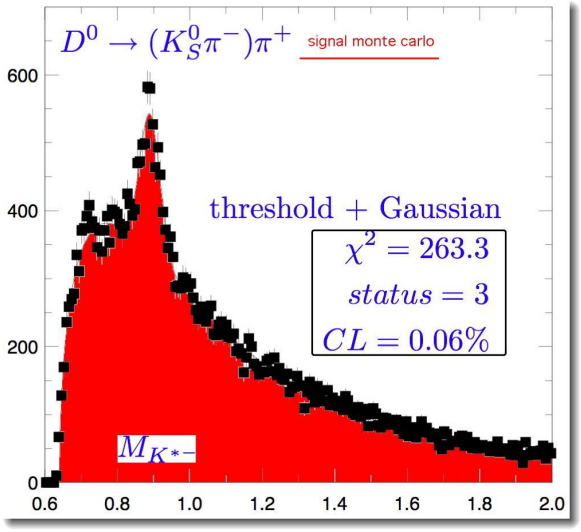

Figure 3.14: The D^0 invariant mass in $D^0 \to (K_S\pi)\pi$ mode is fitted to a gaussian function for signal and a second order polynomial function for background. Results are shown in table 3.5.

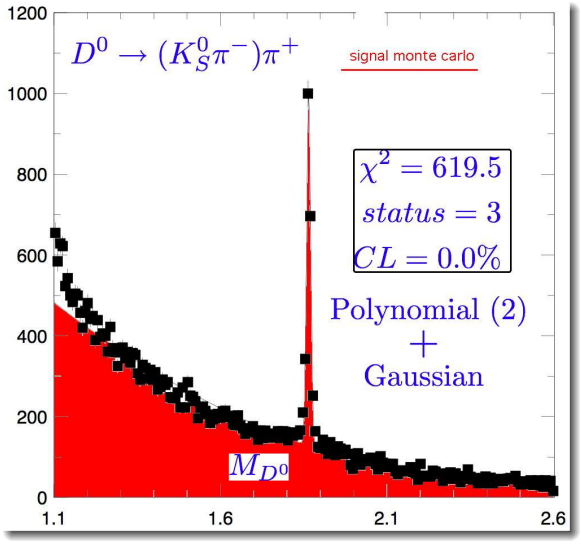

Figure 3.15: The D^{*+} invariant mass in $D^0 \to (K_S\pi)\pi$ mode is fitted to a signal gaussian function and a background threshold function with its offset fixed to 1.1 GeV. The results are shown in table 3.6.

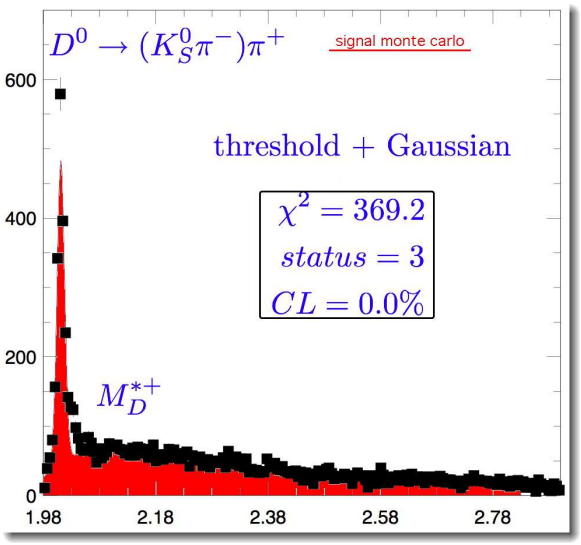

Figure 3.16: The reconstructed D^{*+} that has a matching generated D^{*+} decay. The events that do not satisfy the monte carlo truth conditions are vetoed and the signal events fitted to a Gaussian. See table 3.7.

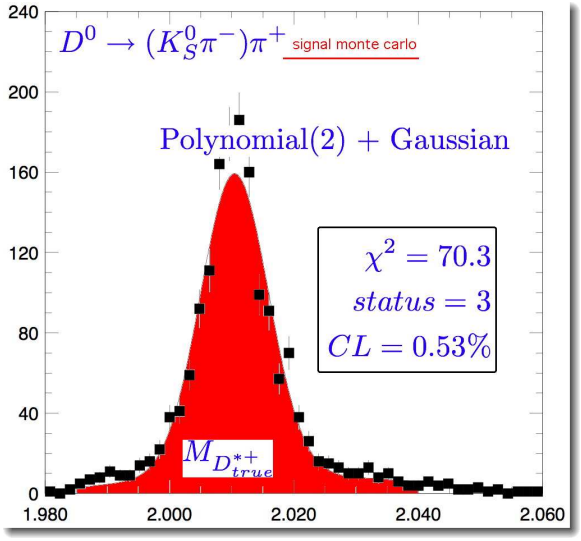

Table 3.2: The event selection criteria used for a preliminary study of the four decay modes in siganl monte carlo.

VARIABLE / PARAMETER	CUT VALUE / VALUE
K_S SELECTION	
dz	1.0 cm
dr	0.25 cm
$d\phi$	0.1 rad
$M^{lower}_{K_S}$ (- 10 MeV)	0.487672 GeV
$M^{upper}_{K_S}$ (+ 10 MeV)	0.507672 GeV
K^{*-} SELECTION	
$M^{lower}_{K^{*-}}$ (- 75 MeV)	0.81666 GeV
$M^{upper}_{K^{*-}}$ (+ 75 MeV)	0.96666 GeV
D^0 SELECTION	
$M^{lower}_{D^0}$ (- 30 MeV)	1.8345 GeV
$M^{upper}_{D^0}$ (+ 30 MeV)	1.8945 GeV
D^{*+} SELECTION	
$M^{lower}_{D^{*+}}$ (- 30 MeV)	1.980 GeV
$M^{upper}_{D^{*+}}$ (+ 30 MeV)	2.040 GeV

Table 3.3: The K^0_S mass signal has been fitted to two Gaussians (G1, G2) and their yield, mean and resolution are given with the corresponding errors in this table [See figure 3.12]. Note that the K_S mass is close to its correct value and the mass width is quite narrow. The parabolic error is symmetrical while the minos error has asymmetrical values.

			PARABOLIC$^{(\pm)}$	MINOS$^{(-)}$	MINOS$^{(+)}$
G1	Yield	1788.5	223.4	218.2	234.2
G2	Yield	3129.7	250.3	264.6	240.5
G1	$M_{K^{*-}}$	0.497	0.00029	0.00032	0.00028
G2	$M_{K^{*-}}$	0.4978	0.000052	0.000051	0.000052
G1	σ	0.0047	0.00057	0.00051	0.00062
G2	σ	0.0016	0.000082	0.000083	0.0000796

Table 3.4: The K^{*-} mass signal is fitted to a Gaussian and the yield, mean and resolution are given with their errors in this table [See figure 3.13]. The background shape is fitted to a threshold function with its offset fixed to 0.640 *GeV*. Note the mass of K^{*-} is consistent with its correct value and the mass width is wide and the errors are small. This width is higher than what we saw in figure 3.11 as there is no invariant mass cut placed on the K^{*-} mass before fitting [these are candidate K^{*-} here, fitted before any cut to get the full width].

		PARABOLIC$(\pm)$	MINOS(-)	MINOS(+)
Yield	2055.1	125.3	123.0	126.5
$M_{K^{*-}}$	0.89008	0.001528	0.001530	0.001528
σ	0.02795	0.00178	0.001723	0.001831

Table 3.5: The D^0 mass signal is fitted to a Gaussian and the yield, mean and resolution are given with the errors in this table [See figure 3.14]. The background shape is fitted to a polynomial function of order(2) with its offset fixed to 1.1 *GeV*. Note the mass of D^0 coincides with its correct value and the mass width is narrow and the errors are small.

		PARABOLIC$(\pm)$	MINOS(-)	MINOS(+)
Yield	1799.4	49.89	49.51	49.53
M_{D^0}	1.8648	0.00019	0.000187	0.000188
σ	0.00621	0.000198	0.000195	0.000199

Table 3.6: The D^{*+} mass signal is fitted to a Gaussian and the yield, mean and resolution are given with their errors in this table [See figure 3.15]. The background shape is fitted to a threshold function with its offset fixed to 1.956. Note the mass of D^{*+} coincides with its correct value and the mass width is narrow and the errors are small. The width is slightly higher than that of D^0.

		PARABOLIC(±)	MINOS(-)	MINOS(+)
Yield	1614.7	49.83	48.61	48.69
$M_{D^{*+}}$	2.011	0.00021	0.000213	0.000216
σ	0.00679	0.000259	0.000254	0.000264

Table 3.7: The trueD^{*+} mass signal is fitted to a Gaussian and the yield, mean and resolution are given with the errors in this table [See figure 3.16]. The background shape is fitted to a polynomial function of order 2 with all of its parameter set free. Note the mass of D^{*+} is consistent with its correct value and the mass width is narrow, narrower compared to the D^{*+} width without a monte carlo truth veto.

		PARABOLIC(±)	MINOS(-)	MINOS(+)
Yield	1295.3	38.84	41.56	41.71
$M_{D^{*+}}$	2.010	0.000172	0.000172	0.000173
σ	0.00548	0.000177	0.000191	0.000193

K_S^0 AND K_L^0 RESOLUTION

While the study is focussed in signal monte carlo part of the analysis it is worth while to see what the resolutions of the K_S^0 and K_L^0 angular distribution are. The resolution is supposed to be much better for the K_S^0 as compared to the K_L^0 while for the two types of K_L sample described earlier the resolution is supposed to be better for the ecl type. The results are shown in figures 3.17 and 3.18 and are summarized in table3.8.

Figure 3.17: The K_S^0 angular resolutions ["difference" in the generated and reconstructed angular distributions] are given in terms of its angles, θ and ϕ.

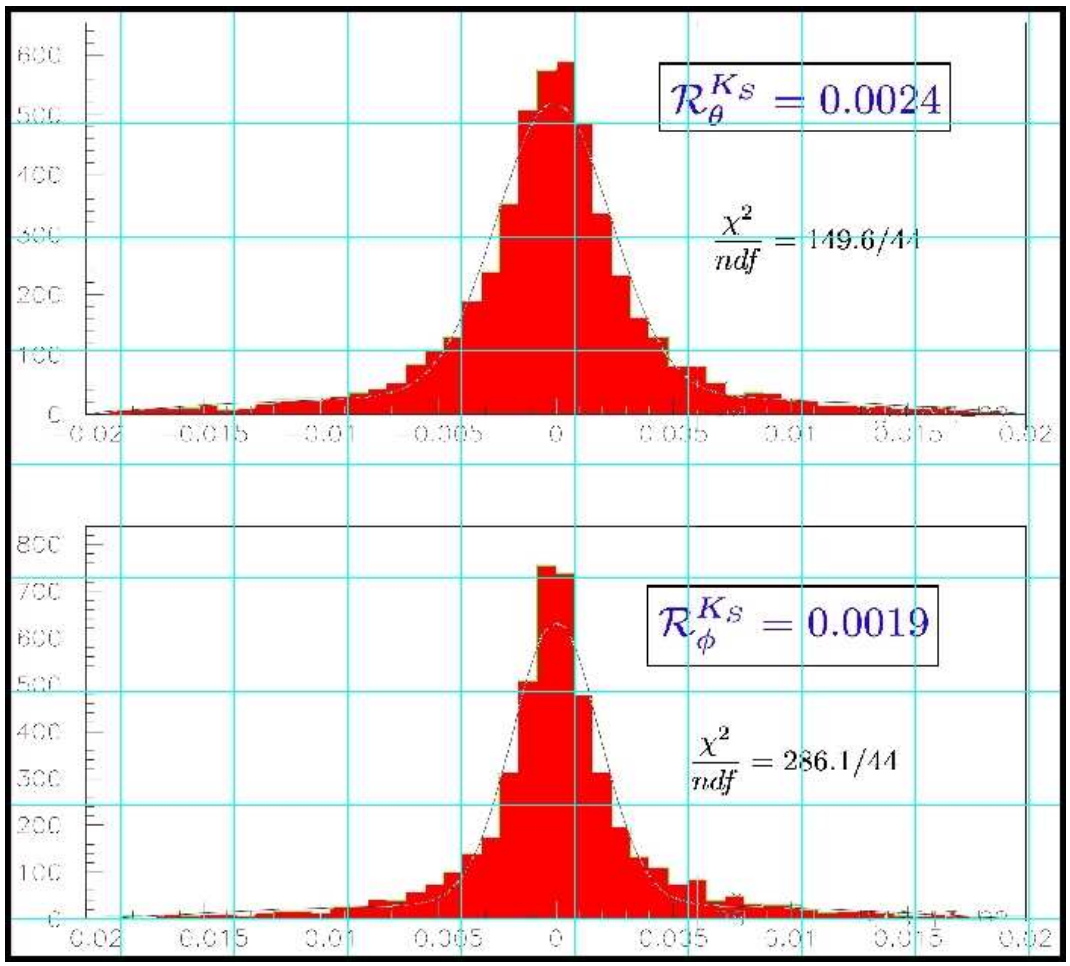

Figure 3.18: K_L^0 Resolution in θ and ϕ

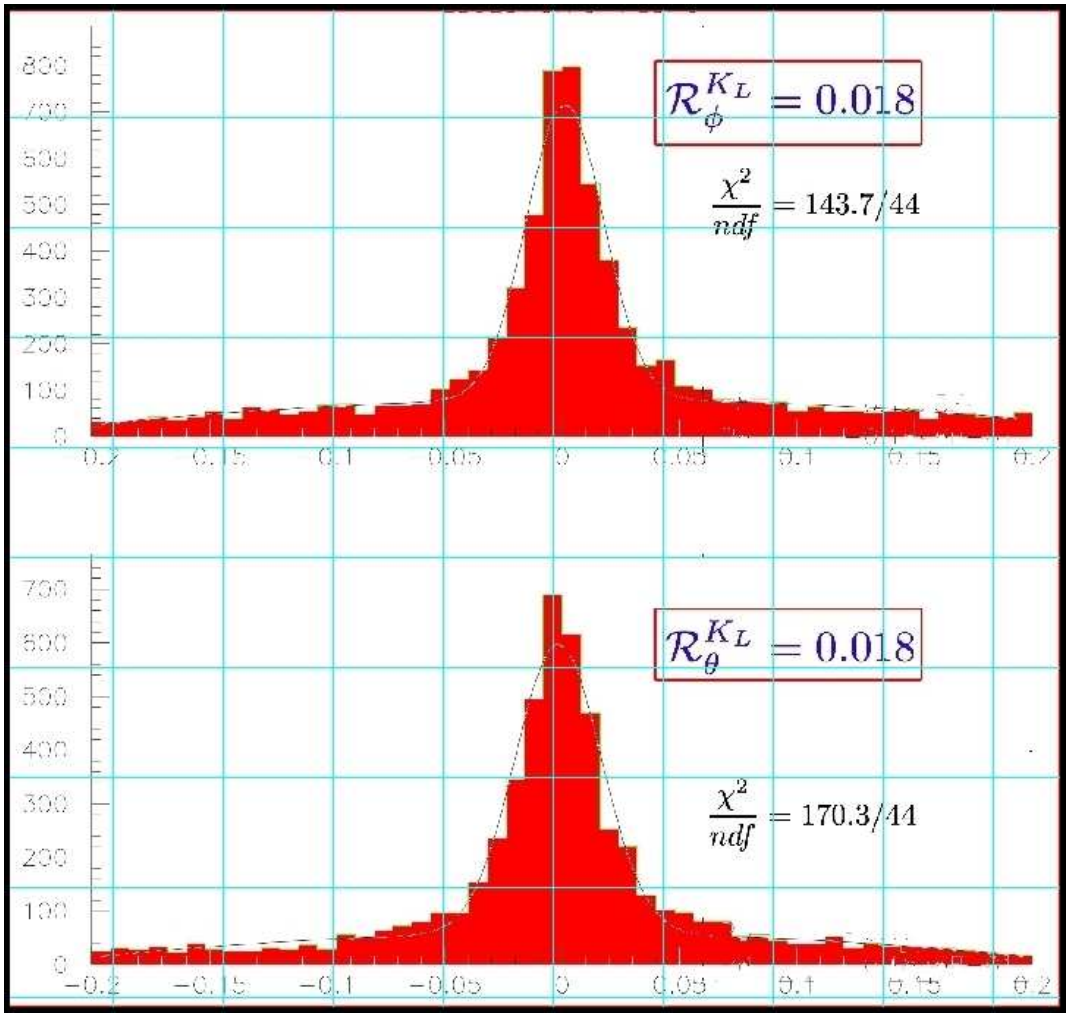

Table 3.8: The angular resolutions of K_S and two types of K_L are summarized here. The result is from signal monte carlo. Note that the K_S resolutions could be 7 - 15 times better than that of K_L and the ecl type K_L resolution could be 2 times better than that of klm type K_L as expected.

	K_S^0	K_L^0	ECL K_L^0	KLM K_L^0	GOOD ECL K_L^0	GOOD KLM K_L^0
R_θ	0.0024	0.0165	0.0122	0.0219	0.0122	0.0222
R_ϕ	0.0019	0.0184	0.0135	0.0277	0.0137	0.0291

CROSS CHECK OF MONTE CARLO WITH EXPERIMENTAL DATA

For the purpose of cross checking with experimental data a very small sample of data viz. experiment 07 of Belle data was "skimmed"[10] and was analyzed for the decay $D^0 \to (K^0_S\pi^-)_{K^{*-}}\pi^+$. [11] Results are described in figures 3.19 and 3.20.

Figure 3.19: The experiment 07, belle data was analyzed for $D^0 \to (K^0_S\pi^-)\pi^+$ for cross check with monte carlo. The K^0_S, K^{*-} ,D^0, D^{*+}, δM distributions are shown here. D^{*+} mass is fitted with the selection window $0.143 \leq \delta M \leq 0.147$ defined as the signal window in delta-M (δM).

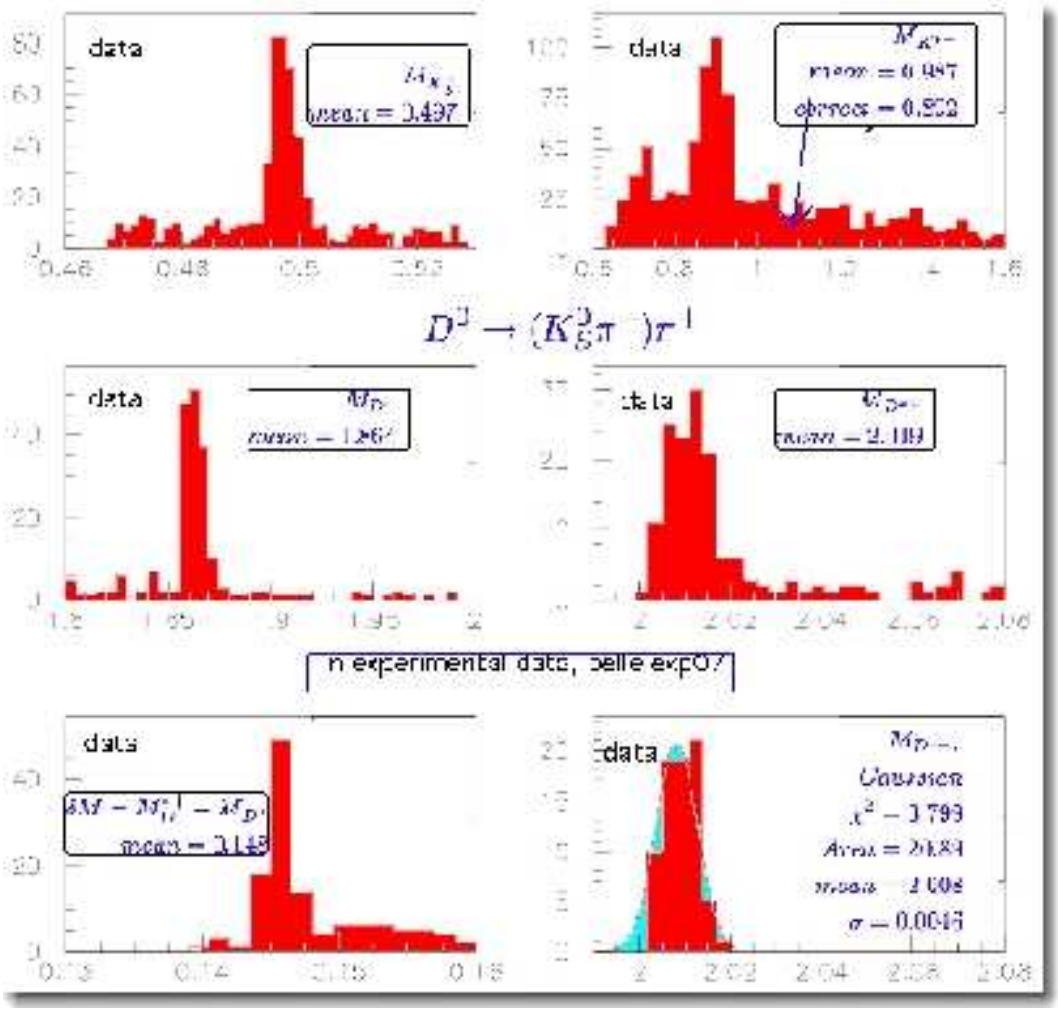

[10] reduced in size by applying preliminary event selection criteria

[11] mode 3, its charge conjugate mode $D^0 \to (K^0_S\pi^+)_{K^{*+}}\pi^-$ was not included

Figure 3.20: In experiment 07 data, reconstructed D^{*+} mass (in $D^0 \to (K^0_S\pi^-)\pi^+$) with a veto on events without matching generated information is fitted to a Gaussian and the yield, mean and resolution are given with the errors on the plot.

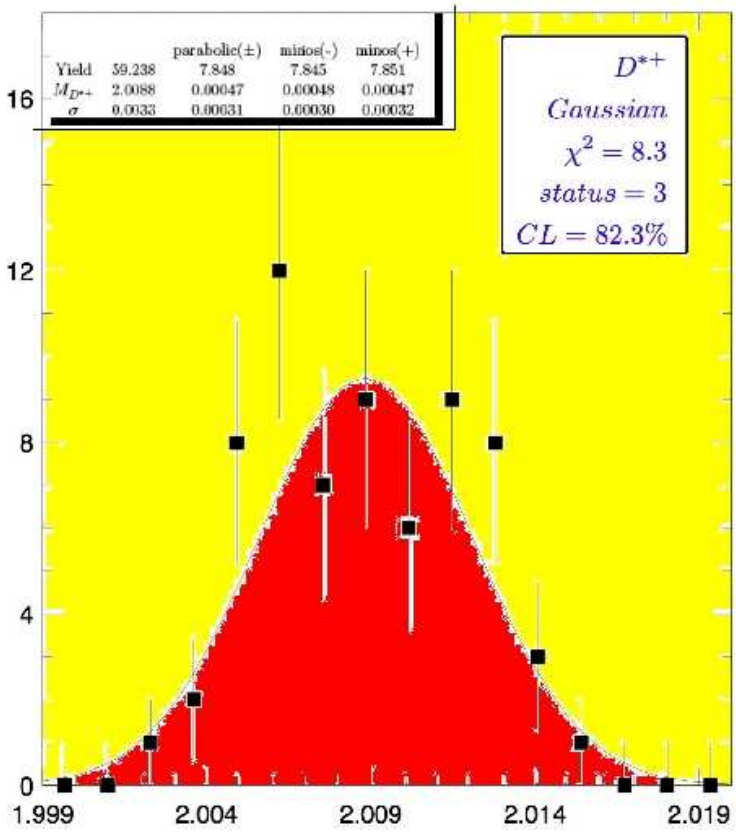

HIGHER STATISTICS

A more sofisticated set of software was developed to perform further analysis. 100,000 monte carlo signal events were generated and "simulated" through the detector for each of the 4 modes of our analysis.[12] A more studied set of event selction cuts inclusive of some of the previous cuts were used, see table 3.9 .[13,14,15] The results of this study are shown in figures 3.21, 3.22, 3.23, 3.25, 3.24, 3.26 and 3.27.

[12] In-fact the charge conjugate (cc) modes are not yet included.

[13] The $K_S\pi\pi$ mode has 90,000 events for the analysis due to a technical snag

[14] for $e^+e^- \rightarrow c\bar{c} \rightarrow fragmentation \rightarrow D^{*+}, inclusive$, raise "inclusive particle type" in evtgen

[15] libraries of Belle software used are; evtgen: b20040727-1143, Geant: b20030807-1600, analysis : b20040727-1143

Table 3.9: An updated analysis with newer event selection criteria. All masses are given in GeV.

# OF EVENTS 100000	GENERATOR EVTGEN	DETECTOR GEANT	PHYSICS PROCESS CHARM FRAGMENTATION	VETO ON EVENTS AT-LEAST 1 D^{*+}
π^0	″mdst_pi0″			
K_S	″mdst-vee2″	$dr > 0.25\,cm$	$d\phi < 0.1\,rad$	$dz < 1\,cm$
K_L	″mdst-klong″	-	-	-
$K_s\pi$	$0.486 < M_{K_S} < 0.510$	-	$1.75 < M_{D^0} < 1.90$	$0.144 < \delta M < 0.147$
$K_L\pi$	-	-	M_{D^0} fixed	3σ on $M_{D^{*+}}$
$K_S\pi\pi$	$0.491 < M_{K_S} < 0.504$	$0.750 < M_{K^{*-}} < 1.000$	$1.85 < M_{D^0} < 1.88$	$0.143 < \delta M < 0.148$
$K_L\pi\pi$	-	$0.752 < M_{K^{*-}} < 1.032$	M_{D^0} fixed	3σ on $M_{D^{*+}}$

Figure 3.21: The $K_S\pi^0$ mode analysis in signal monte carlo With the 100000 monte carlo sample all the 4-decay modes were analyzed, without their cc modes. This corresponds to event selection in table 3.9. The $K_S\pi^0$ mode is shown here.

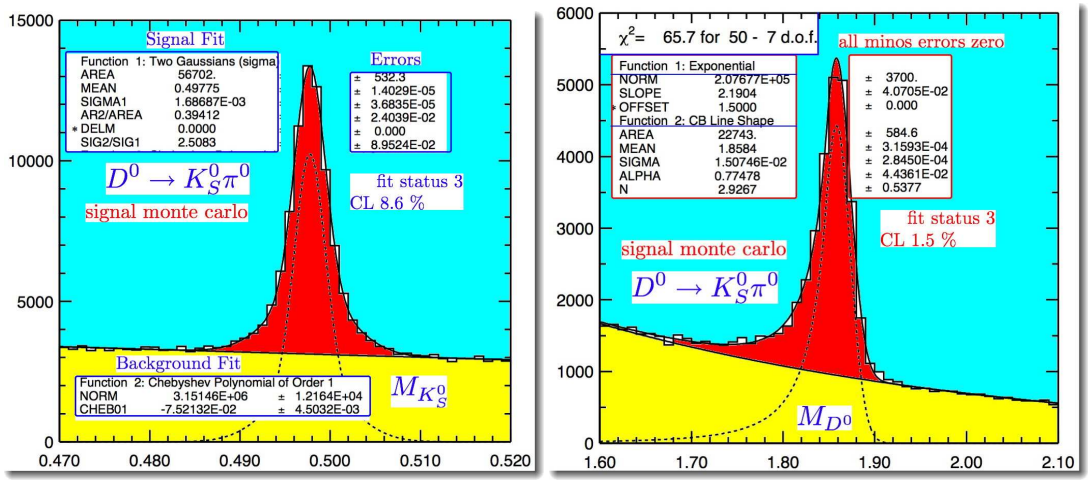

Figure 3.22: The signal distribution for $K^0_S\pi^0$ is shown in this figure.

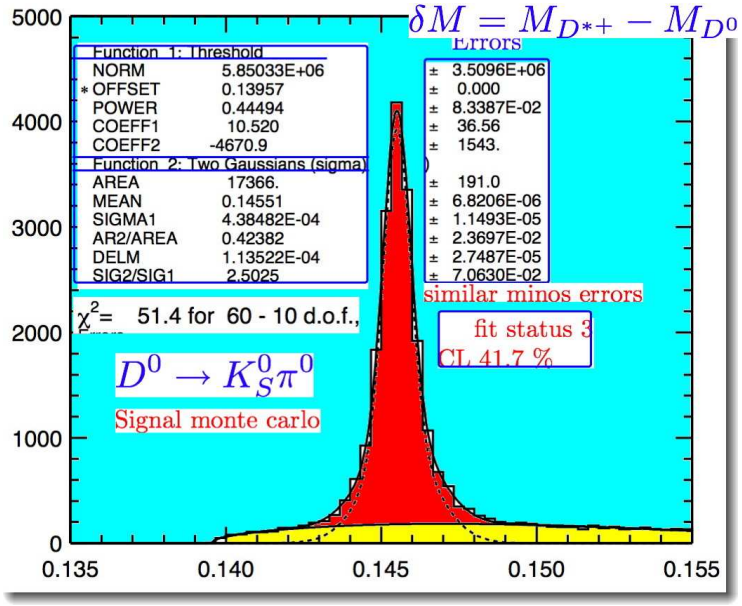

Figure 3.23: The $K_L\pi^0$ mode analysis in signal monte carlo The $K_L\pi^0$ mode is analyzed with 100000 events.

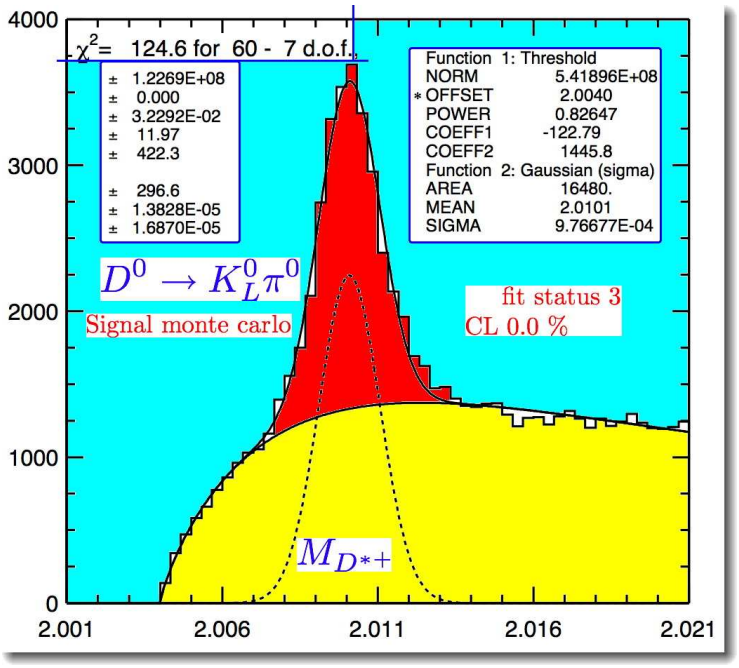

Figure 3.24: The $(K_S\pi)\pi$ mode analysis in signal monte carlo. The candidates selection for the $(K_S\pi)\pi$ mode analyzed are shown in this plot.[16]

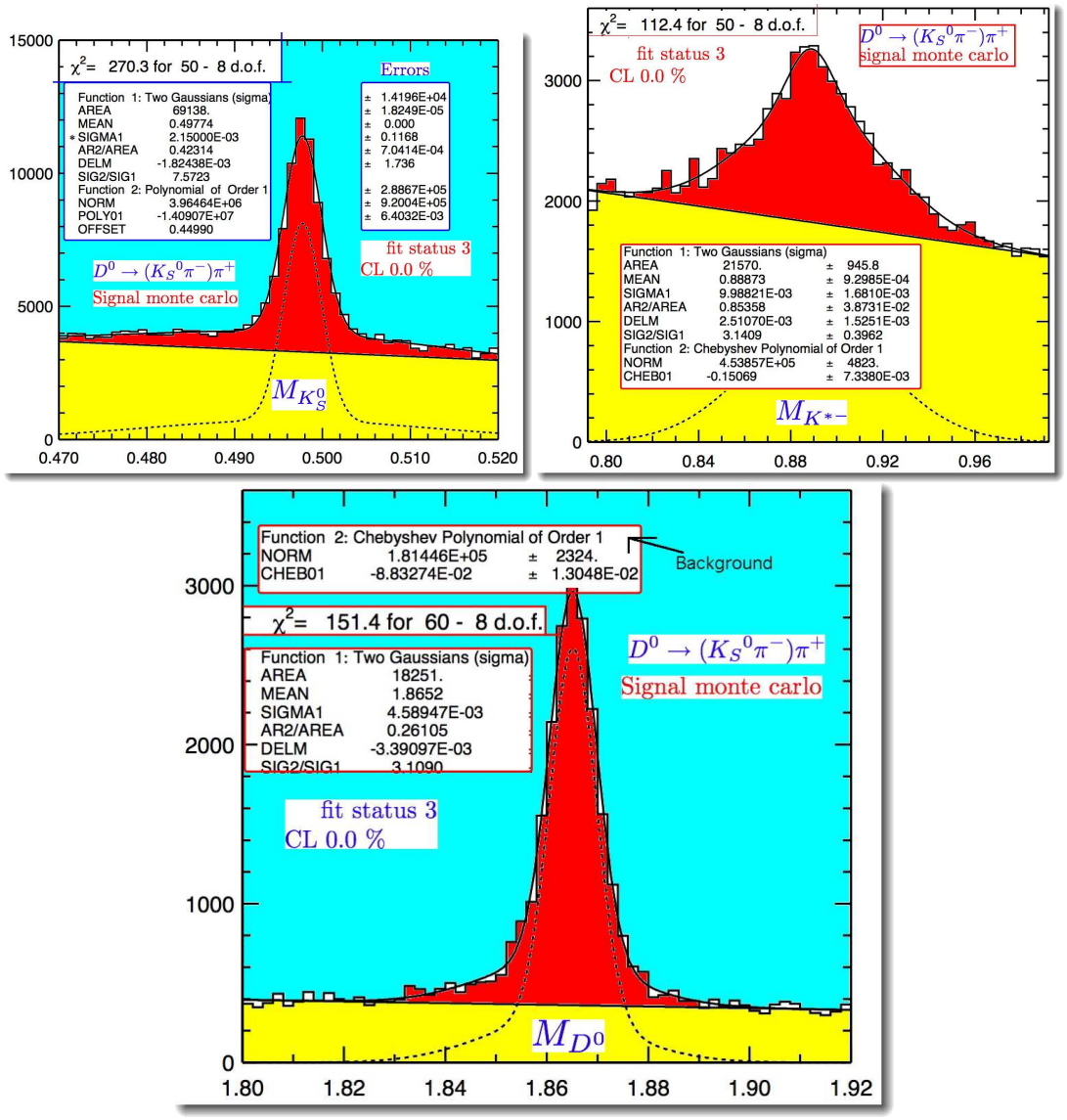

Figure 3.25: The signal distribution for $(K_S^0\pi)\pi$.

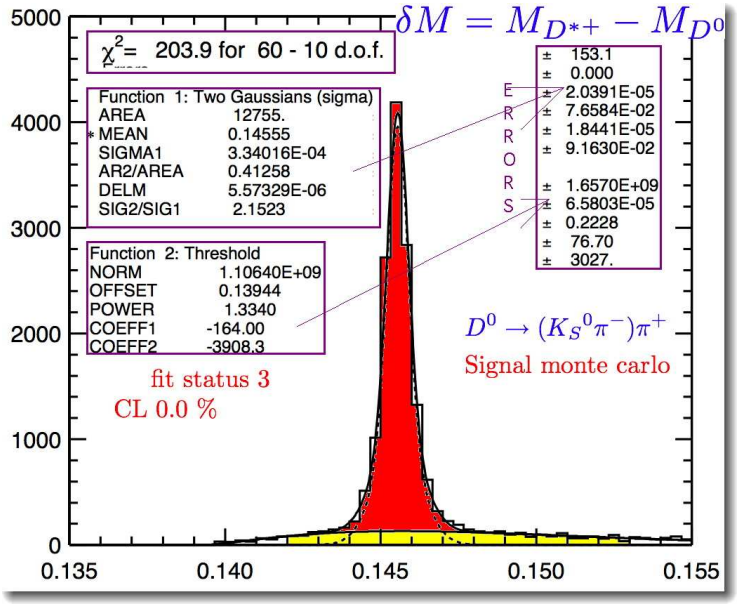

Figure 3.26: The $(K_L\pi^+)\pi^-$ mode analysis in signal monte carlo. The K^{*-} candidates for the $(K_L\pi)\pi$ mode.

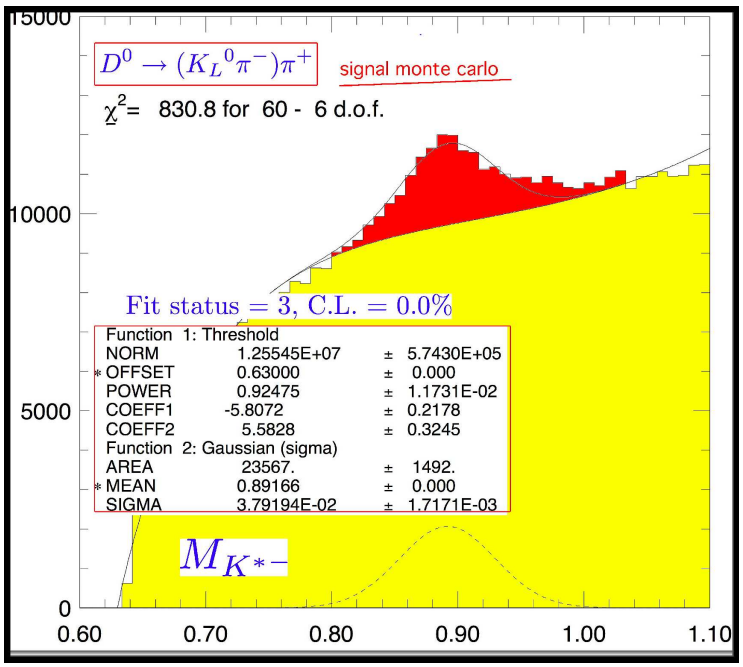

Figure 3.27: The distribution of $D^0 \to K^0_L \pi\pi$ signal in signal monte carlo of 100000 events.

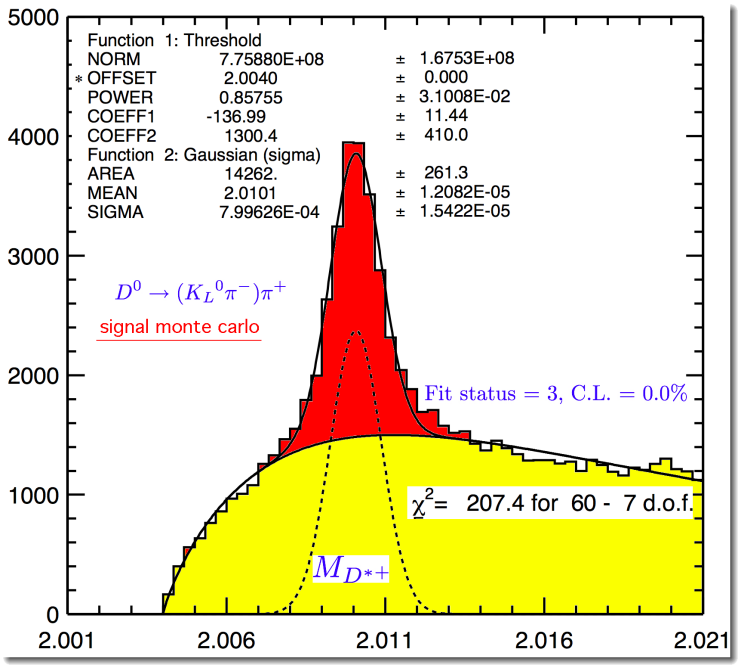

FACTORIZABILITY OF EFFICIENCIES

Another important study that was performed at this level of the analysis was to verify the so called factorizability of the efficiencies. This analysis is based on the understanding that many of the systematics of reconstruction in the analysis are cancelled out by the ratio of calibration modes to the signal modes because of same final state particles. In otherwords the efficiencies factor out to cancel each other except for the K_S-K_L efficiencies. This is possible if the efficiency of the signal D^* is a product of the efficiencies of its candidates, viz, the π^0, K_S, π^+ efficiency etc, for each mode.

The idea of factorization of efficiencies is checked in signal monte carlo. To match the generated K_L with the reconstructed one an angular veto is used on the same. K_S etc are matched by using standard belle software modules. [get_hepevt()] The efficiency is studied as a function of the lab momentum of the particles.

This study is described in the following itemized steps.

- ♢ Plot the generated lab momenta p_1.
- ♢ Count the matching number of events reconstructed in each bin
- ♢ Obtain 1-dim. efficiencies as function of momenta eg $\varepsilon^1(p_1)$ etc
- ♢ Scatter plot the generated lab momenta pair wise
- ♢ Count the number of reconstructed D^{*+} events matching in each 2-dim. bins
- ♢ Obtain the efficiency of D^{*+} as function of 2 momenta eg $\varepsilon^{D^{*+}}(p_1, p_2)$
- ♢ Plot $\varepsilon^1(p_1)$, $\varepsilon^2(p_2)$, $\varepsilon^{D^{*+}}(p_1, p_2)$ and $\varepsilon^1(p_1) \times \varepsilon^2(p_2)$ [figure 3.28]
- ♢ Compare $\varepsilon^{D^{*+}}(p_1, p_2)$ and $\varepsilon^1(p_1) \times \varepsilon^2(p_2)$
- ♢ Check ratio of $\varepsilon^{D^{*+}}(p_1, p_2)$ to $\varepsilon^1(p_1) \times \varepsilon^2(p_2)$, this should be flat, see figure 3.29. [a]
- ♢ Lemma $\varepsilon^{D^{*+}}(p_1, p_2, p_3) = N_3(p_3) \times \varepsilon^{D^{*+}}(p_1, p_2)$, since p_3 is constrained by D^{*+} kinematics, here N_3 is some scale factor.
- ♢ Implication $\int \varepsilon^{D^{*+}}(p_1, p_2, p_3)\, dp_3 = \int N_3(p_3)\, dp_3 \times \varepsilon^{D^{*+}}(p_1, p_2)$
- ♢ Assume factorization, i.e. $\varepsilon^{D^{*+}}(p_1, p_2, p_3) = \varepsilon^1(p_1) \times \varepsilon^2(p_2) \times \varepsilon^3(p_3)$, this $\Longrightarrow \int \varepsilon^{D^{*+}}(p_1, p_2, p_3)\, dp_3 = [\int \varepsilon_3(p_3)\, dp_3] \times \varepsilon^1(p_1) \times \varepsilon^2(p_2)$
- ♢ Implication from the above $\varepsilon^{D^{*+}}(p_1, p_2) = \frac{\int N_3(p_3)\, dp_3}{\int \varepsilon_3(p_3)\, dp_3} \times \varepsilon^1(p_1) \times \varepsilon^2(p_2)$, this means the ratio is flat.
- ♢ The results for the $D \to K_S\pi$ mode and the $D \to K_L\pi$ mode are partly shown in [figure 3.30 and 3.30] . The $D \to (K_S\pi)\pi$ mode is shown in appendix. The $(D \to K_L\pi)\pi$ mode was not studied.

[a] A fit to this figure is summarized in table 3.10 for $D \to K\pi$ mode.

Figure 3.28: Recognizing in the decay$D \to K_S\pi^0$, K_S's generated lab momentum p_1 or p_1^{gen},π^0's generated lab momentum p_2 or p_2^{gen} and π^+_{slow}'s generated lab momentum p_3 or p_3^{gen} where π^+_{slow} is π^+ from $D^{*+} \to D^0\pi^+$ the following plots show the individual reconstruction efficiencies ($\varepsilon^1(p_1)$, $\varepsilon^2(p_2)$ and $\varepsilon^3(p_3)$) of the final state particles (K_S, π^0, π^+) as a function of their generated lab momenta (p_1, p_2 and p_3). Further recognizing the 2-D efficiency functions $\varepsilon^{D^{*+}}(p_1, p_2)$ as the efficiency of D^{*+} in the lab momenta p_1 and p_2 and other pair wise efficiency functions $\varepsilon^{D^{*+}}(p_2, p_3)$ etc, this figure shows how the efficiency $\varepsilon^{D^{*+}}(p_1, p_2)$ factors out into $\varepsilon^1(p_1)$, $\varepsilon^2(p_2)$ and so on. To prove this we take a ratio of $\varepsilon^{D^{*+}}(p_1, p_2)$ to the 2-D efficiency function formed by the product of $\varepsilon^1(p_1)$ and $\varepsilon^2(p_2)$ and fit the resulting 2-D efficiency function. This ratio should be flat as explained in Section 3.2.

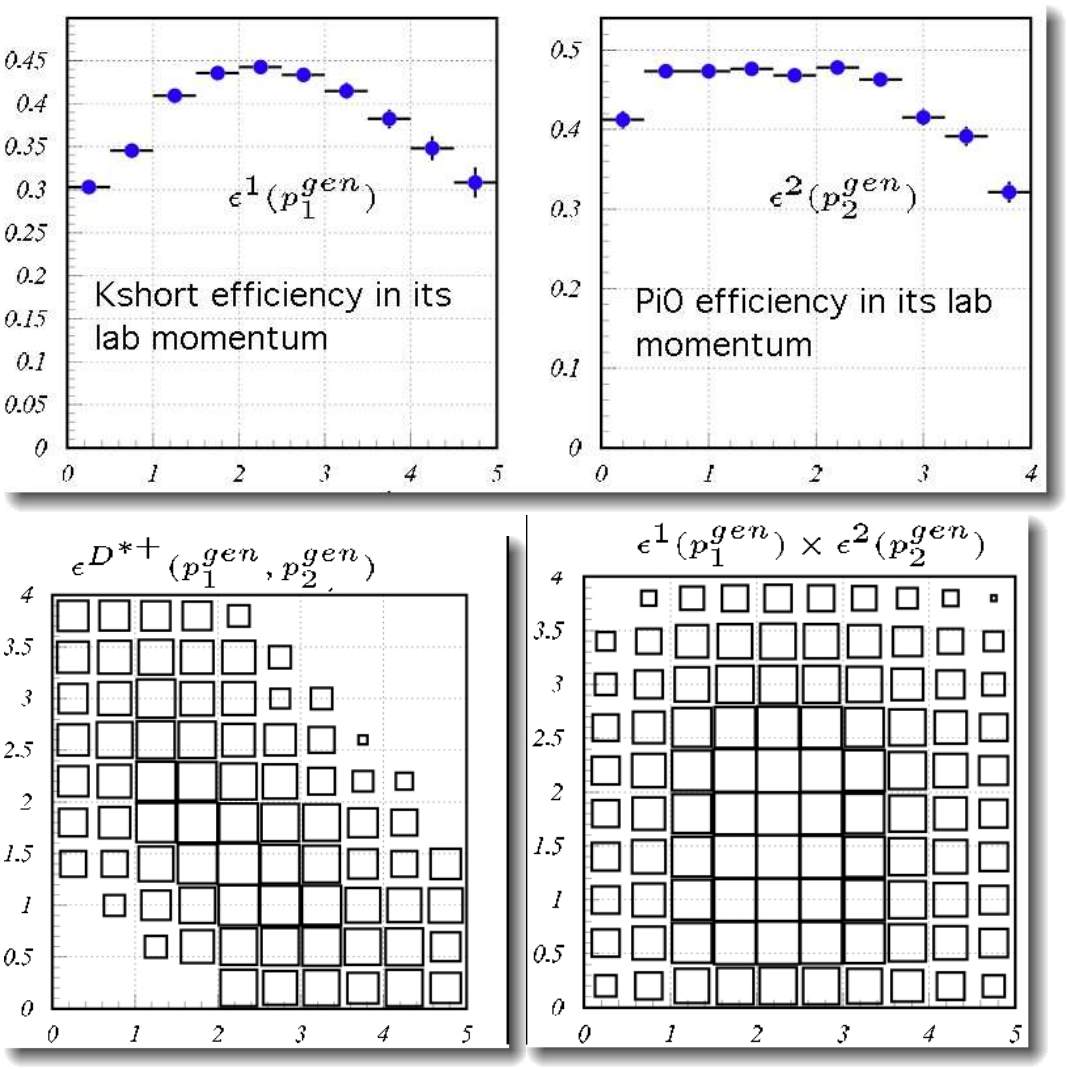

Figure 3.29: The ratio of $\varepsilon^{D^{*+}}(p_1, p_2)$ to the 2-D efficiency product of $\varepsilon^1(p_1)$ and $\varepsilon^2(p_2)$ is fited to a 2-D efficiency function of the form $f(x,y) = (P_1 + P_2X + P_3X^2) \times (P_4 + P_5Y + P_6Y^2)$.

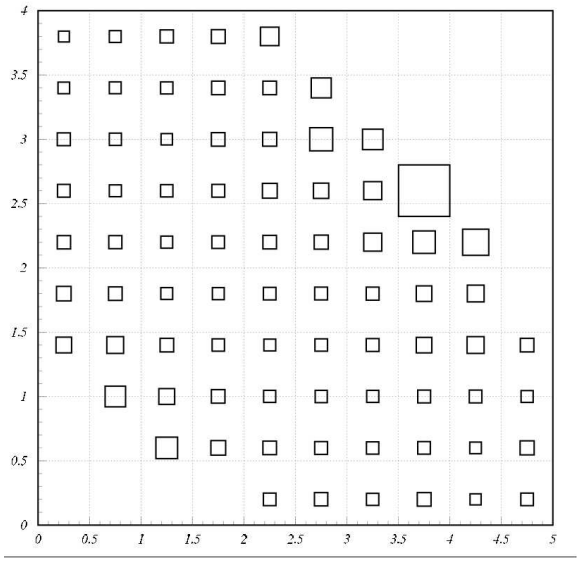

Table 3.10: The terms independent of X, Y are orders of magnitude bigger than terms dependent on X, Y. This proves that the ratio fits well to a flat function and the efficiencies factor out.

	P_1	$P_2\ (X)$	$P_3\ (X^2)$	P_4	$P_5\ (Y)$	$P_6\ (Y^2)$
Value	0.9977	0.08857	-0.01459	0.9977	0.08857	-0.01459
Error	1.6072	0.6595	0.1951	1.6072	0.6595	0.1951

Figure 3.30: factorization in $K_L\pi$ mode here.

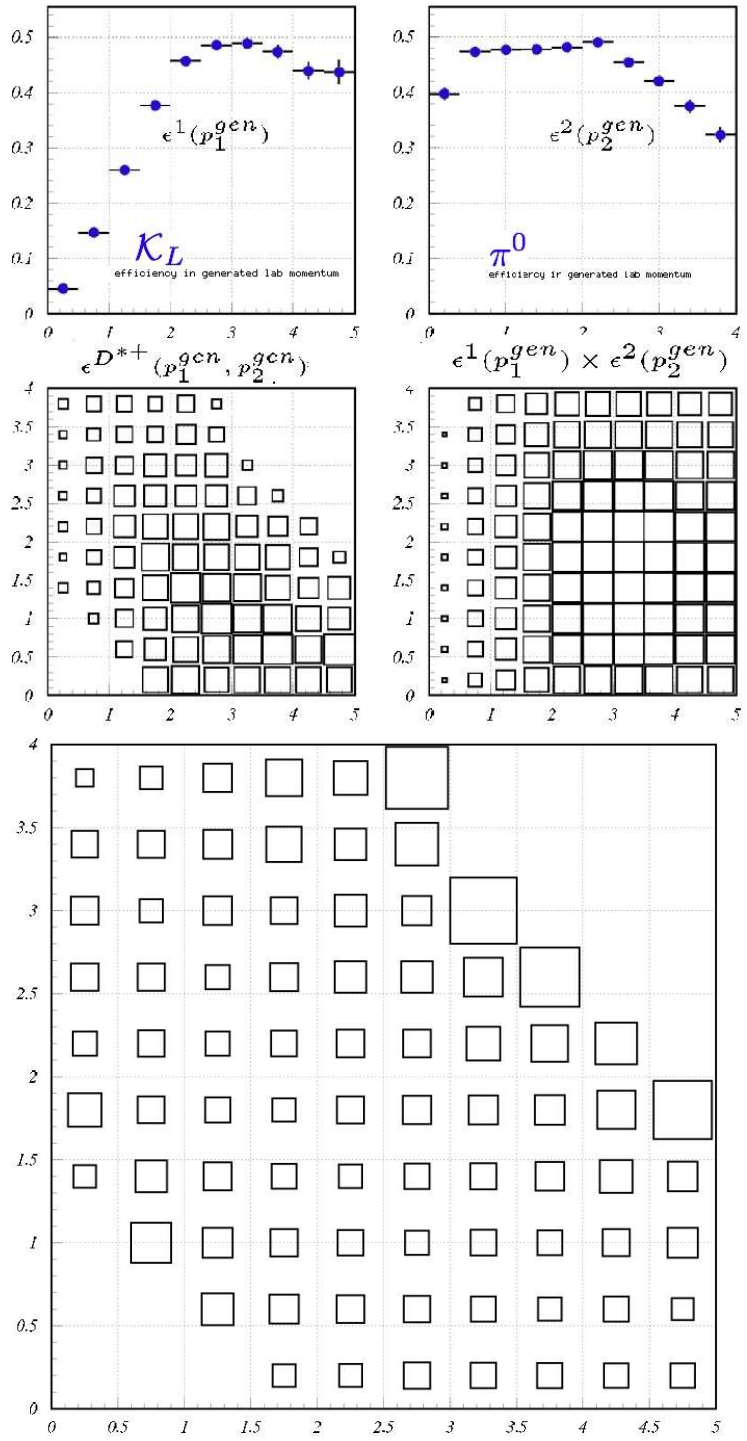

Chapter 4

Signal and Background in Inclusive Monte Carlo

in this chapter...the measurement performed in inclusive monte carlo is described and the signal yields and background modes are obtained.

4.1 EVENT SELECTION

The data sample used for this analysis amounts in total to an integrated luminosity of 32 fb^{-1} of Belle experimental data. The generic/inclusive monte carlo sample analyzed is roughly 3 $\times$ experimental data used. We select D^* candidates with **reconstructed scaled momentum**[a], x_p, given by $0.6 < x_p < 1.0$, which rejects D^*s from B-meson decays and supresses the combinatoric background.

[a] defined as $x_p = p^*/\sqrt{E_{beam}^2 - M^2}$, where p^* is D^* momentum in cms frame, E_{beam} is beam energy and M is mass of D^*

In addition to the standard reconstruction procedure for $\pi^{\pm}$, π^0, and K_S^0, the daughter γs of the π^0 are rejected if their energy is less than 50 MeV. The K_S are also required to satisfy the following quality criteria:

the $K_S \to \pi^+\pi^-$ vertex should be separated from the interaction point in the plane perpendicular to the beam axis by more than 500 μm;

the distance along the beam axis between the $\pi^{\pm}$ tracks at the K_S vertex must be less than 1 cm;

the cosine of the angle between the assumed K_S flight path from the interaction point to the decay vertex and the reconstructed K_S momentum in the transverse projection with respect to the beam must be more than 0.95.

K_L^0 reconstruction involves a potential background source from KLM clusters caused by unreconstructed charged particles, particularly when these particles do not originate from the interaction region[1]. These are rejected by vetoing the KLM clusters with a match, to calorimeter clusters of energy between 0.15 and 0.3 *GeV*. This corresponds to minimum ionization energy.

The dominant part of the background is due to the pickup of arbitrary soft pions when forming a D^0 candidate. A characteristic feature of such combinations is that the D^0 mass is accommodated by assigning a large momentum to the K^0, which then accounts for most of the D^0 momentum. Therefore the K^0 flight angle with respect to the D^0 boost[2] for this background tends to peak

[1] e.g. in-flight decays of K and π

[2] hereafter θ_{DK}

Figure 4.1: K^0 flight angle with respect to the D^0 boost, θ_{DK}, in the true signal [with a veto on non-signal in the inclusive monte carlo sample], from experiment 07-13 charm montecarlo.Note that the $\widetilde{K_L}$ are actually as K_S reconstructed like K_L, so the plots show what the D^0 mass method does to K_s.

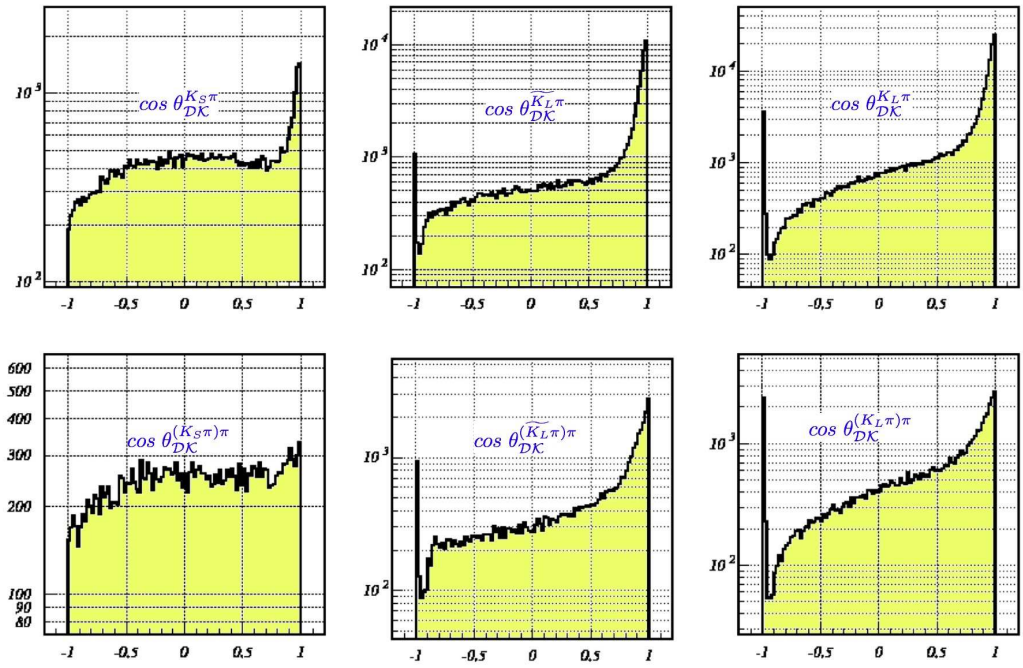

in the forward direction (Fig. 4.1) while for the signal the underlying distribution is isotropic, with a slight tilt to the forward direction in the measured distribution due to detector efficiency.

The sharp peak around $\cos\theta_{DK} = -1$ is due to the degenerate case when a random π^0 or $\pi^+\pi^-$ system can form a "good" D^0 with a K^0 almost at rest in the laboratory frame: to exclude these cases, we require $\cos\theta_{DK} > -0.95$. The upper cut on this quantity needs optimization which was performed in a previous study at Belle using signal MC and data in the M_{D^*} sideband: we require $\cos\theta_{DK} < 0.2$ for all four modes.

The invariant mass of the $K^0\pi^-$ combination in the $(K^0\pi^-)\pi^+$ mode is required to lie within 50 MeV/c^2 of the nominal $K^*(892)$ mass. In addition the invariant mass of the $\pi^+\pi^-$ pair is required to be less than 0.7 GeV/c^2 to make the signal and the control modes kinematically similar, and to suppress the contribution from $K^0\rho$ decays.

Table 4.1: The details of amount of data used in analysis, experimental data Vs monte carlo, calculated from the logs of analyzed data.

EXPERIMENT #	DATA (IN fb^{-1})			GENERIC MC (IN fb^{-1})			DATA/MC
	4S	Cont.	Total	4S	Cont.	Total	Ratio
07	5.795	0.588	6.383	14.086	1.687	15.773	2.47
09	4.194	-	4.194	11.566	-	11.566	2.76
11	7.941	1.183	9.124	20.482	2.902	23.384	2.56
13	10.698	1.199	11.897	31.349	3.597	34.946	2.94
13, "R1 to R531"	2.701	0.515	3.216	8.067	1.546	9.613	2.99
07 - 13	28.628	2.97	*31.598*	77.483	8.180	*85.669*	*2.71*
07 - 13 R531	20.631	2.286	*22.917*	54.201	6.135	*60.336*	*2.63*

4.2 EVENT COMPOSITION STUDY

The event composition of the reconstructed signal was studied in great detail in monte carlo, which had 3 streams of mc data from Belle repository which amounts in terms of luminosity to nearly 2.7 times the size of the experimental data that was analysed, details of which are given in table 4.1.

Each of the decay mode that needed to be studied, including the background decay modes are identified in the main body of the data analysis code by a "tagging algorithm" at the level at which the decays were generated by Particle decay modules. Then each of these identified decay modes are flagged as a variable in the ntuple output. These decay modes can then be either vetoed or allowed at the data-analysis (n-tuple) level by the corresponding variable/flag.

The following decay modes in relation to this analysis were studied in the inclusive monte carlo sample:

Signal channels	$D^0 \to K_S \eta'(958)$	$D^0 \to K_L f_2(1270)$
$D^0 \to K_S \pi^0$	$D^0 \to K_S f_0(1370)$	$D^0 \to K_L f_0(1710)$
$D^0 \to K_L \pi^0$	$D^0 \to K_S f_2(1270)$	$D^0 \to \pi^+\pi^-\pi^0$
$D^0 \to K^{*-}(K_S\pi^0)$	$D^0 \to K_S f_0(1710)$	$D^0 \to \pi^+\pi^- K_S^0$
$D^0 \to K^{*-}(K_L\pi^0)$	$D^0 \to K_L \rho^0$	$D^0 \to \pi^+\pi^- K_L^0$
Background channels	$D^0 \to K_L \omega(782)$	$D^0 \to K^-\pi^+$
$D^0 \to K_S \rho^0$	$D^0 \to K_L \eta$	$D^0 \to K^{*-}K^+$
$D^0 \to K_S \omega(782)$	$D^0 \to K_L \eta'(958)$	
$D^0 \to K_S \eta$	$D^0 \to K_L f_0(1370)$	

The signal of the four decay modes of interest and the background modes each combined with their charge conjugate modes can thus be identified and separated from the rest of the feature and plotted against the latter. From the plots that are shown below [figures 4.2, 4.3, 4.4, 4.5, 4.6 and 4.7] one can see the large peaks which represent the signal in the monte carlo. Unexpectedly in some cases tiny peaks present under the signal peaks were found. These are the so called "peaking background" the details of which are shown after the above mentioned plots. For a colored output, all the background are color coded in the following way to distinguish them from each other. These are also numbered for the benefit of a situation where colored output is not possible. In each of the signal decay modes[3] the following color coding is followed for the plots in discussion above.

- ♢ Signal is shown in ***hatched red (# legend 1)***[a]
- ♢ Other $c\bar{c}$ backgrounds except for the peaking features is shown in ***blue (# legend 2)***[b]
- ♢ $b\bar{b}$ background[c] is shown in ***cyan(# legend 3)***
- ♢ All "u d s" backgrounds is shown in ***magenta(# legend 4)***
- ♢ Broad resonance, $\bar{K^0}\rho^0$ is shown in ***black(# legend 5)***
- ♢ "Other" broad resonances[d] and unidentified peakings are shown in ***green(# legend 6)***

[a] signal comes from $c\bar{c}$, both from "off Resonance"(continuum) and "on Resonance"
[b] combinatorics
[c] both mixed and charged types
[d] studied $\rho^0, \omega(782), \eta, \eta'(958), f_0(1370), f_2(1270), f_0(1710)$

[3] including two types of classification for the K_L^0 data sample, ecl and klm type

Figure 4.2: The $D^0 \to K^0_S \pi^0$ is reconstructed in Monte Carlo with suitable event selection criteria. This mode gives a very clean sample owing to the clean measurement of K^0_S. This mode is almost free of any contamination. While the combinatorics is negligible the peaking background present here can hardly be seen. The details of this modes composition is shown later. See table 4.2.

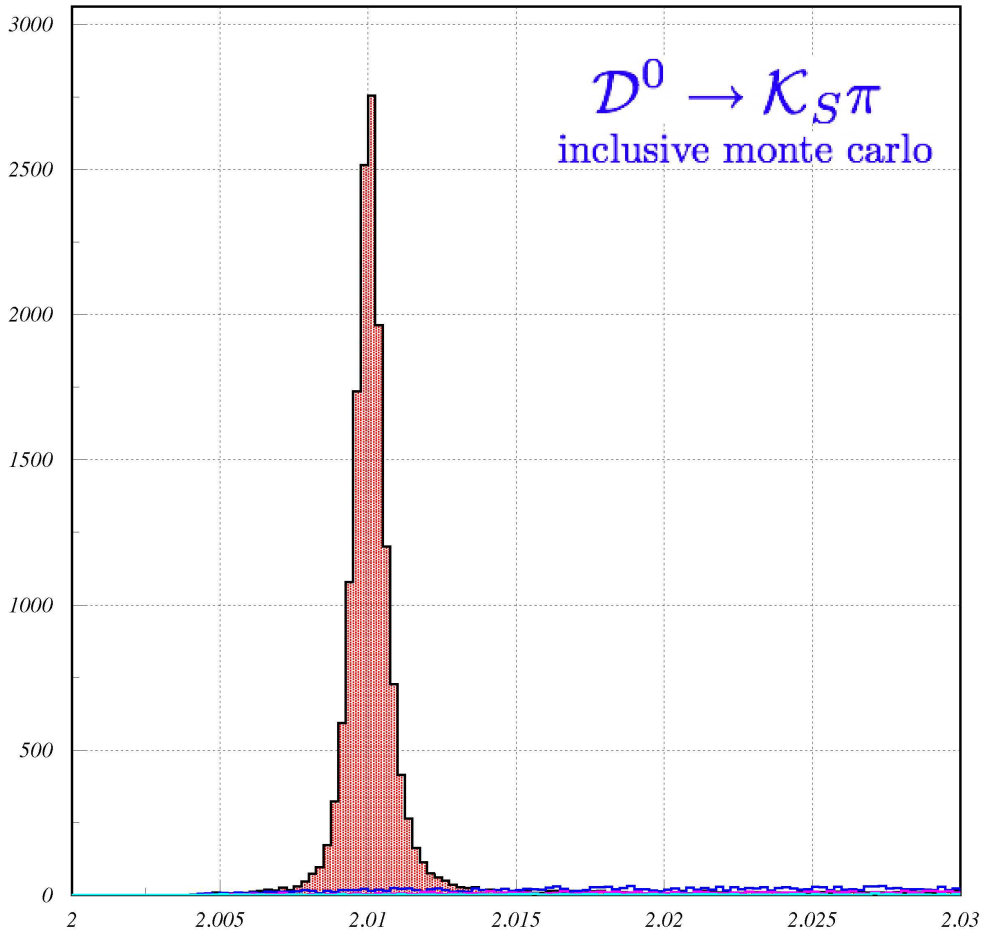

THE PEAKING BACKGROUNDS

A detailed description of the peaking backgrounds is given in this section. For brevity of space here, the backgrounds which do not produce any peaking components such as $b\bar{b}$ and uds and the non peaking components of $c\bar{c}$ will be given in the Appendix.

The detailed features are shown with descriptions in the following pages.

Figure 4.3: This plot shows the classification of different event types in the $D^0 \to K^0_L \pi^0$ signal reconstructed by the KLM, the large peak is $c\bar{c}$ signal. The blue curve is combinatorics and obviously free of any peaking features. The magenta is *bb* [mixed and charged] and cyan is uds type combinatorics.

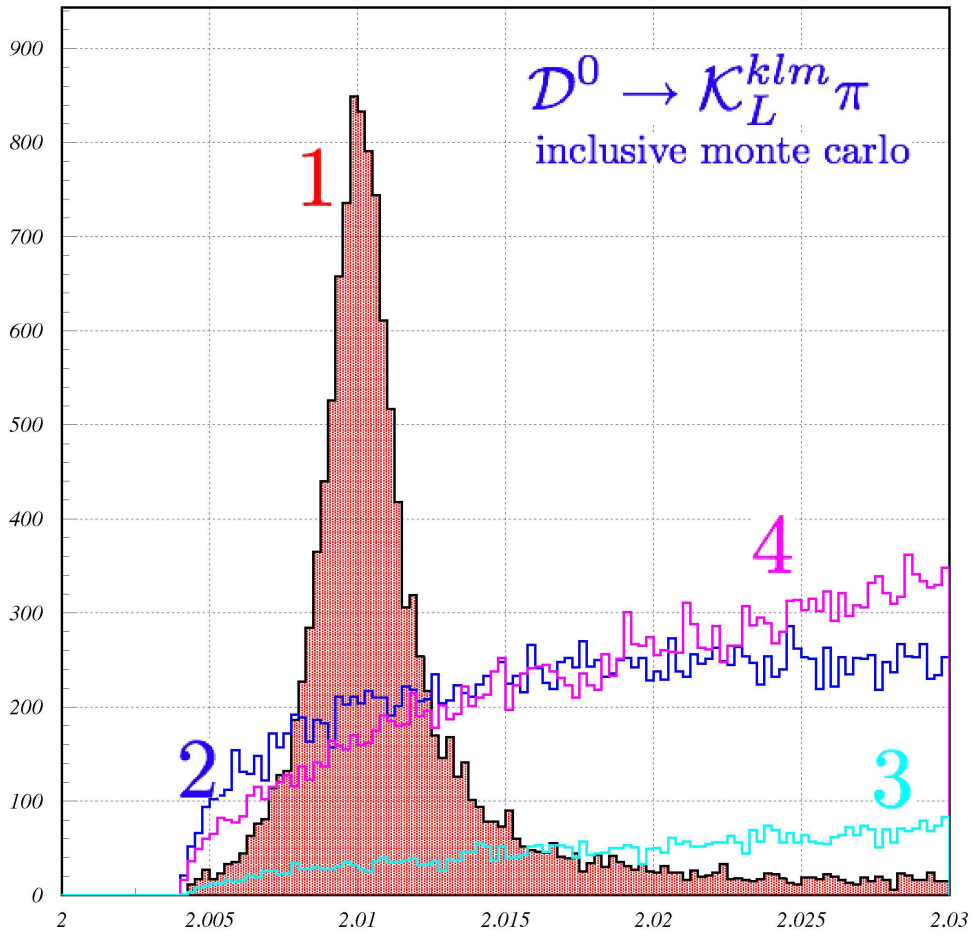

Figure 4.4: This plot shows the classification of different event types in the $D^0 \to K^0_L \pi^0$ signal reconstructed by the KLM and the ECL as evident by the narrow peak compared to the KLM signal for this mode. The large peak is $c\bar{c}$ signal. The blue curve is $c\bar{c}$ combinatorics and as before has no peaking features. The non-$c\bar{c}$ combinatorics is shown in magenta and cyan.

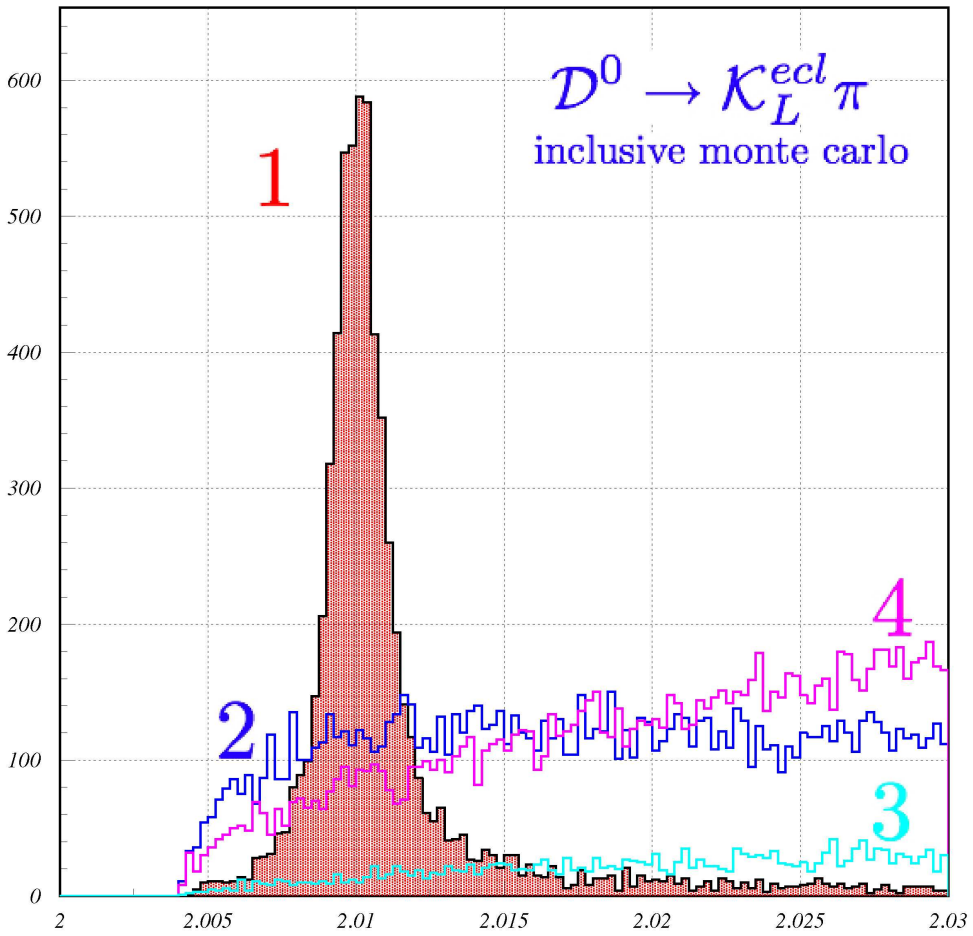

Figure 4.5: This plot shows the calibration signal $D^0 \to (K^0_S\pi^-)_{K^*}\pi^+$. This is a clean signal wrt the combinatorics. Apart from the signal peak there is a clear peak in black and one in blue although both are small. According to our classification described above the black is the peaking background $D^0 \to K^0_S\rho^0$. The blue is the unidentified peaking component. The other peaks present can't be seen here as they are tiny, they show up when plotted individually.

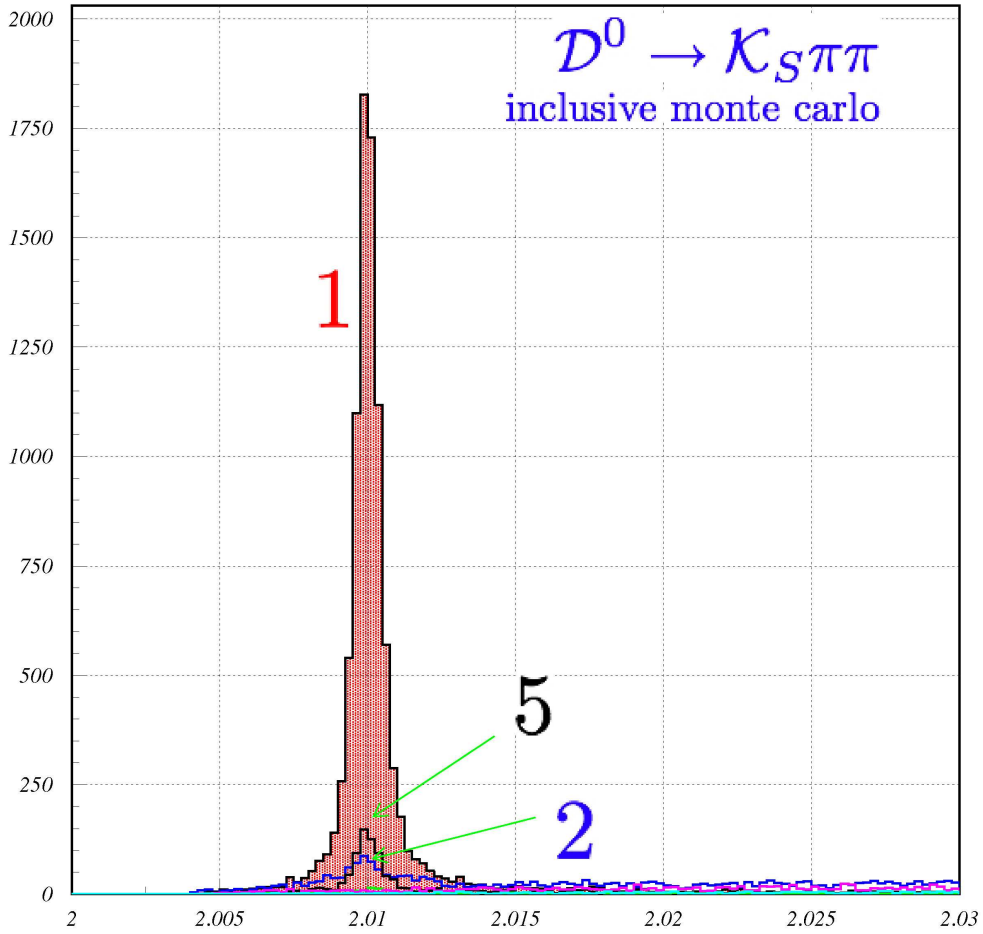

Figure 4.6: The calibration mode [mode3, klm type K_L] has significant amount of combinatorial background coming from continuum, $b\bar{b}$ and uds. There is also a small but prominent peaking background coming from the broad resonance $D^0 \to K_L\rho^0$. All though negligible the component seen in green here corresponds to roughly 1.1% of other broad resonances[4], see table 4.3. Infact klm type sample in this mode is free of any other contamination unlike the ecl type sample of the mode which contains several other peaking contaminations.

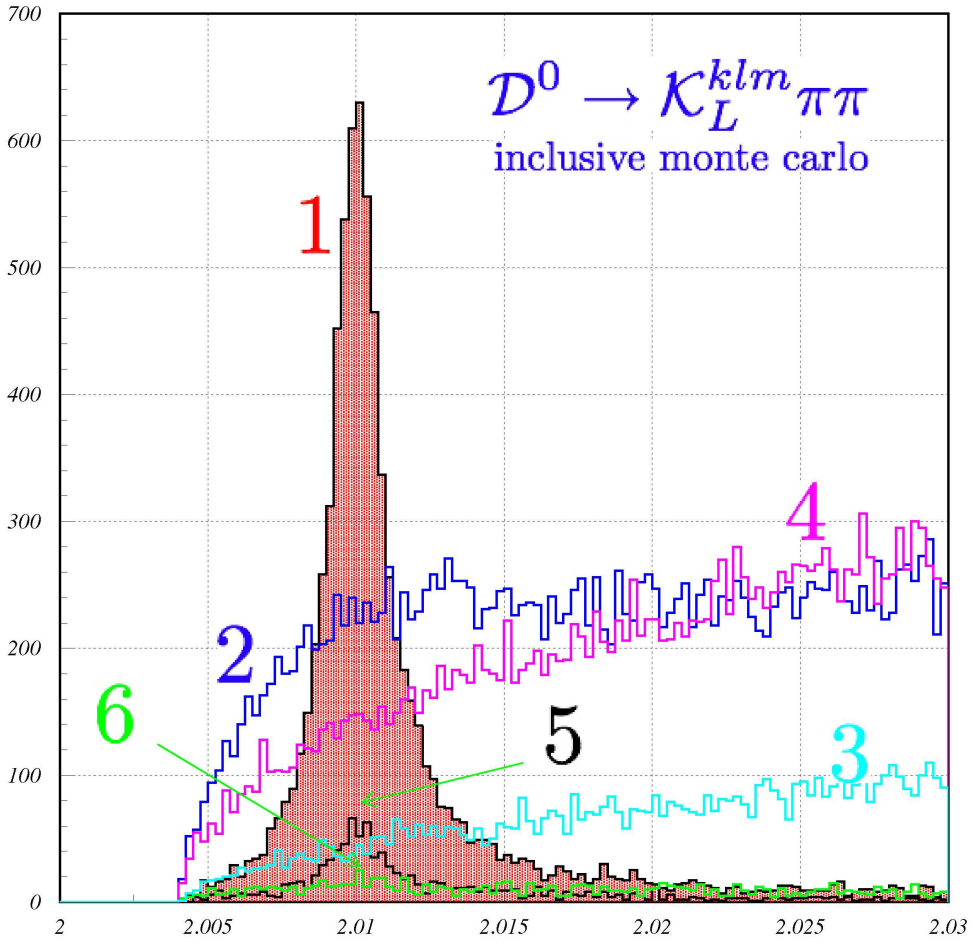

Figure 4.7:

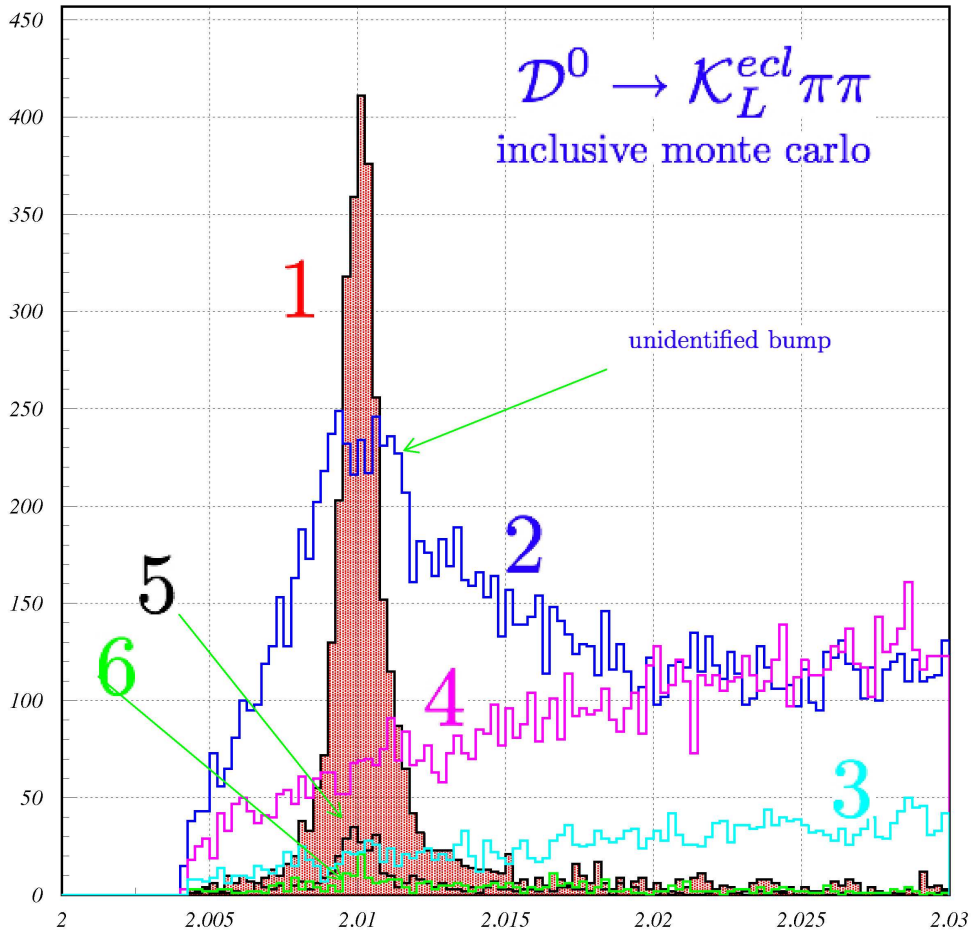
$\mathcal{D}^0 \to \mathcal{K}_L^{ecl}\pi\pi$
inclusive monte carlo
1
2
3
4
5
6
unidentified bump
450
400
350
300
250
200
150
100
50
0
2
2.005
2.01
2.015
2.02
2.025
2.03

Peaking background in "signal modes"

The only peaking background that is present in the signal modes[a] are the $D^0 \to \bar{K}R$ where R is the so called broad resonances defined earlier[b] . But fortunately the fraction of this background compared to the total yield is only 0.6% and moreover the small branching fraction of these decay modes would further ensure negligible error on the measurement. Also these peaking background pollutes only one of the signal mode. viz. the $D^0 \to K^0_S\pi^0$ mode, see figure 4.8.

[a] modes where we are trying to measure the asymmetry
[b] ρ^0, η, ω, f etc

Peaking backgrounds in "K_S calibration modes"

In mode $D^0 \to (K^0_S\pi^-)_{K^{*-}}\pi^+$, there are several peaking backgrounds present, viz. $D^0 \to K^0_S\rho^0$, the "other" broad resonances, $D^0 \to \bar{K}R$[a], and $D^0 \to K^-\pi^+$, $D^0 \to K^{*-}K^+$ and $D^0 \to K^{*+}K^-$, see figures 4.9, 4.10, 4.11, 4.12, 4.13.

[a] $R = \rho^0, \omega(782), \eta, \eta^{'}(958), f_0(1370), f_2(1270), f_0(1710)$

Peaking backgrounds in "K_L calibration modes"

We divide the other calibration mode, viz., $D^0 \to (K^0_L\pi^-)_{K^{*-}}\pi^+$, into two types, the ecl type and the klm type sample.

klm: this mode is contaminated by only the broad resonances background modes, $D^0 \to K^0_S\rho^0$ and the "other broad resonances"[a] each of them peaking under the signal. Any other peaking backgrounds do not contaminate this sample, see figure4.21 and figure 4.22.

[a] $\rho^0, \omega(782), \eta, \eta^{'}(958), f_0(1370), f_2(1270), f_0(1710)$

Table 4.2: The yields of the signal and peaking backgrounds in inclusive monte carlo for the signal modes. Note that all modes are almost free of any such contamination.

	YIELD	$\bar{K^0}\rho^0 + \bar{K^0}\eta + \bar{K^0}\omega + \bar{K^0}f$ etc	$K^-\pi^+$	$K^{*-}K^+$	$K^{*+}K^-$
$D^0 \to K_S^0\pi^0$	13959±133.06	91.49±11.07 (0.6%)	-	-	-
$D^0 \to K_L^{klm}\pi^0$	8957.6±302.57	-	-	-	-
$D^0 \to K_L^{ecl}\pi^0$	5313.6±320.34	-	-	-	-

Table 4.2 and 4.3 list all the peaking modes with the corresponding branching fractions from PDG 2006 and their yields and percentage yields wrt the yield of the signal.

Table 4.3: The yields of the signal and peaking backgrounds in inclusive monte carlo for the calibration modes.

	YIELD	$\bar{K^0}\rho^0$	$\bar{K^0}\eta + \bar{K^0}\omega + \bar{K^0}f$ etc	$K^-\pi^+$
PDG 2006 BF (%)		0.75+0.6-0.8		3.8±0.07
$D^0 \to (K^0_S\pi^-)\pi^+$	7937.6±101.70	521.96±26.49 (5.76%)	52.59±8.23 (0.58%)	39.19±7.48(0.43%)
$D^0 \to (K^{klm}_L\pi^-)\pi^+$	4665.5±121.76	354.22±37.89(6.98%)	55.88±19.94(1.10%)	-
$D^0 \to (K^{ecl}_L\pi^-)\pi^+$	2334.3±62.81	155.43±16.05(3.58)	35.15±8.08(0.81%)	115.49±26.22(2.66%)
	YIELD	$K^{*-}K^+$	$K^{*+}K^-$	UNIDENTIFIED
PDG 2006 BF (%)		0.2±0.11	0.37±0.08	
$D^0 \to (K^0_S\pi^-)\pi^+$	7937.6±101.70	86.11±9.56(0.83%)	78.54±8.91(0.87%)	334.57±56.56(3.70%)
$D^0 \to (K^{klm}_L\pi^-)\pi^+$	4665.5±121.76	-	-	
$D^0 \to (K^{ecl}_L\pi^-)\pi^+$	2334.3±62.81	30.12±46.03(0.69%)	72.00±21.56(1.66%)	1595.8±307.71(36.78%)

Figure 4.8: Broad Resonaces in $D^0 \to K^0_S\pi^0$ mode. The "peaking" broad resonaces $K_S\rho^0$+$K_S\eta$+ $K_S\omega$+$K_S f$ etc in $D^0(K\pi^0)$ region, peaking "yield" realative to signal yield is 0.6%.

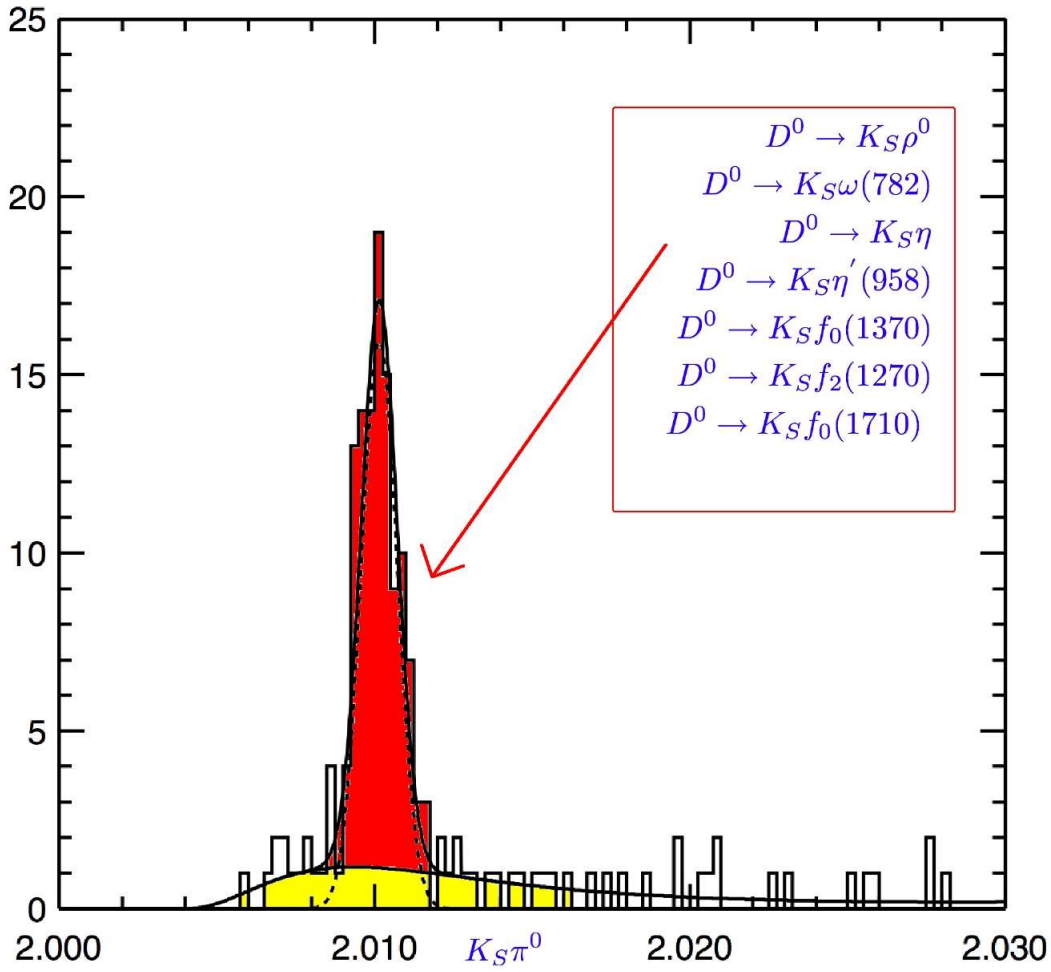

Figure 4.9: The $K^0_S\rho^0$ peaking in $D^0 \to K^0_S\pi^-\pi^+$ mode, *peaking to signal is 5.76%.*

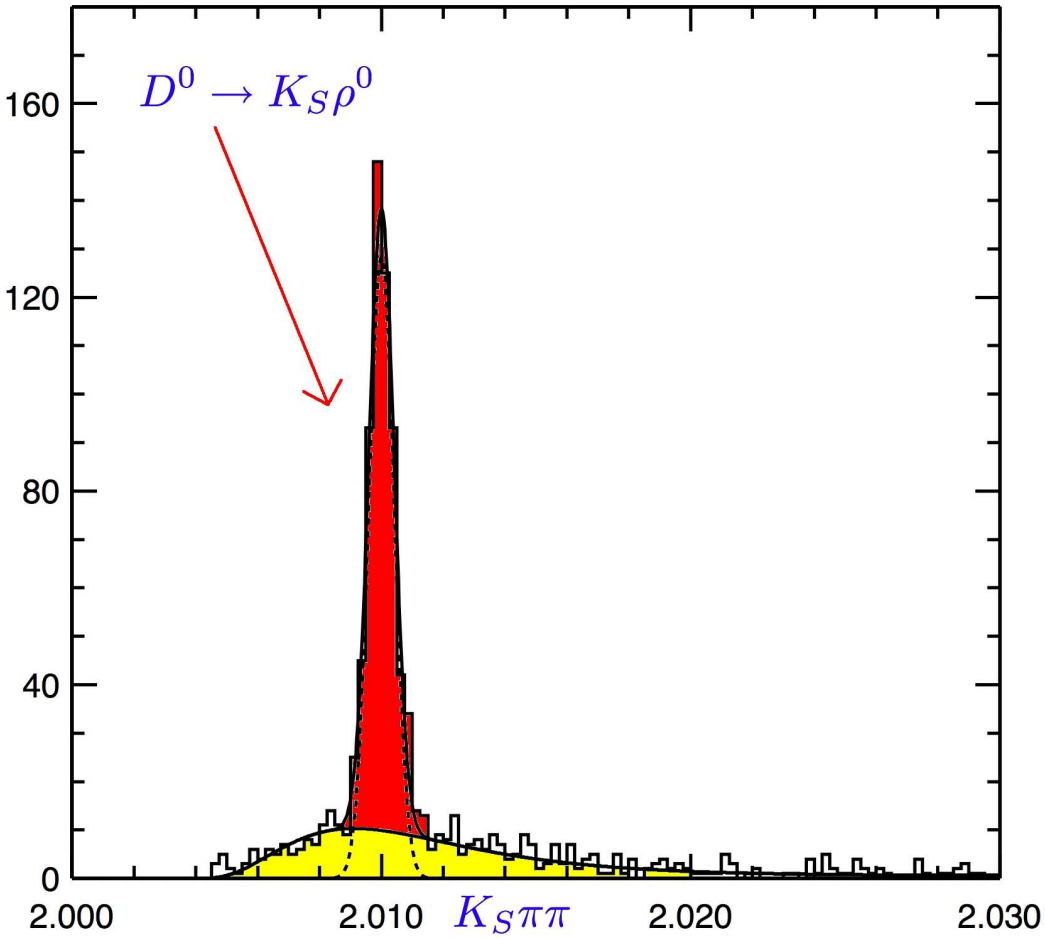

Figure 4.10: The $K_S\eta + K_S\omega + K_Sf$ etc peaking in $D^0 \to K^0_S\pi^-\pi^+$ mode, peaking to signal is 0.58%.

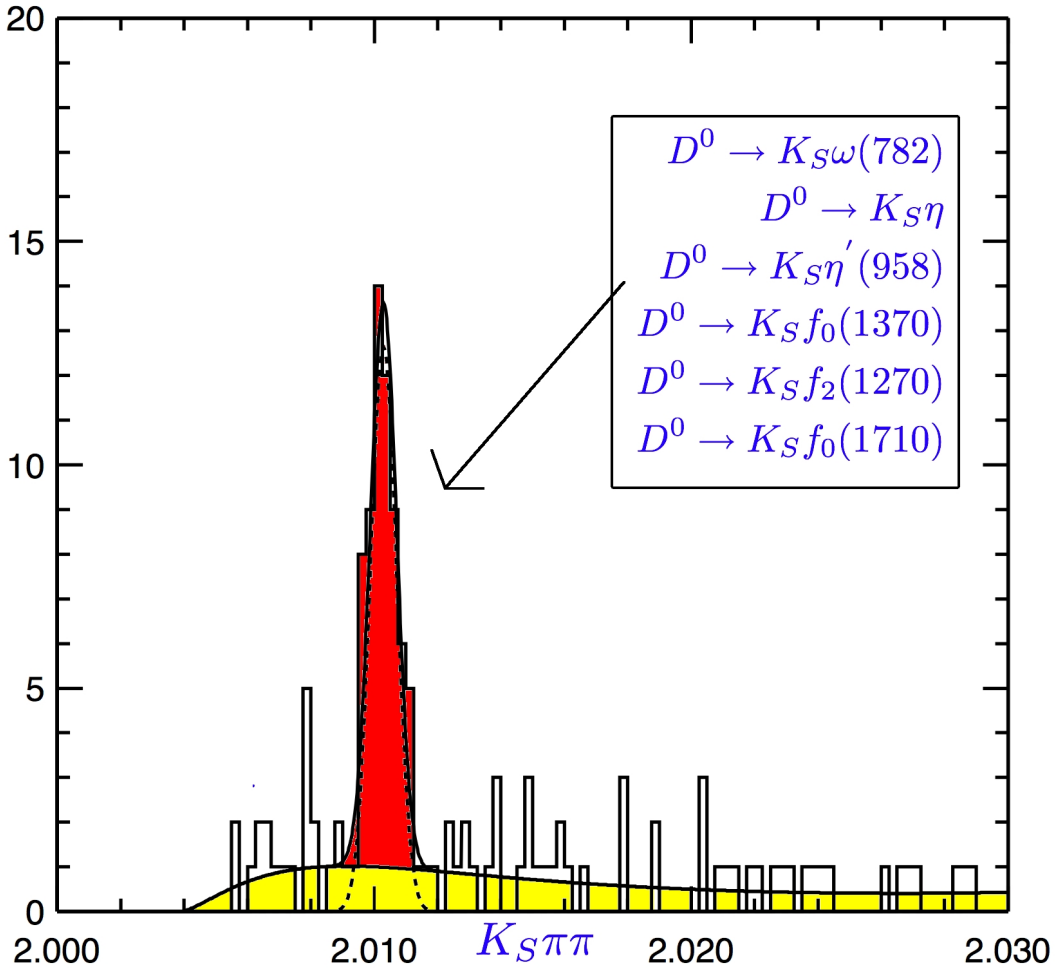

Figure 4.11: The $K^-\pi^+$peaking in $D^0 \to K^0_S\pi^-\pi^+$ mode, peaking to signal is 0.43%.

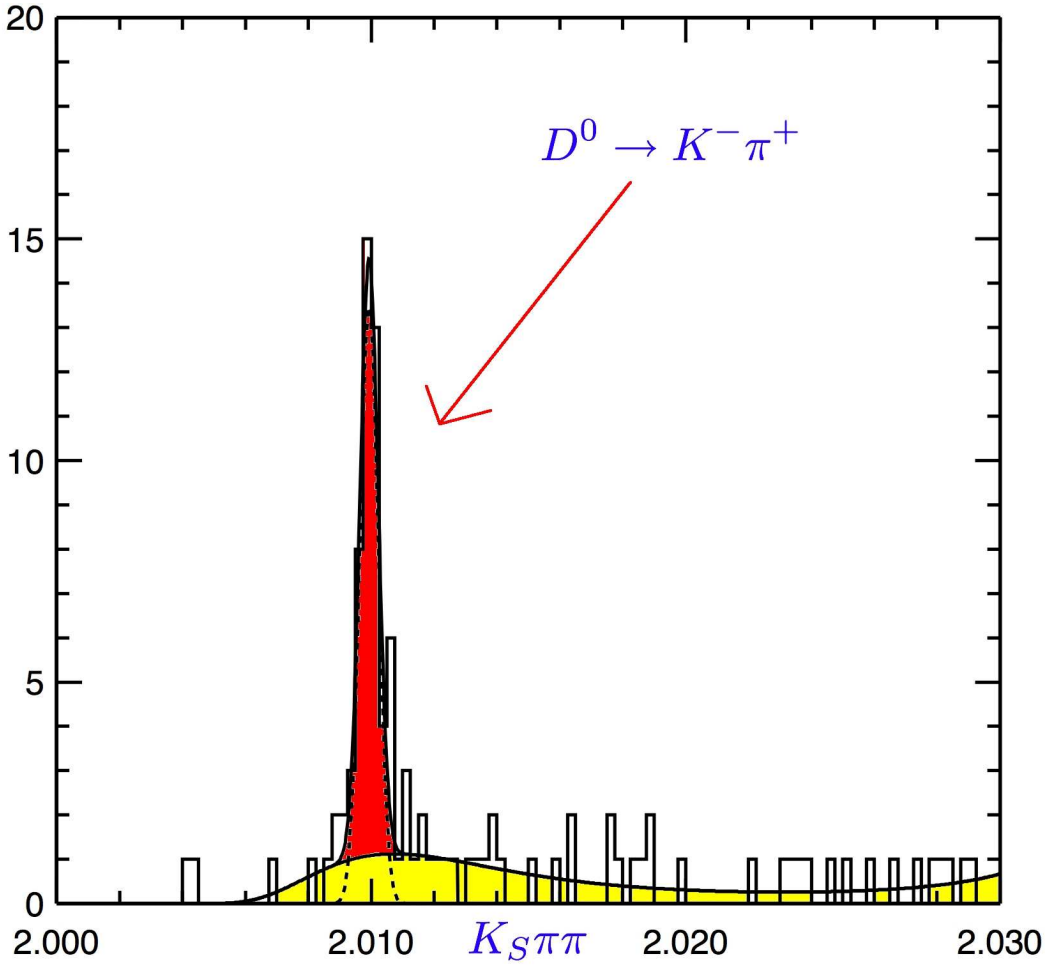

Figure 4.12: The $K^{*-}K^{+}$ in $D^0 \to K^0_S\pi^-\pi^+$ mode, peaking to signal is 0.83%.

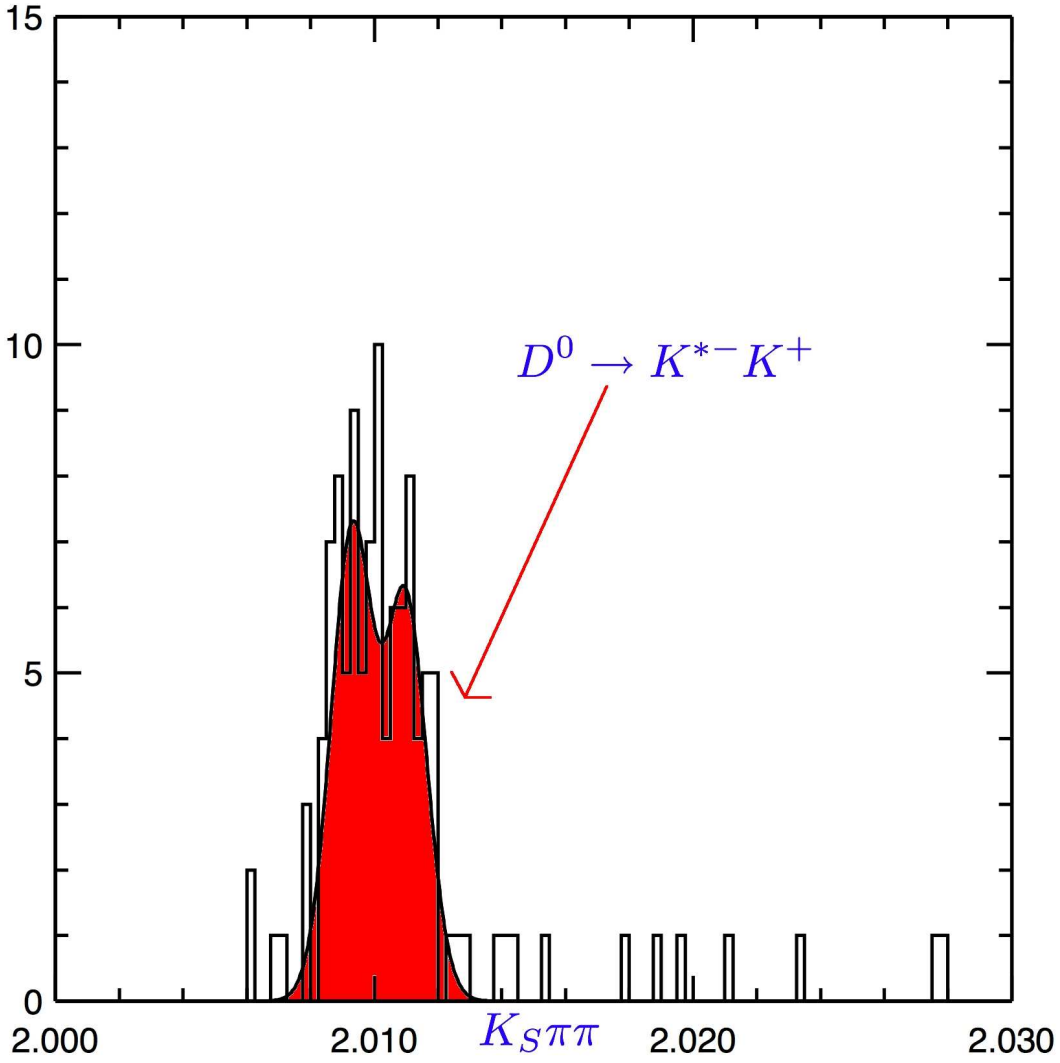

Figure 4.13: The $K^{*+}K^-$ in $D^0 \to K^0_S\pi^-\pi^+$ mode, peaking to signal is 0.87%.

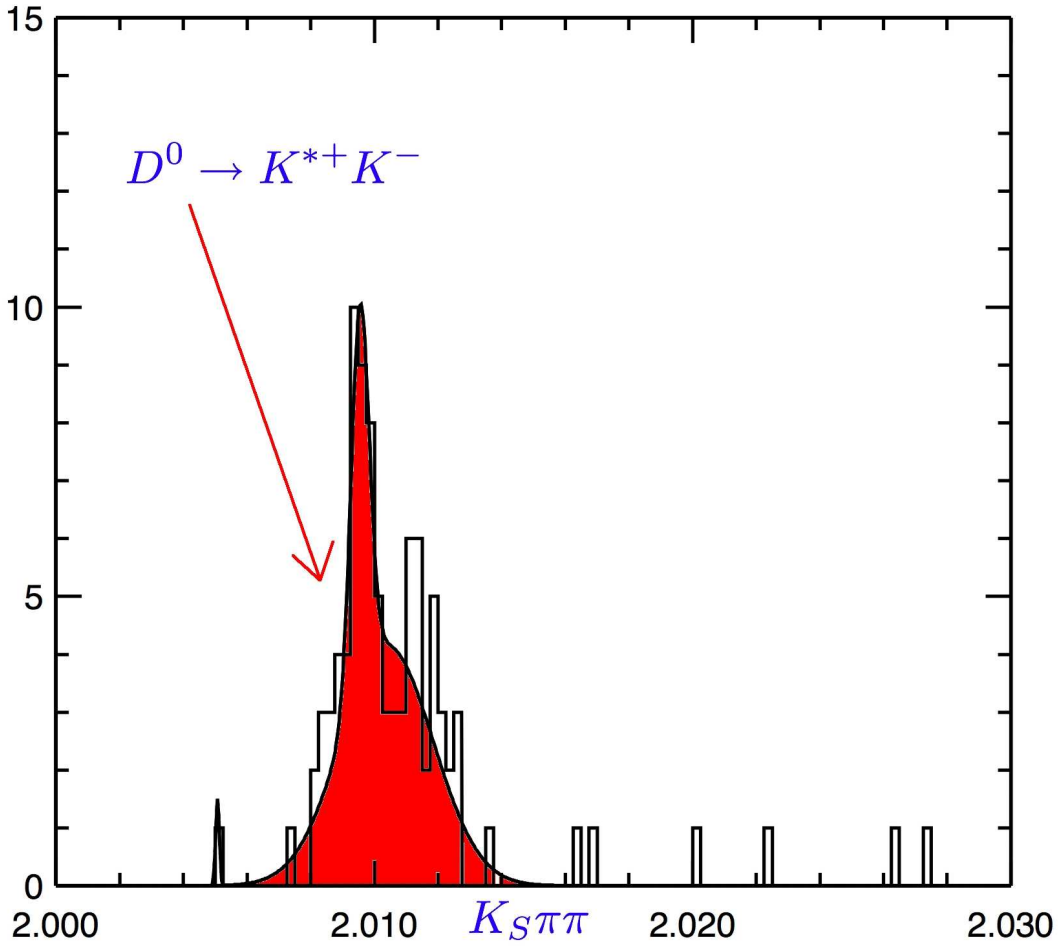

Figure 4.14: The unidentified component in $D^0 \to K^0_S\pi^-\pi^+$ mode, peaking to signal is 3.70%.

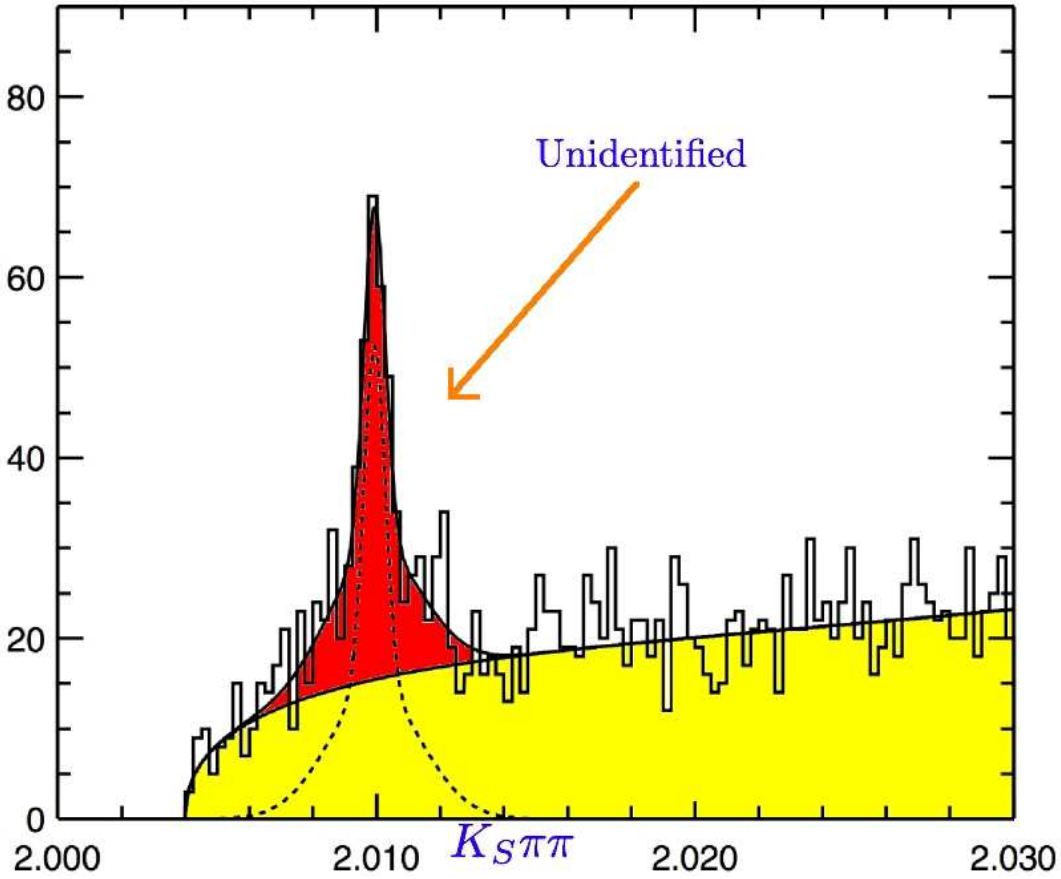

Figure 4.15: The $K^0_L\rho^0$ peaking in $D^0 \to K^{0\,ecl}_L\pi^+\pi^-$ mode, peaking to signal is 3.58%.

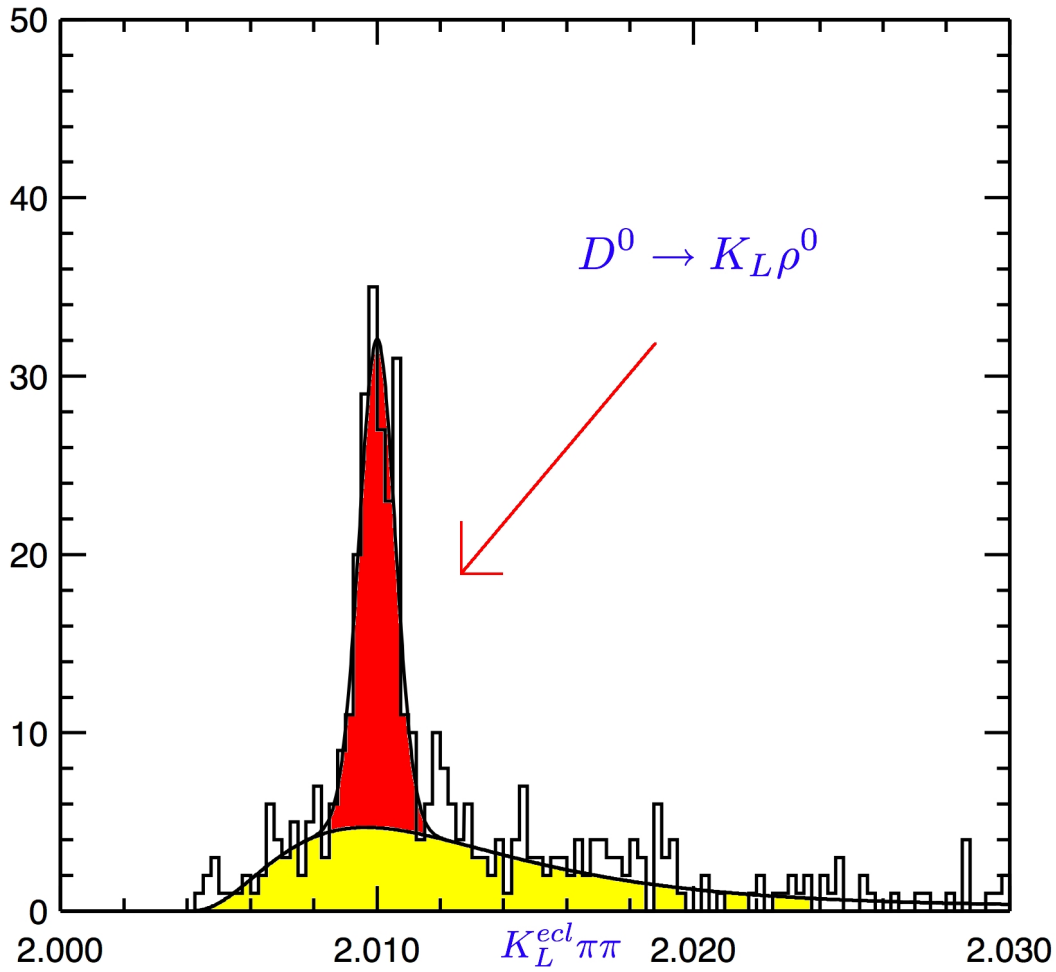

Figure 4.16: The $K_L\eta + K_L\omega + K_Lf$ etc broad resonances peaking in $D^0 \to K_L^{0ecl}\pi^+\pi^-$ mode, peaking to signal is 0.81%.

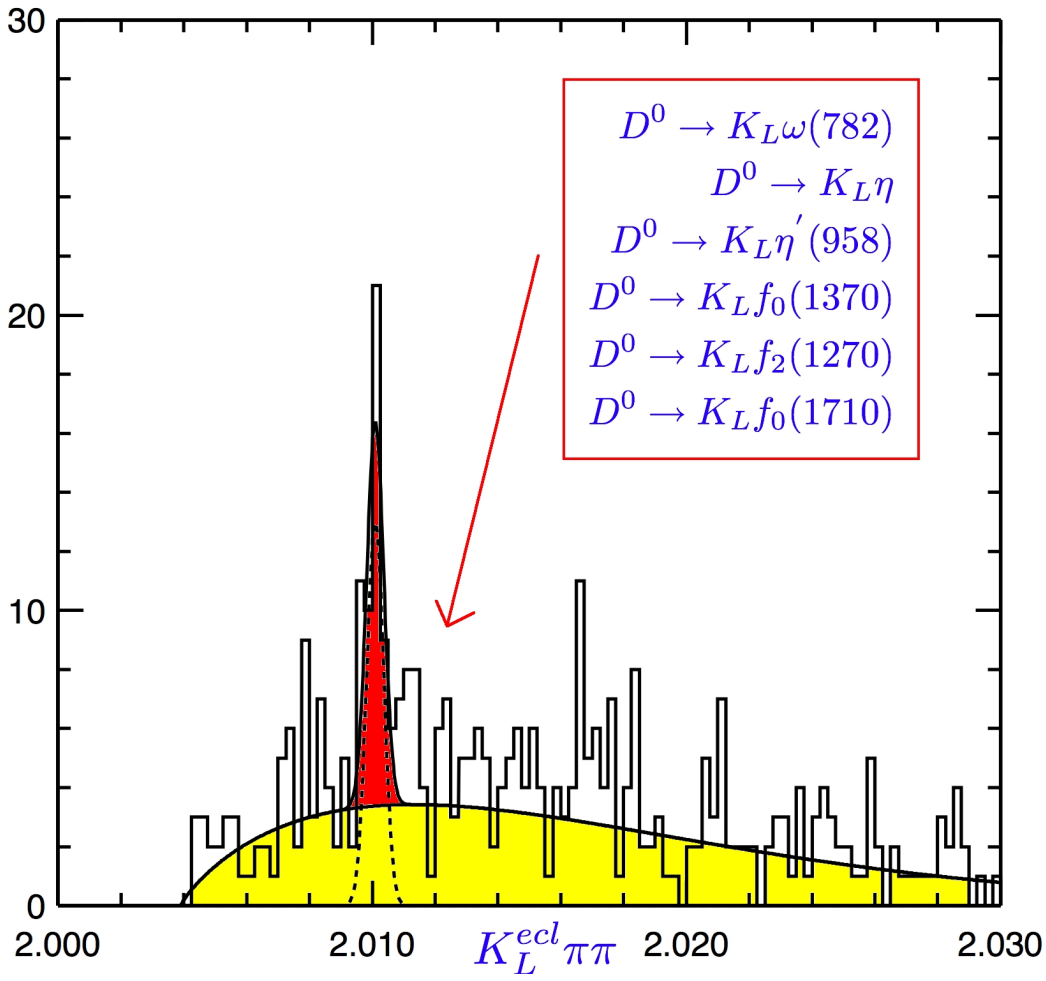

Figure 4.17: The $K^-\pi^+$ in $D^0 \to K_L^{0\,ecl}\pi^-\pi^+$ mode, peaking to signal is 2.66%.

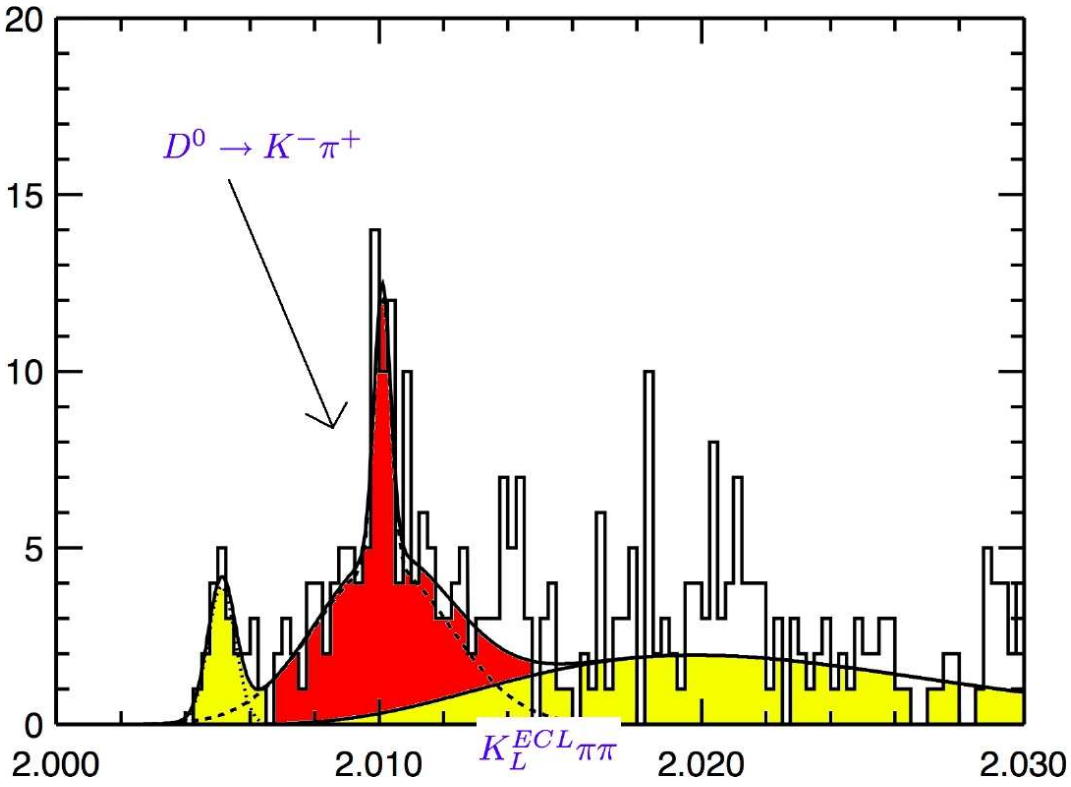

Figure 4.18: The $K^{*-}K^{+}$ in $D^0 \to K_L^{0\,ecl}\pi^-\pi^+$ mode, peaking to signal is 0.69%.

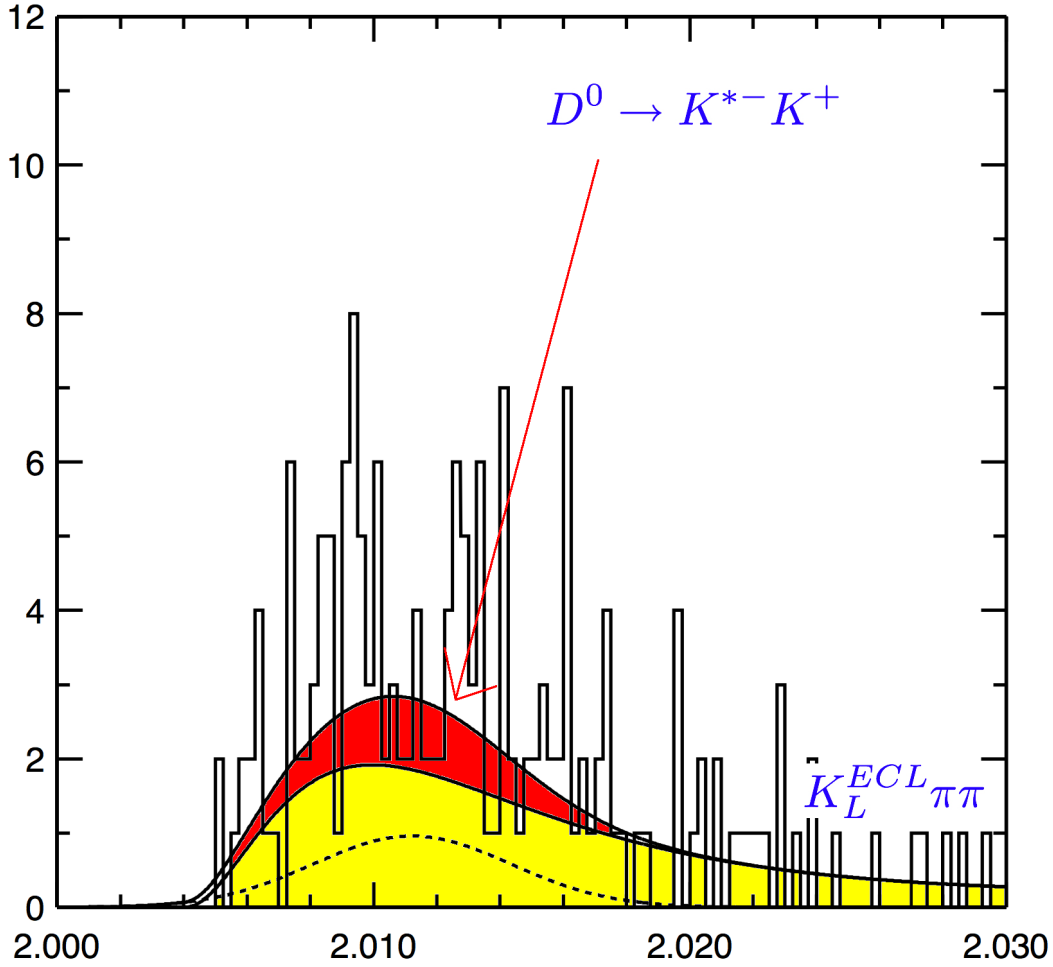

Figure 4.19: The $K^{*+}K^-$ in $D^0 \to K_L^{0\,ecl}\pi^-\pi^+$ mode, peaking to signal is 1.66%.

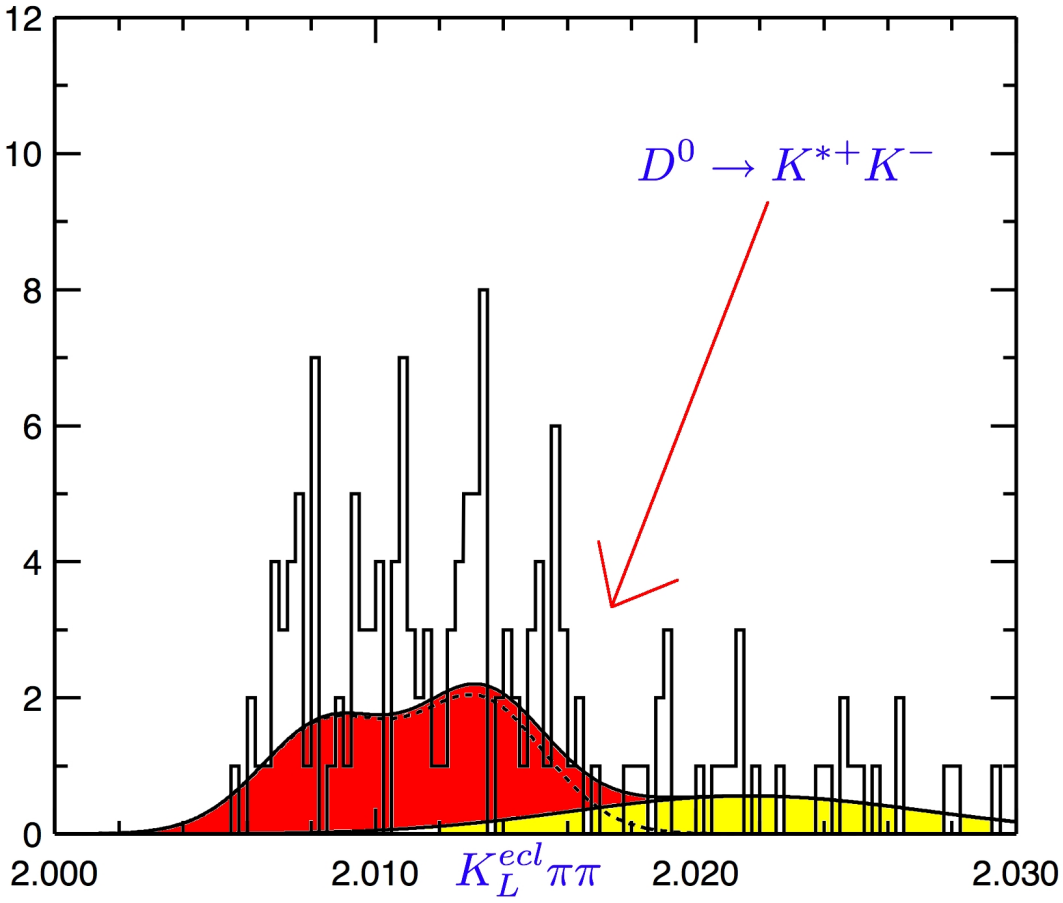

Figure 4.20: The unidentified bump in $D^0 \to K_L^{0\,ecl}\pi^-\pi^+$ mode. If we discard all $K_L^{0\,ecl}$, then loss in signal efficiency is 37.23% in signal mode. The corresponding loss in calibration mode is 33.34%, peaking to signal is 36.78%.

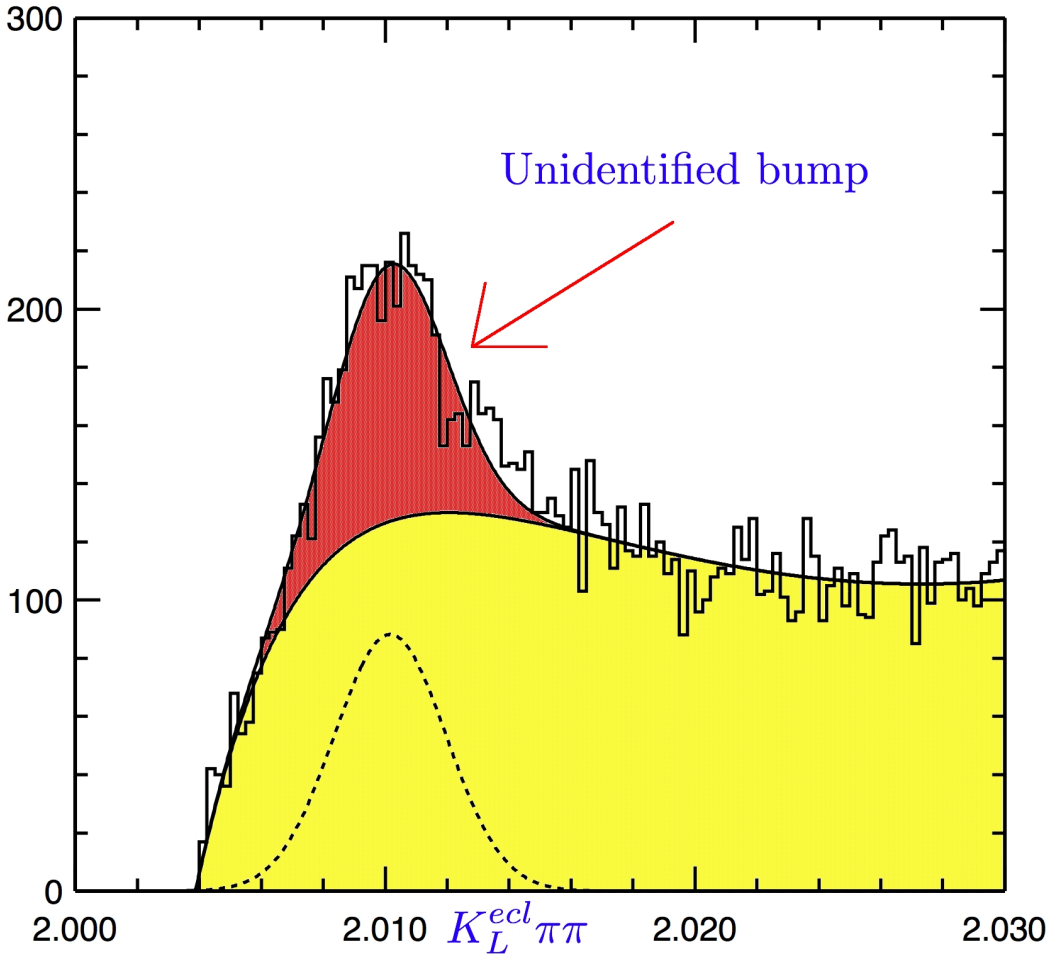

Figure 4.21: The $K_L\rho^0$ peaking in $D^0 \to K_L^{0klm}\pi^-\pi^+$ mode, peaking to signal is 6.98%.

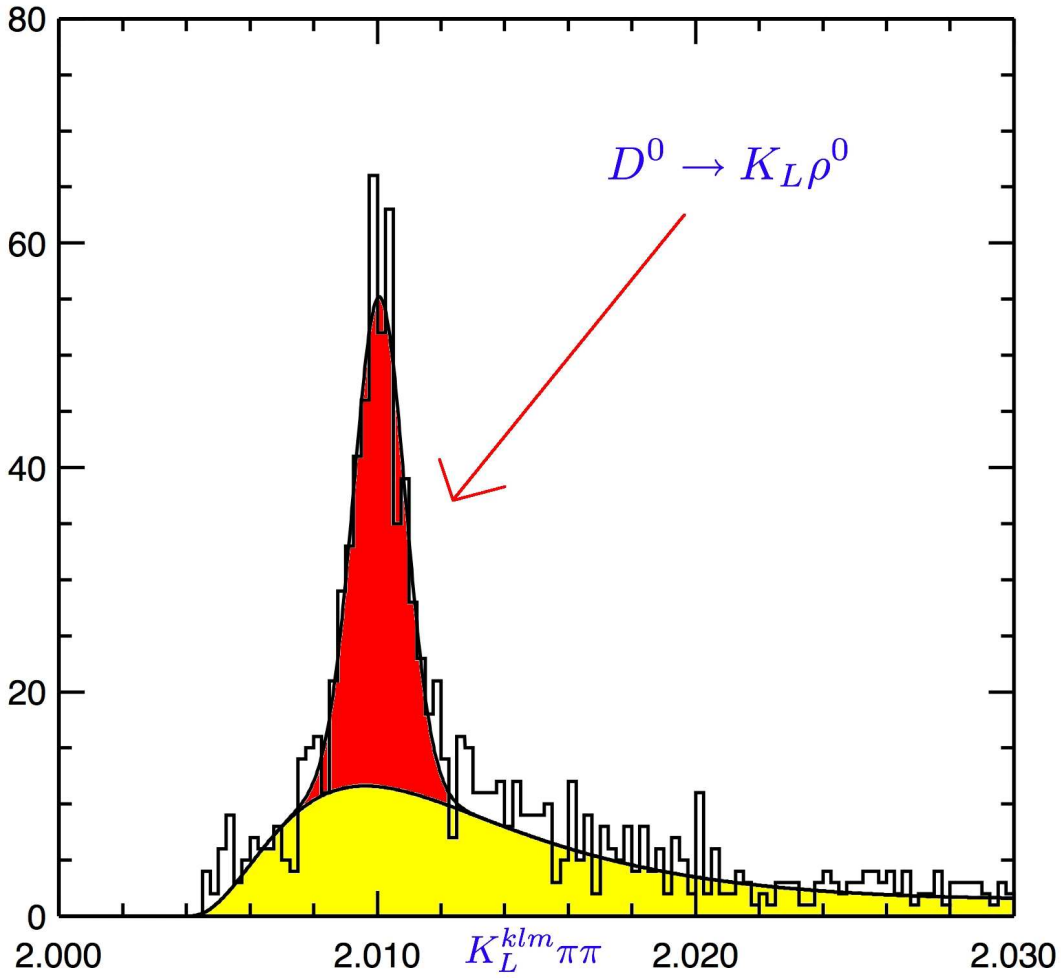

Figure 4.22: The broad resonances$K_L\eta + K_L\omega + K_L f$ etc peaking in $D^0 \to K_L^{0klm}\pi^-\pi^+$ mode, peaking to signal is 1.10%.

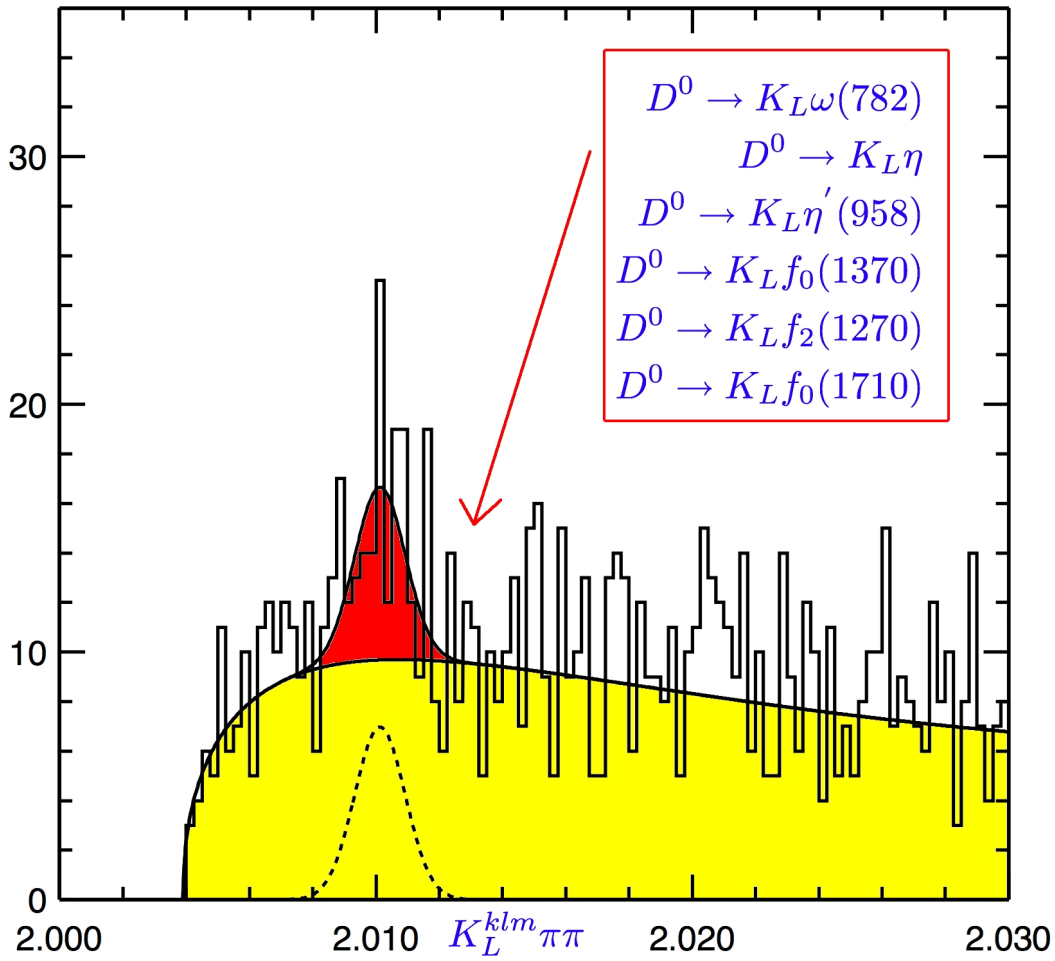

Chapter 5

Experimental Data from Belle

in this Chapter....The yields of the signal obtained from experimental data is described.

Chapter 6

Results

in this Chapter.....The results obtained from both inclusive monte carlo and experimental data are analyzed to obtain a quantitative value for the Asymmetry we intended to determine in our measurement with the error we could ascribe to the methods.

6.1 Asymmetry and Errors

1. Estimate of Peaking background from M.C.

y(i) = Yield of ith peaking background mode with statistical error from fit s(i)

α**(i)** = Generated B.F. of ith peaking background mode

β**(i)** = PDG B.F. of ith peaking background mode with uncertainty σ(i)

L_{data} = data size

L_{MC} = MC size

2. Bias of fit from MC

Y_F**(j)** = Yield of jth signal mode with statistical error from fit s_F(j) obtained from fit to total MC, signal + background

Y_B**(j)** = background subtracted signal yield = Y_F(j) - $\sum$ y(i)

Y_T**(j)** = Yield of truely reconstructed signal for jth mode with statistical error from fit s_T(j)

3. Asymmetry in data

$Y_F^{'}$**(j)** = Signal yield in data with error $s_F^{'}$(j)

$Y_B^{'}$**(j)** = background subtracted signal yield in data = $Y_F^{'}$(j) - $\sum$(scale) y(i), where scale = $(\frac{L_{data}}{L_{MC}})(\frac{\beta(i)}{\alpha(j)})$ (???)

Thus $A^{'} = \frac{Y_B^{'}(1) - Y_B^{'}(2)(\frac{Y_B^{'}(3)}{Y_B^{'}(4)})}{Y_B^{'}(1) + Y_B^{'}(2)(\frac{Y_B^{'}(3)}{Y_B^{'}(4)})}$ where 1, 2, 3, 4 are the four (signal and calibration) modes.

4. pseudo-K_L^0 and K_S^0 sample

Divide the data into two samples of size L_1 and L_2

Calculate the asymmetry, $A^{''}$ similar to $A^{'}$

5. Multiple candidates

fraction of events with more than 1 candidates per event with error. f(j) and $s_f(j)$

6.2 Conclusion

Chapter 7

Summary

in this Chapter....We draw a conclusion to our measurement.

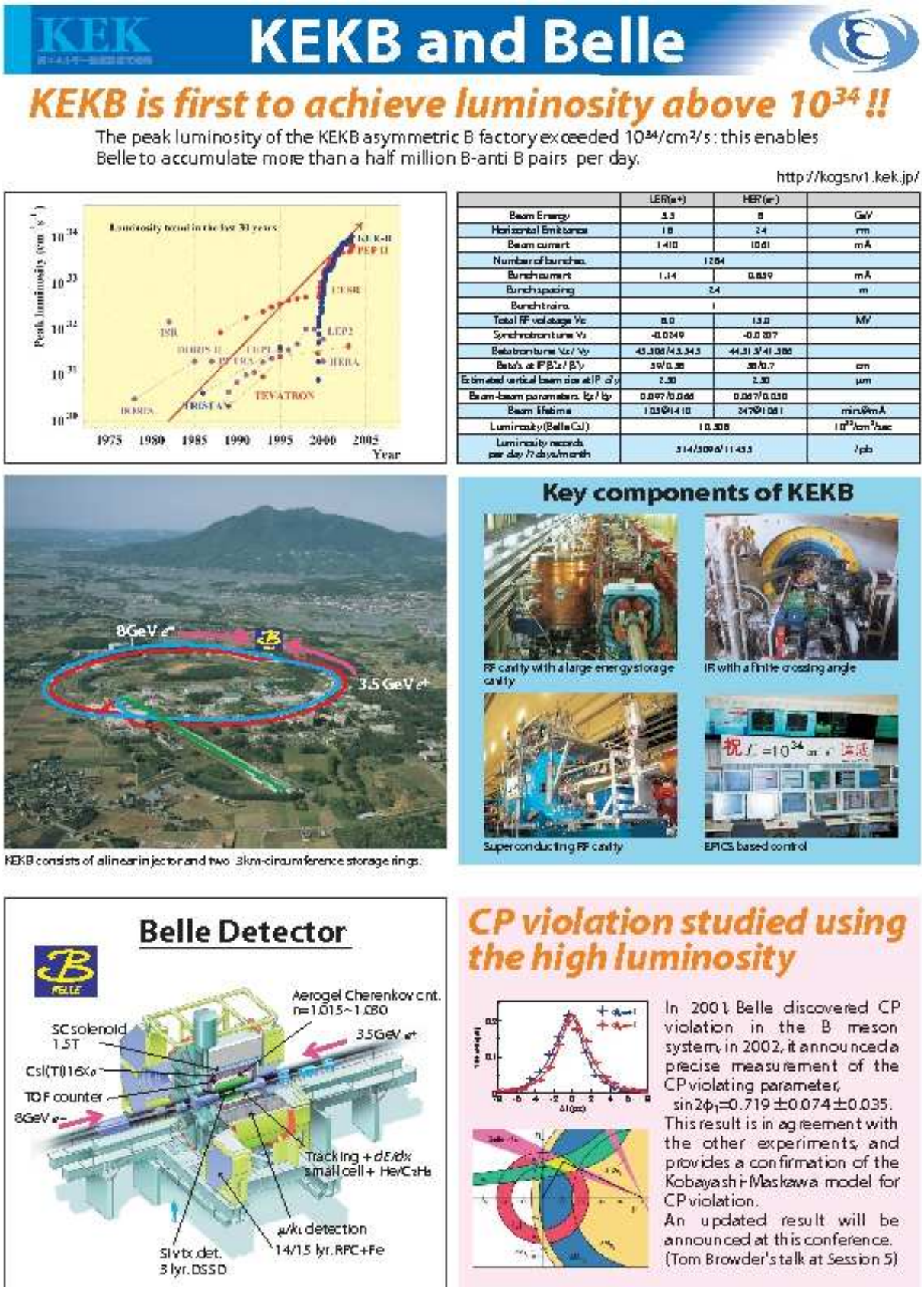

Figure 7.1: The KEKB accelerator and Belle Experiment

Figure 7.2: The Japanese duo who won the Nobel-2008 depicted in this animation. They had correctly predicted the quark mixing which is evidenced in the Belle B-meson studies.

Appendix A

Monte Carlo

A.1 Generating signal in QQ98

```
DECAY VPHO
CPTAG
MATRIX 1. 0. -1.
CHANNEL 0 1.00 D*+ D*-
ENDDECAY
DECAY D*+
HELICITY 1.0 0 0
CHANNEL 0 1.0 D*+ PI-
ENDDECAY ;
DECAY D*+
ANGULAR_HELICITY -1 1. 0. -1.
ANGULAR_HELICITY 0 0. 0. 1.
ANGULAR_HELICITY 1 1. 0. -1.
CHANNEL 0 1.0 D0 PI+
ENDDECAY ;
DECAY D0
HELICITY 1.0 0 0
CHANNEL 0 1.0 K*- PI+
ENDDECAY
DECAY K*-
ANGULAR_HELICITY -1 1. 0. -1.
ANGULAR_HELICITY 0 0. 0. 1.
ANGULAR_HELICITY 1 1. 0. -1.
CHANNEL 0 1.0 KB PI-
ENDDECAY
; End
```

A.2 Resolution of K_L

The resolution of K_L was studied in more detail and the results are shown here. See Figure A.1,A.2,A.3 and A.4.

Figure A.1: K_L^{ECL} **Resolution in θ and ϕ**

The angular resolutions of the ECL type K_L^0.

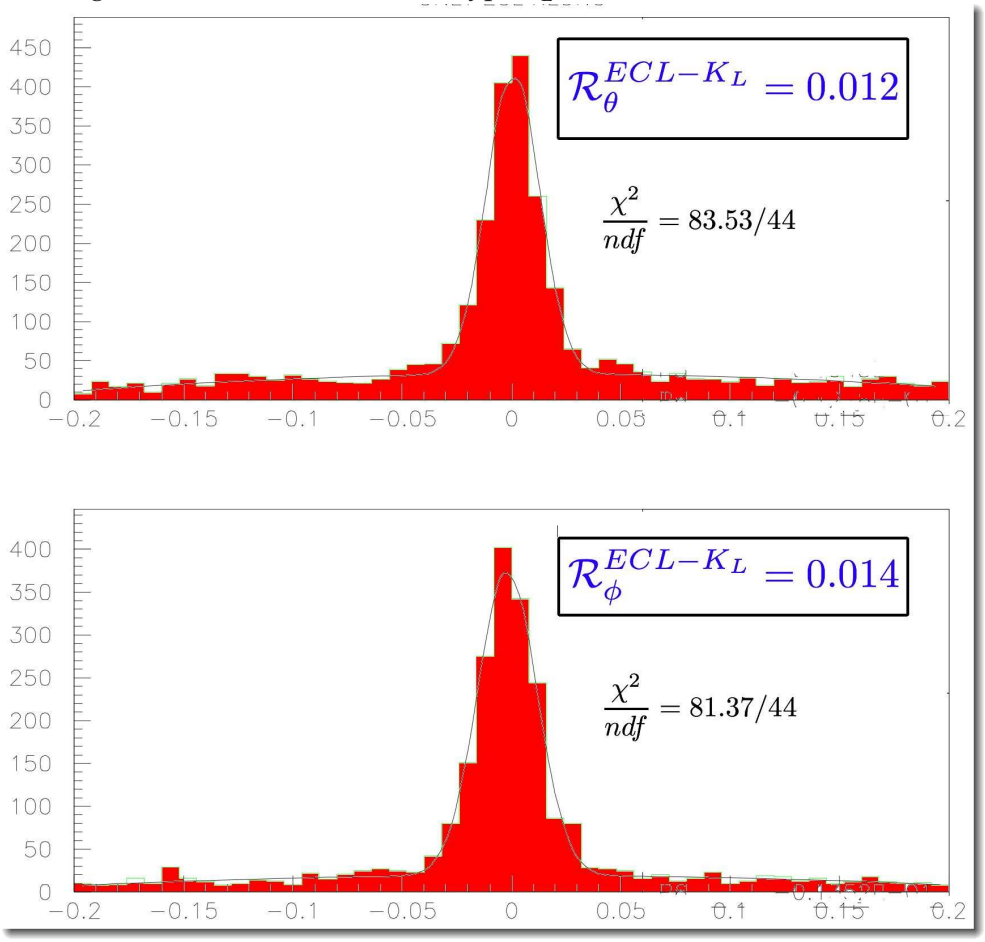

A.3 Factorization of Efficiencies

The factorizability of efficiencies in the $D^0 \to K_S\pi^-\pi^+$ is shown here. The study performed on the $D^0 \to K_S\pi^0$ and the $D^0 \to K_L\pi^0$ modes has been shown earlier. See figure A.5,A.6,A.7.

A.4 The $K_L\pi$ mode backgrounds in inclusive MC

This mode fortunately has no contamination. the broad resonances which are dominate peaking backgrounds in many modes have no presence here. See A.8.

Figure A.2: **"Good" K_L^{ECL} Resolution in θ and ϕ**

The angular resolutions of ECL type K_L^0s for events in the 3 σ region.

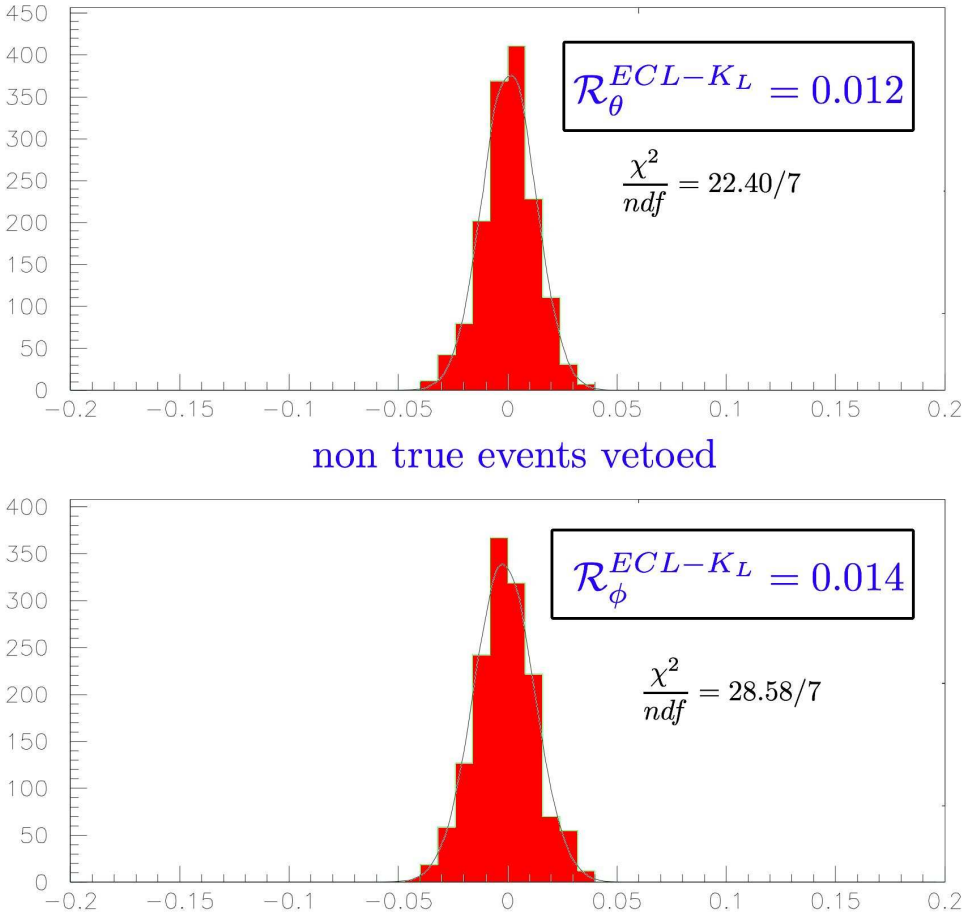

A.5 $c\bar{c}$, $b\bar{b}$ AND *uds* BACKGROUNDS IN INCLUSIVE MC

The $c\bar{c}$, $b\bar{b}$ and *uds* backgrounds are shown in the plots in figure A.9, A.10 and A.11.

Figure A.3: K_L^{KLM} **Resolution in** θ **and** ϕ

The angular resolutions of KLM type K_L^0.

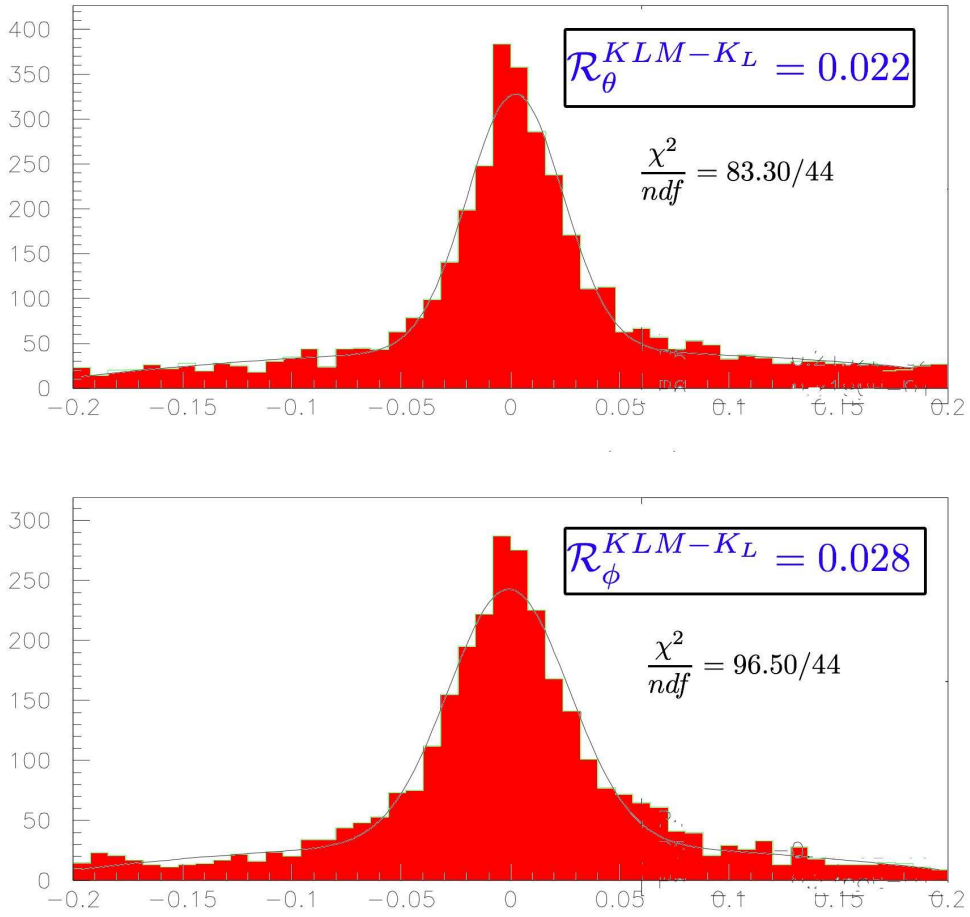

Figure A.4: K_L^{KLM} **Resolution in θ and ϕ**

K_L^{KLM} Resolution in θ and ϕ for events in the 3 σ region.

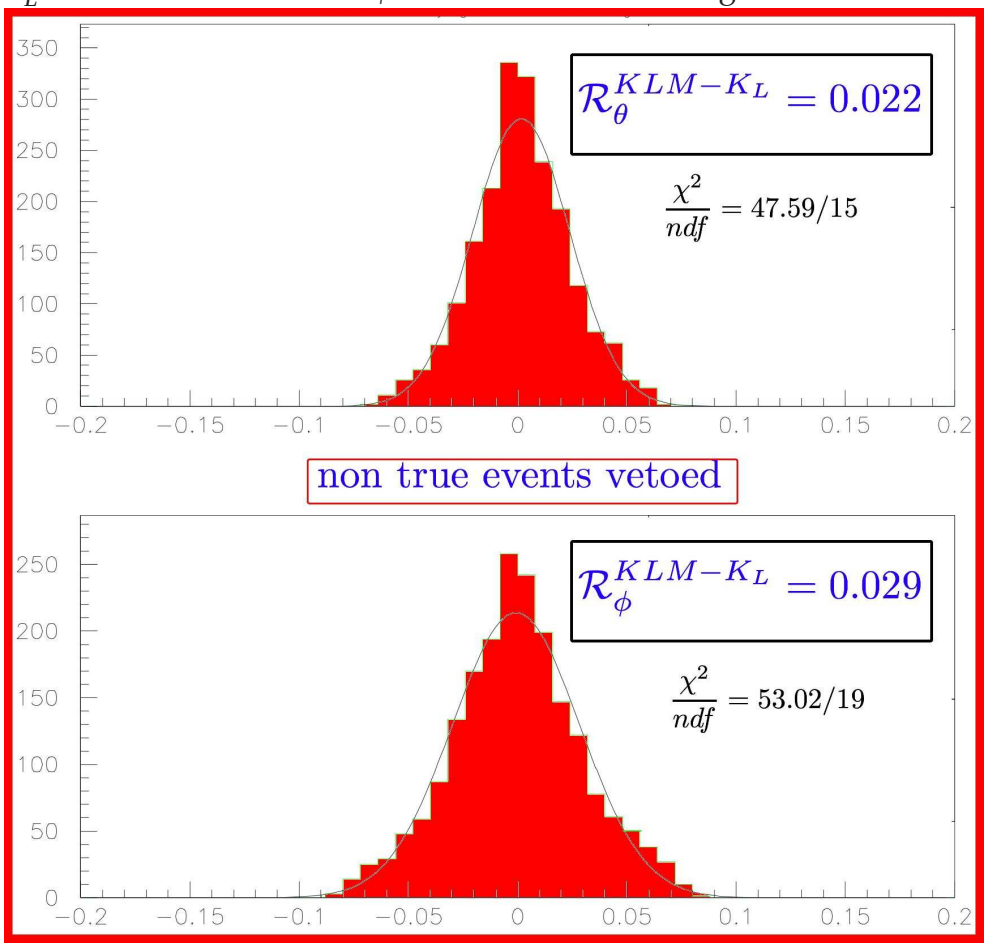

Figure A.5: Factorizability in $D \to K_S\pi^+\pi^-$

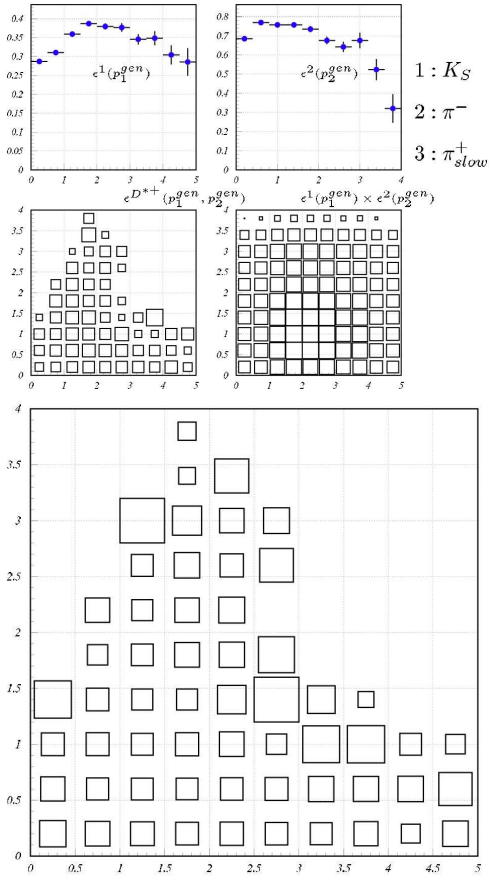

Figure A.6: Factorizability in $D \to K_S\pi^+\pi^-$

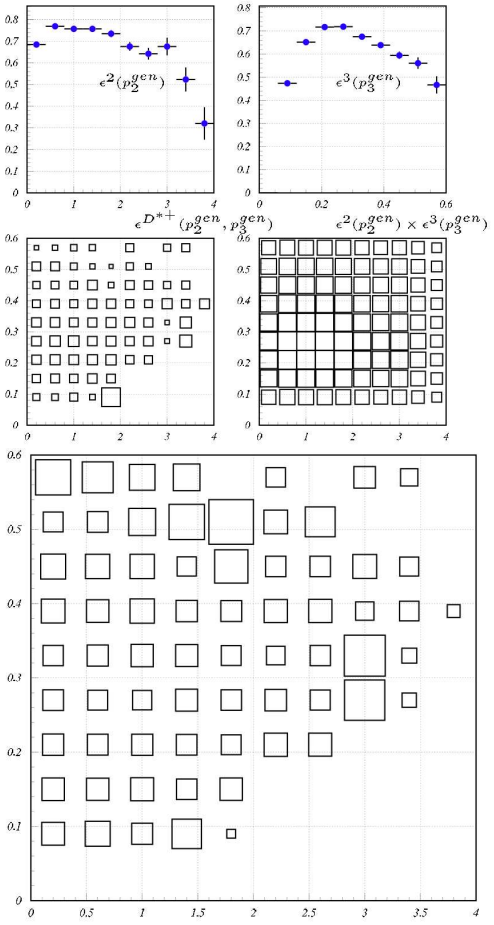

Figure A.7: Factorizability in $D \to K_S\pi^+\pi^-$

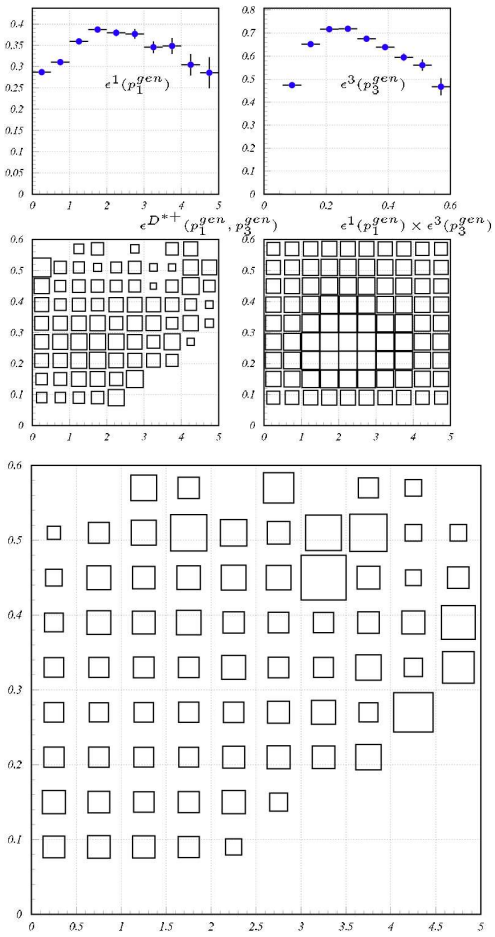

Figure A.8: The klpi mode backgrounds

The $K_L\pi$ mode has no peaking contamination, The $K_S\pi$ mode is also very clean except for a negiligible peaking backgrounds a) all broad resonances in ECL type b) all broad resonances in KLM type c) the c-cbar background in klpi d)the c-cbar klm background in klpi

figures/peak_bkg/fit/klpi_allbroad_ecl.eps	figures/peak_bkg/fit/klpi_allbroad_klm
figures/peak_bkg/fit/klpi_ccbar_ecl.eps	figures/peak_bkg/fit/klpi_ccbar_klm.eps

Figure A.9: The continuum [$c\bar{c}$] background

The continuum [$c\bar{c}$] background a) ccbar kspi b) ccbar klpi, klm c) ccbar klpi, ecl d) ccbar in klpipi, klm

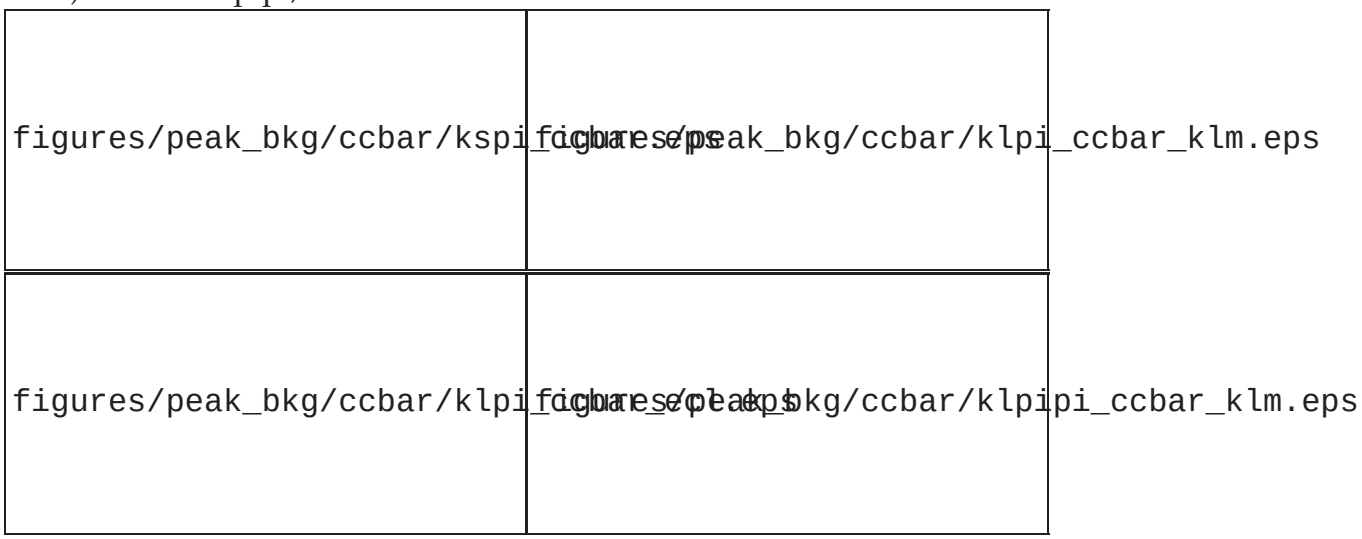

Figure A.10: $b\bar{b}$ background

Figure A.11: uds background

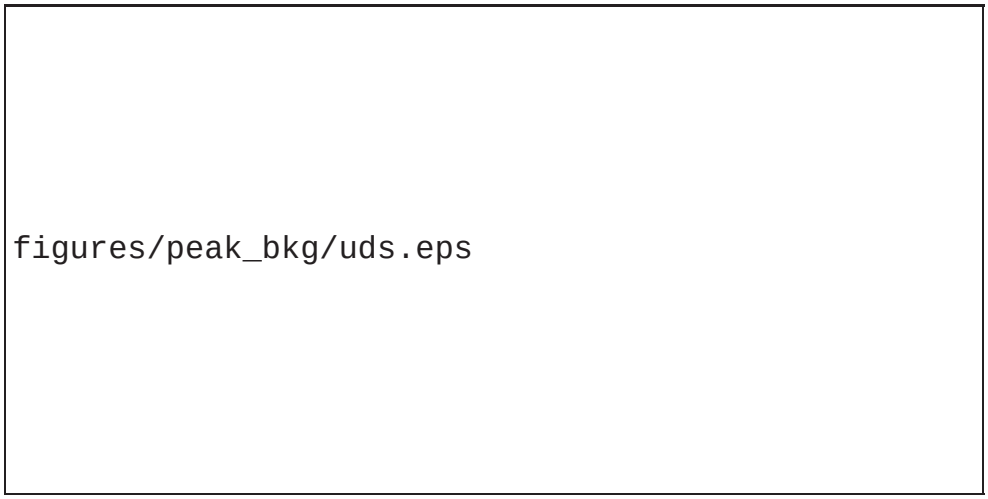

Bibliography

[1] J. M. Link et al. (E687 Collaboration), Phys. Lett. B ***485***, 62 (2000).

[2] R. Godang et al. (CLEO Collaboration), Phys. Rev. Lett. ***84***, 5038 (2000).

[3] K. Abe et al. (Belle Collaboration), BELLE-CONF-0131 (2001).

[4] E. Golowich and S. Pakvasa, Phys. Lett. B ***505***, 94 (2001).

[5] K. Abe et al. (Belle Collaboration), KEK Progress Report 2000-4 (2000), to be published in Nucl. Inst. and Meth. A.

[6] D. E. Groom et al. (Particle Data Group), Eur. Phys. J. ***C15***, 1 (2000).

[7] I.I. Bigi and H. yamamoto, arXiv:hep-ph/9502238 v1 6 Jan 1995

[8] DORIS (Doppel-Ring-Speicher, "double-ring storage") was DESY's second circular acclerator.

[9] `http://www.lns.cornell.edu/public/CESR/`

[10] `http://lns.cornell.edu/public/CLEO`; CLEO Collaboration, J. P. Alexander et-al, \PRL86 2001 2737-2741

[11] Particle Data Group, S. Eidelman et-al, PLB 592 1 2004.

[12] Belle Collaboration, A. Abashian et-al, NIMA 479 117 2002.

[13] L. Wolfenstein, Phys. Rev. Lett. ***51***, 1945 (1983).

[14] DELPHI Collaboration, V. Chabaud et-al, The DELPHI silicon strip microvertex detector with double sided readout, NIMA 368 1996 314332.

[15] O. Toker, S. Masciocchi, E. Nygard, A. Rudge, and P. Weilhammer, VIKING: A CMOS low noise monolithic 128-channel front-end for Si strip detector readout, NIMA 340 1994 572579.

[16] The VA1TA Chip. http://www.ideas.no/ User Manual.

[17] Belle Collaboration, M. e. a. Yokoyama, Radiation Hardness of VA1 with Submicron Process Technology, IEEE Trans. Nucl. Sci. Vol. 48 (2001) 440443.

[18] R. Abe et-al, Status of the Belle SVD detector, NIMA 478 2002 296298; T. Kawasaki, The Belle silicon vertex detector, NIMA 494 2002 94101; BELLE Collaboration, G. Alimonti et al., The BELLE silicon vertex detector, NIMA 453 2000 7177 ; M. Hazumi, Performance of the Belle silicon vertex detector, NIMA 473 2001 16.

[19] Y. Ushiroda, NIMA 511 6 2003.

[20] H. Hirano et-al, A high resolution cylindrical drift chamber for the KEK B- factory, NIMA 455 2000 294304.

[21] T. Iijima et-al, Aerogel Cherenkov counter for the BELLE detector, NIMA 453 2000 321325; T. Iijima et-al, Aerogel Cerenkov counter for the BELLE experiment, NIMA s379 1996 457459.

[22] H. Kichimi et-al, The BELLE TOF system, NIMA 453 2000 315320.

[23] H. Ikeda et-al, A detailed test of the CsI(Tl) calorimeter for BELLE with photon beams of energy between 20-MeV and 5.4-GeV, NIMA 441 2000 401426.

[24] Belle Collaboration, V. Zhilich, Online Luminosity Measurements with CSI Calorimeter at the Belle Detector, Belle Note 465 (2001). Belle internal paper.

[25] Y. Ushiroda et-al, Development of the central trigger system for the BELLE detector at the KEK B-factory, NIMA438 1999 460471

[26] BELLE Collaboration, M. Nakao, M. Yamauchi, S. Y. Suzuki, R. Itoh, and H. Fujii, Data acquisition system for the BELLE experiment, IEEE Trans. Nucl. Sci. 47 (2000) 5660.

[27] M. Tomoto et-al, Z-trigger system with the BELLE central drift chamber, NIMA 447 2000 416423.

[28] Belle Collaboration, S. e. a. Nishida, Trigger effciency, Belle Notes 350, 381, 423, 459, 504, 520, 548, 584 (2000-2002). Belle internal paper.

[29] S. Nishida, Radiative B decays into K pi gamma and K pi pi Final States,. PhD Thesis 2004/3.

[30] Belle Collaboration, K. H. et al., Level 4 Software Trigger at Belle, Belle Note 299 (2000).

[31] T. Sjostrand, High-energy physics event generation with PYTHIA 5.7 and JETSET 7.4, Comput. Phys. Commun. 82 (1994) 7490; T. Sjostrand, PYTHIA 5.7 and JETSET 7.4: Physics and manual, hep-ph/9508391.

[32] B. Andersson, G. Gustafson, G. Ingelman, and T. Sjostrand, PARTON FRAGMENTATION AND STRING DYNAMICS, Phys. Rept. 97 (1983) 31.

[33] http://www.lns.cornell.edu/public/CLEO/soft/QQ/

[34] http://www.slac.stanford.edu/ lange/EvtGen/

[35] R. Brun et al., GEANT 3.21, CERN Report No. DD/EE/84-1 , 1987